Polymeric semiconductor and transition-metal dichalcogenide nanocomposites for inkjet-printed thin-film transistor devices

by

Hyunwoo Choi

A thesis
presented to the University of Waterloo
in fulfillment of the
thesis requirement for the degree of
Doctor of Philosophy
in
Electrical and Computer Engineering

Waterloo, Ontario, Canada, 2023

Examining Committee Membership

The following served on the Examining Committee for this thesis.

External Examiner	Dr. Tse Nga Tina Ng Department of Electrical and Computer Engineering University of California San Diego
Supervisor	Dr. William S. Wong Department of Electrical and Computer Engineering University of Waterloo
Internal Examiner	Dr. Youngki Yoon Department of Electrical and Computer Engineering University of Waterloo
Internal Examiner	Dr. Siva Sivoththaman Department of Electrical and Computer Engineering University of Waterloo
Internal-External Examiner	Dr. Michael K. C. Tam Department of Chemical Engineering University of Waterloo

Author's Declaration

I hereby declare that I am the sole author of this thesis. This is a true copy of the thesis, including any required final revisions, as accepted by my examiners.

I understand that my thesis may be made electronically available to the public.

Abstract

Patterned using subtractive processes, conventional thin-film deposition techniques inevitably require high-vacuum deposition and photolithography to define functional layers to create a device structure. Inkjet printing technology has received considerable attention to realize low-cost and potential mass production of large-area electronics at low temperatures using an additive process approach. However, the materials used in the printing process are based on solution-based electronic inks formulated with organic electronic materials. Among them, conjugated polymers are widely used as a semiconductor for thin-film transistor (TFT) applications, but they possess poor charge transport properties compared to other single or polycrystalline inorganic semiconductors. Moreover, the inkjet printing method has a weakness for depositing polymeric solution that form thin films having a highly ordered molecular structure.

To overcome this limitation when using printed polymers, a hybrid organic/inorganic semiconductor ink was explored. The hybrid semiconductor ink was prepared by mixing two different materials, molybdenum disulfide (MoS_2) nanosheets and solution-based poly(3-hexylthiopene-2,5-diyl) (P3HT), the former is a two-dimensional semiconductor and the latter a conjugated polymer. To enhance the level of exfoliation and stability of MoS_2 nanosheets in P3HT, the surfactant trichloro(dodecyl)silane (DDTS), was used to functionalize the MoS_2 surface. Printed TFTs using the nanosheet suspension were found to enhance the field-effect mobility by approximately 3× compared to TFTs without the suspension. The introduced single-crystalline MoS_2 nanosheets in the P3HT matrix improved the electrical and structural properties of the inkjet-printed thin-film polymer.

Based on these findings and insights, the observed effects can be extended to second-generation polymeric semiconductors, specifically the donor-acceptor (D-A) co-polymers. These materials are renowned for exhibiting the highest mobilities among printable polymers while maintaining ambipolarity, a desirable trait for configuring complementary metal-oxide-semiconductor (CMOS) circuits. In light of this, novel nanocomposite semiconductor inks were developed to demonstrate the influence of 2D nanoparticles on the electronic properties of D-A copolymers, diketopyrrolopyrrole-thieno[3,2-b]thiophene (DPPT-TT). Printed TFTs using this new hybrid semiconductor showed that the field-effect mobility of the devices increased by 33 % and 140 % in both hole (p-type) and electron (n-type) transports, respectively. Atomic force microscopy (AFM) results of the printed hybrid thin film revealed that strongly aggregated polymer domains were observed in films containing the MoS_2

nanosheets. In ultraviolet–visible–near infrared spectroscopy (UV-vis-NIR) measurement, increased intensity of 0-0 and 0-1 peaks from hybrid film indicates improved charge transport was due to enhanced intermolecular charge transfer in the microstructure of the polymer film. Furthermore, the incorporation of hybrid nanocomposites proved particularly beneficial for inkjet-printed TFTs utilizing metal electrodes, as the latter had a tendency to augment contact resistance and thereby compromise device performance. However, the introduction of hybrid nanocomposites effectively counteracted the performance degradation arising from the printed metal electrodes by enhancing the crystallinity of the polymeric film. Moreover, these findings also highlight the feasibility of employing lower sintering temperatures for inkjet-printed metal electrodes. This is attributed to the fact that the result of increased contact resistance associated with lower sintering temperatures can be effectively mitigated by the nanocomposite semiconductor. Consequently, an overall enhancement in device performance was achieved by applying the hybrid nanocomposite ink. This study elucidated the advantageous influence of solution-processed MoS_2 nanosheets on the crystallinity and electrical properties of polymeric thin films, consequently leading to significant improvements in the performance parameters of inkjet-printed TFTs.

Acknowledgements

I want to convey my most profound appreciation to Prof. William Wong, my supervisor, for providing incredibly valuable comments and recommendations. His assistance, extensive expertise, patience, and editing abilities played a significant role in the successful completion of this thesis.

I also wish to express my appreciation to my committee members, namely Prof. Youngki Yoon, Prof. Michale Tam, Prof. Siva Sivoththaman, and Prof. Tse Nga Ng, for their meticulous review of my thesis and their valuable suggestions during the defense.

Above all, I want to extend my gratitude to Dr. Wontae Park for his close collaboration with me, for imparting comprehensive training in all facets of device fabrication and analysis, and for serving as an exemplary mentor.

Furthermore, I want to acknowledge the following individuals: Dr. Czang-Ho Lee, for guiding me in utilizing a majority of the experimental tools in the lab; Richard Barber, who manages all lab facilities and ensures my safety while working; Dr. Roksana Tonny Rashid, for assisting me with the SEM system; Dr. Yebin Lee, for helping me with UV-vis spectroscopy; and Dr. Dong Seob Chung, for providing training on the use of AFM.

Many thanks to my colleagues at Advanced Flexible Electronic Technology (AFET) group, Dr. Mohsen Asad, Dr. Mohammad Nouri, and Pranav Gavirneni for their valuable insights and engaging discussions pertaining to my research works.

Lastly, I extend heartfelt thanks to my family for their unwavering support and guidance throughout these years.

Dedication

To my family, Minsun, and Yunho

Table of Contents

List of Figures

List of Abbreviations

2D: Two-dimensional
AFM: Atomic force microscopy
ATSs: Alkyl-trichlorosilanes
BGBC: Bottom-gate, bottom-contact
CBM: Conduction band minimum
CMOS: Complementary metal-oxide semiconductor
CNTs: Carbon nanotubes
CVD: Chemical vapor deposition
DA copolymer: Donor-acceptor copolymer
DCB: 1,2-dichlorobenzene
DDTS: Dodecyltrichlorosilane, trichloro(dodecyl)silane
DPPT-TT: Diketopyrrolopyrrole thieno[3,2-b]thiophene
HMDS: Hexamethyldisilane
HOMO: Highest-occupied molecular orbital
IJP: Inkjet-printing
LER: Line edge roughness
LUMO: Lowest-unoccupied molecular orbital
MoS_2: Molybdenum disulfide
NPs: Nanoparticles
OSC: Organic semiconductor
OTFT: Organic thin film transistor
P3HT: poly(3-hexylthiopene-2,5-diyl)
PR: Photoresist
PVD: Physical vapor deposition
R2R: Roll-to-roll
S/D: Source and drain
SAM: Self-assembled monolayer
SEM: Scanning electron microscope
S.S.: Subthreshold swing
TFT: Thin film transistor
TMDCs: Transition metal dichalcogenides
UV-vis: Ultraviolet-visible
UV-vis-NIR: Ultraviolet-visible-near infrared
VBM: Valance band maximum
XRD: X-ray diffraction

Chapter 1
Introduction

1.1 Flexible and large-area electronics

As an emerging technology, flexible and large-area electronics have the attractive potential to bring an industrial revolution to the multibillion-dollar consumer electronics market [1, 2]. This technology will play a key role in the realization of next-generation electronics applications such as wearable devices, fully rollable displays, and textile-based electronics. In the display industry, especially, the display panel has been developed for large-scale integration enabled by a scalable manufacturing process. Moreover, flexible displays are ideally fabricated on polymeric films on substrates such as polyimide (PI) [3], polyethylene terephthalate (PET) [4], and polyethersulfone (PES) [5] that are intolerant to high temperatures and require low thermal-budget processes. At the same time, conventional microfabrication techniques have been used to demonstrate flexible electronic devices and circuits, where the technology for fabricating these electronic devices is thin-film deposition technique for the deposition of high-quality electronic materials. However, the conventional method requires costly fabrication processes such as high vacuum deposition and photolithography processes. For the development of flexible large-area systems, low-cost and large-area inkjet printing (IJP) technology is a promising candidate to replace these conventional microfabrication techniques for next-generation fabrication processes.

1.2 Conventional thin film deposition techniques

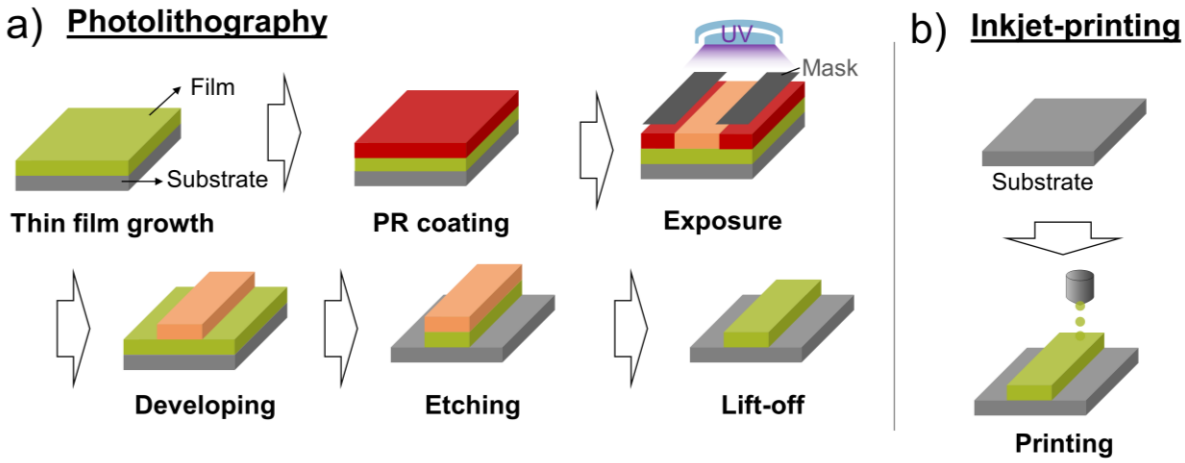

Figure 1.1: a) Schematic illustration of the conventional photolithography process with negative photoresist and b) inkjet-printing process.

The conventional process for defining a structure employs a subtractive approach where photolithography patterning of the thin film defines specific geometries on thin-film layers. Fig. 1.1 shows the schematic illustration of comparing the conventional subtractive microfabrication process with the inkjet-printing method, which uses an additive approach to deposit and pattern the thin film simultaneously. Obviously, the inkjet-printing process has relatively simple and fewer fabrication steps than the conventional subtractive method. Figure 1.1a shows the entire patterning process that begins with the application of a photoresist (PR) coating. PR is spin-coated on the thin film, and it is exposed to ultraviolet (UV) light through a photolithography mask. After exposure, a low-temperature anneal removes the solvents from the PR to fully cure the PR pattern. The exposed thin-film field can then be patterned by a dry or wet etching process. As a final step, the remaining PR is washed away by using a resist stripper. This process is usually the most complex and expensive step in device fabrication and removing this process will greatly simplify and reduce the processing costs. Typical large-area microfabrication approaches for device integration are

generally accomplished using a subtractive process, where thin films are first deposited over the entire surface that is then patterned using an etching process to remove the film to define a given structure. On the contrary, direct thin film deposition and patterning simultaneously can be achieved by inkjet-printing due to its additive nature.

Thin-film deposition is one of the most important technologies for the fabrication of flexible and large-area electronics such as logic circuits, displays, sensors, radio-frequency identification (RFID) tags, and photovoltaics. This method is the basis for the development of thin-film transistors [1, 6, 7]. Thin-film deposition technique has been developed to deposit a high-quality thin film by precisely controlling the growth of the materials. Fig.1.2 shows two different types of thin-film deposition techniques: physical vapor deposition (PVD) and chemical vapor deposition (CVD). In PVD, the source material is typically in a solid state. Through various methods like sputtering or evaporation, the material is physically transformed into the vapor phase, meaning it becomes a gas without undergoing any substantial chemical changes [8]. CVD is different from PVD, another conventional thin film deposition method, which involves chemical reactions at a

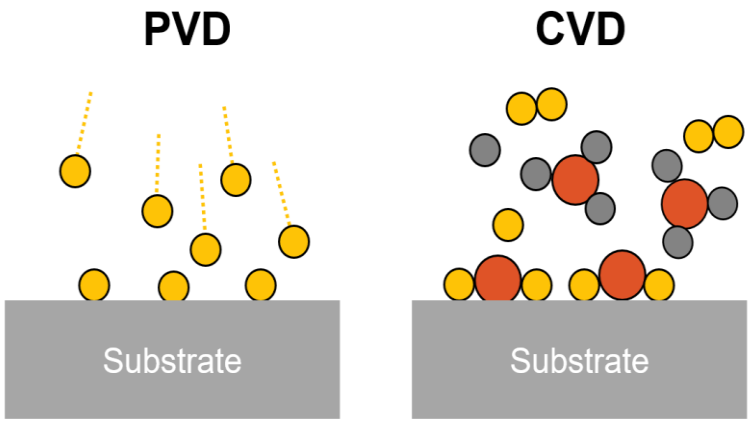

Figure 1.2: Schematic illustration of the physical and chemical vapor deposition methods.

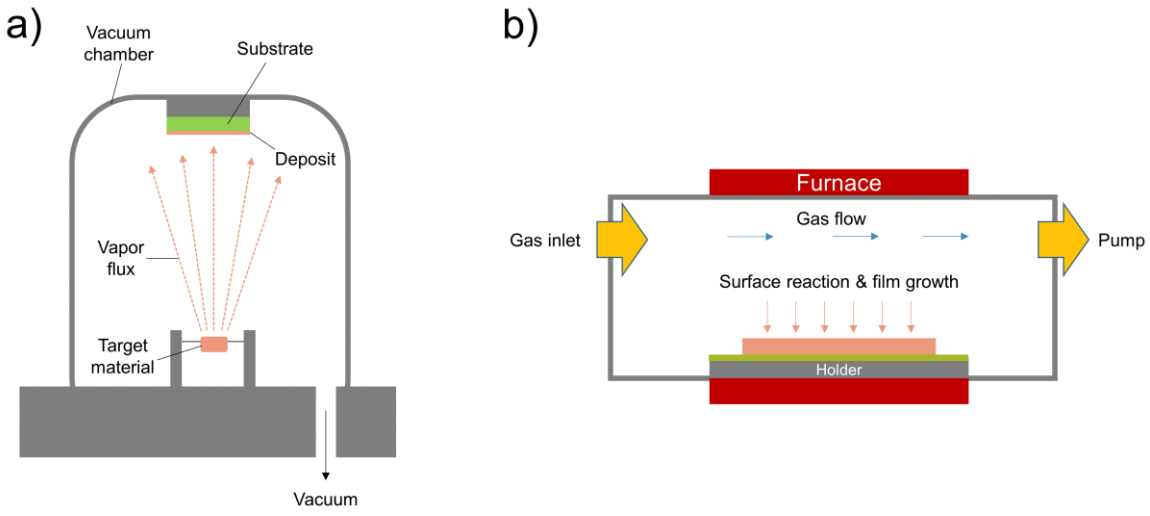

Figure 1.3: Schematic diagram of a) a thermal evaporation system (common PVD process) and b) a chemical vapor deposition (CVD) system.

high temperature in the gas phase to produce a thin film on the substrate [9]. The gaseous source condenses onto the substrate, where it forms a thin film. These methods can coat a wide range of materials with a uniform thin film onto a large area with atomic-scale control. For this reason, both methods are widely used in the semiconductor device industry.

Fig. 1.3a shows a thermal evaporation process which is one of the most common and widely used PVD processes. As shown in the schematic, the solid-state target source will be vaporized by physically induced high energy (thermal energy in this case) [8] and its atoms are transported through vacuum conditions to the substrate surface and deposited as thin film. In the CVD method, single or multi-precursor gases are flowing into the chamber through a gas inlet and a chemical reaction occurs on the heated surface of the substrate to form the thin film [9] shown in Fig. 1.3b. Both CVD and PVD methods provide uniform large-area deposition and high-quality thin films.

The deposition rates can be controlled precisely to create reproducible thicknesses for the fabrication of electronic devices.

Thin-film transistor device fabrication consists of a series of deposition and etching processes to pattern device structures that are integrated onto a substrate. These devices consist of high-quality thin films grown by PVD or CVD that are then patterned and defined through photolithographic techniques to form patterned etch masks on the thin-film surfaces. A subtractive etching approach is then implemented to remove material in the surrounding field that is not masked, defining a pattern on the thin-film layer. However, these conventional subtractive processing techniques require ultra-clean high-vacuum conditions, high-temperature processing, multi-step photolithography patterning with expensive photomasks, and chemically hazardous materials.

One method to alleviate these constraints in the device fabrication process is replacing these complex integration schemes with an additive technique that can deposit and pattern the device structure simultaneously. The use of IJP techniques may be a viable approach to alleviate these problems, but challenges remain in the development of electronic inks and their patterning for device fabrication that need to be overcome. Overcoming these challenges would pave the way to enable high-quality thin films that may be scaled to large areas for manufacturing.

1.3 Printing technology

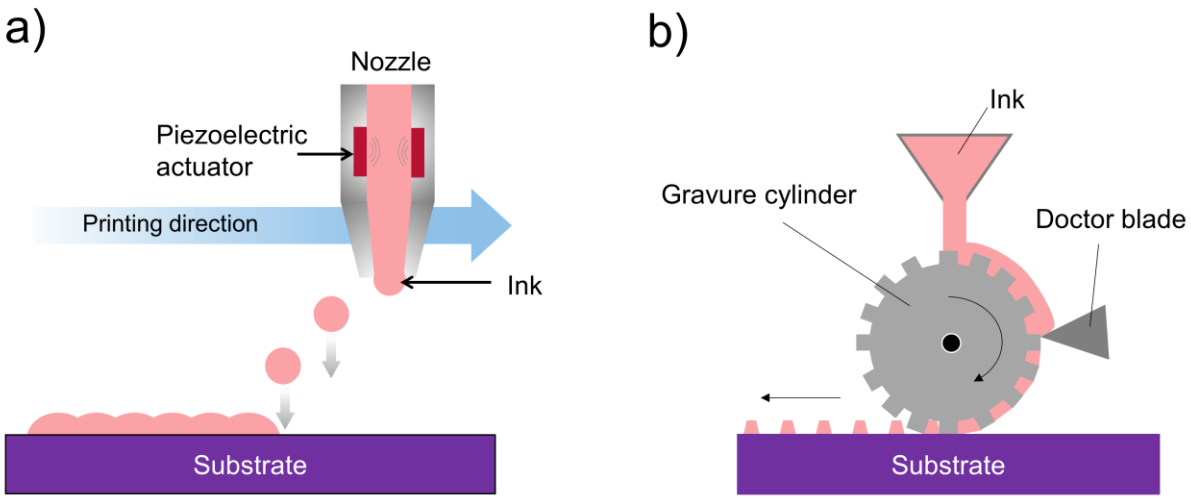

Figure 1.4: a) Inkjet printing as a non-contact printing vs b) a gravure printing as a contact printing.

The most attractive feature of printing technology is the capability to directly deposit materials on the substrate with a predesigned pattern. It is the additive processing approach that simplifies the fabrication of electronic devices compared to conventional approaches. This method enables a maskless fabrication process and continuous process in a single assembly line which enables roll-to-roll (R2R) processing that may allow device processing in an ambient air environment, making it a cost-effective alternative compared to conventional vacuum deposition processes.

Printing technology is classified by contact and non-contact printing methods. Non-contact printing methods enable the deposition of material on any surface without contamination on the substrate. In the non-contact printing method, such as IJP, the ink droplet is expelled from the printing nozzle onto the surface of the substrate. The volume and frequency of the ink droplet can be controlled by the actuation of the printhead, usually through a piezo or thermoelectric transducer with the electrical signal shown in Fig. 1.4a. By moving the nozzle or substrate, the ink droplet can

be jetted only where needed to make a specific pattern. This drop-on-demand approach minimizes materials waste, simplifies electronic device fabrication, and potentially reduces the cost of manufacturing.

On the contrary, contact printing methods are another approach to print large volumes that may be used for device fabrication. As a contact printing method, gravure printing is a widely used technique for printing thin film devices with high-throughput and high-resolution [10]. The carved metal pattern of the cylinder transfers the ink in the cylinder cavities to the substrate surface shown in Fig. 1.4b. The excess ink from the printing cylinder is scraped off by the doctor blade. This technique, unfortunately, requires high-viscosity liquids which cause difficulty of transferring ink [11] and inherently contact to the substrate that may result in contamination and remaining surface residue [10]. In this work, the IJP process was used given its lower viscosity ink usage, high registration accuracy, its relatively high reproducibility, and its proven capacity for fabricating thin-film transistor devices [10].

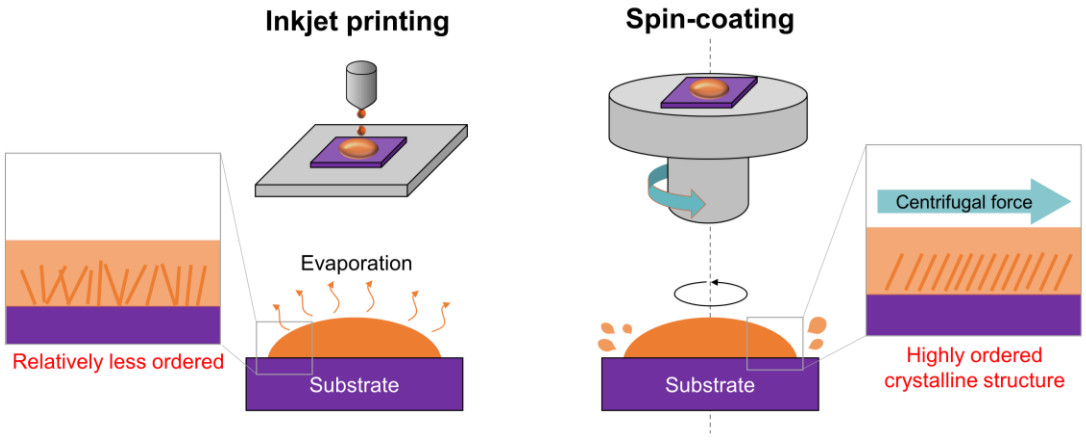

Figure 1.5: Schematic illustration of inkjet printing and spin coating process.

While IJP has many advantages as an additive process over conventional microfabrication techniques, there are challenges that still prevent its pervasive use in the electronics industry. Fig. 1.5 compares two different deposition methods (IJP and spin-coating) using liquid materials. IJP technology enables the direct deposition of materials on the substrate with high accuracy achieved by the ejection of a liquid droplet onto the substrate surface. Once the droplet forms on the surface it starts to dry and forms a film. During this drying process, several challenges need to be overcome for the creation of a uniform high-quality film to form. One challenge is poor crystallinity of the organic semiconductor (OSC) that is the main challenge of IJP arising from the evaporation dynamics of the ink, hampering the carrier transport properties of the TFT devices [12].

The spin-coating method possesses a different deposition mechanism compared to IJP. By spinning the substrate at a high rotational speed, the liquid materials on the substrate are spread outward by the imposed centrifugal force. After spinning, the liquid uniformly coats the overall surface. When the solvent is fully evaporated, a highly ordered crystalline structure of OSC thin film forms [12-14]. On the contrary, the IJP process produces relatively poorer crystallinity due to the absence of an external force to help form crystalline domains in the OSC thin film. This property is a major reason for lower TFT performance fabricated by the IJP method due to the absence of centrifugal forces for printed droplets [12-14]. Crystallinity is an important aspect in determining the performance of TFTs and the deposition method has an effect on the ordering within a thin-film layer [15].

1.4 Inkjet-printed TFTs

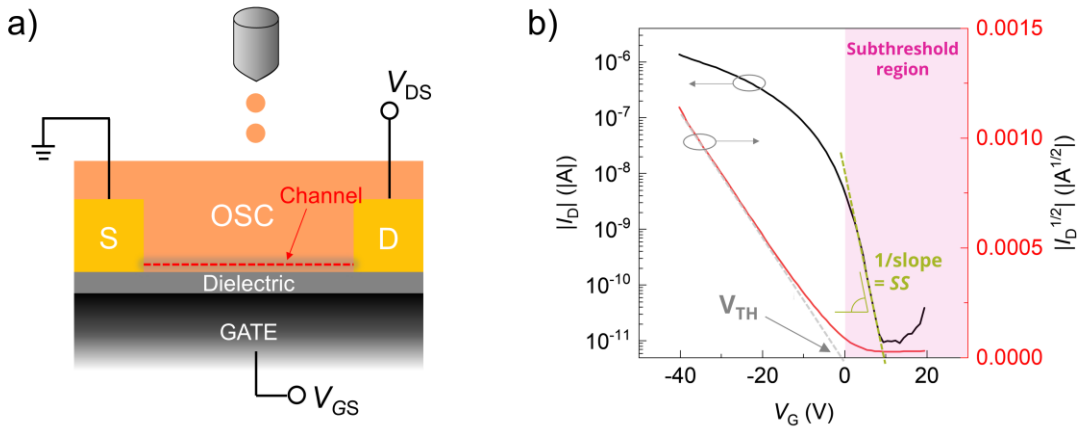

Figure 1.6: a) Schematic of BCBG TFT structure with applied gate bias larger than threshold voltage ($V_{GS} > V_{TH}$). The channel (accumulation layer) is formed underneath the inkjet-printed organic semiconductor film that is depicted by red dashed line. b) Example of transfer characteristics of common p-type channel TFT.

A TFT in its simplest description is an electrical switch and is the fundamental building block of electronic circuitry. The conventional inkjet-printed bottom contact bottom gate (BCBG) TFT structure is depicted in Fig. 1.6a. The current flow through the semiconductor is modulated by an applied gate bias (V_{GS}) that changes the electrical conductivity of the semiconductor between the source-to-drain electrodes. The applied gate voltage induces an electric field perpendicular to the surface of the semiconductor through the gate dielectric (gate oxide). The field induces an accumulation of charges in the semiconductor thin film near the oxide which forms a conductive channel layer. A horizontal electric field is created across the source and drain electrodes using an applied bias (V_{DS}) at the source and drain electrode, which induces charge transport from source to drain. On the contrary, when V_{GS} is removed or reduced, the channel layer is also diminished and the layer conductivity reduces, which causes the current flow to decrease and the device to be turned off. In this manner, the TFT functions as an electrical switch, turning on and off depending

on the applied gate bias. The current flow between the source and drain through the channel region (I_{DS} or I_D) is controlled by applied biases (V_{GS} and V_{DS}) and may be modeled by the gradual-channel approximation, which was first proposed by Shockley [16]:

$$I_{DS,sat} = \frac{W}{2L}\mu_{sat}C_i(V_{GS} - V_{TH})^2 \tag{1.1}$$

$$I_{DS,lin} = \frac{W}{L}\mu_{lin}C_i\left[(V_{GS} - V_{TH})V_{DS} - \frac{V_{DS}^2}{2}\right] \tag{1.2}$$

where $I_{DS,\text{ sat or lin}}$, W, L, and C_i are the drain current in saturation or linear regime, width and length of the channel, and the gate oxide capacitance, respectively. The organic thin film transistor (OTFT) works in two different operating regimes, the linear and saturation regimes. When $|V_{DS}|$ increases from 0 and is smaller than $|V_{GS}-V_{TH}|$, the I_{DS} linearly increases and is proportional to the applied $|V_{DS}|$ [17, 18]; this mode of operation is called the linear regime. Then, at the bias condition $|V_{DS}| \sim |V_{GS}-V_{TH}|$, pinch-off occurs in the channel region then the I_{DS} saturates even with higher $|V_{DS}|$ defining the saturation operation regime [17, 18]. The above equations are only valid when $|V_{GS}|$ is larger than $|V_{TH}|$. In this condition, the charge carriers can be accumulated and the conductivity of the semiconductor along the oxide-semiconductor interface increases, forming a one-dimensional potential distribution in the channel region [19]. By using this equation, the field-effect mobility in the linear (μ_{lin}) or saturation regime (μ_{sat}) can be extracted, and they are independent of applied bias conditions. If the semiconductor has higher carrier mobility under active operation, it will have better charge transport properties by showing an enhanced current level (I_{DS}). Therefore, field-effect mobility is considered as one of the most important device parameters for evaluating the TFT performance. The mobility of OTFT is mostly affected by the carrier transport which is in turn dependent on the ordering within the organic semiconductor.

Hence, the crystallinity can be varied between the organic semiconductors and is highly affected by the deposition method and surface condition of the substrate.

This thesis introduces a novel method to improve the crystallinity of organic semiconductors itself, especially polymeric semiconductors, by using hybrid nanocomposite semiconductor inks. By applying this method, the improved field-effect mobility of the inkjet-printed OTFTs was demonstrated and analyzed within the research presented in this thesis.

To analyze the transport properties of the TFTs formed using different ink formulations, the current-voltage (*I-V*) characteristics of the devices were studied. The transport properties were investigated in the linear or saturation mode to extract the field-effect mobility (μ_{lin} or μ_{sat}) using equations 1.1 and 1.2. The threshold voltage (V_{TH}) was extracted from the transfer characteristics (I_{DS} *vs.* V_{GS}) of the TFTs as shown in Fig. 1.6b. As depicted in the figure, V_{TH} is estimated by the linear-extrapolation method from the *I-V* data in the square root of the I_{DS} vs. V_{GS} plot. The extrapolated intercept with the V_{GS} axis gives the V_{TH}. Ideally, the linear and saturation field-effect mobility should be similar in the range. However, in real devices the μ_{lin} is usually smaller than μ_{sat} due to a contact resistance (R_C) [18, 20] which can appear for various reasons such as the formation of a Schottky barrier [21], poor device process and structure [22], and undesired nonuniform structural disordering of the organic materials [23].

In the linear regime (low V_{DS}, $V_{GS}-V_{TH} >> V_{DS}$), the device operates as a resistor in the channel region, and the resistance of the channel (R_{CH}) mostly depends on the gate bias (V_{GS}) ($I_{ds,\ lin} = V_{DS}/R_{CH}(V_{GS})$). Since the total resistance (R_T) in TFT includes both channel and contact resistances which are connected in series ($R_T = R_{CH} + 2R_C$), the voltage drop occurs across the semiconductor/electrode interface due to the R_C, and the V_{DS} applied in the channel region should

decrease in the linear regime [24]. On the contrary, in the saturation regime ($V_{GS}-V_{TH} < V_{DS}$), the R_C is usually considered to be negligible, since the I_{DS} is independent of V_{DS} from the gradual channel approximation equation (eq. 1.1). Hence, the saturation field-effect mobility is more adequate to describe the intrinsic charge-carrier mobility of the organic semiconductor materials [20, 25]. However, recent studies have reported the impact of R_C in the saturation regime and reported R_C can degrade the drain current [26, 27]. It may become a more severe problem in inkjet-printed metal electrodes for TFT applications. This effect and its analysis will be presented in the last chapter of this thesis.

The other electrical parameter of the TFT is the sub-threshold swing (*S.S.*) which is expressed in units of mV/decade:

$$S.S.\left(\frac{\mathrm{mV}}{\mathrm{decade}}\right) = \frac{dV_{GS}}{d(logI_{ds})} \tag{1.3}$$

In the range of V_{GS} under V_{TH} defined as a subthreshold region, the switching speed of the transistor can be evaluated by the *S.S.* which is the reciprocal value of the slope of the curve (log-scale I_{DS}-V_{GS}, Fig. 1.6b) in this region. The theoretical minimum limitation at room temperature of the *S.S.* is 60 mV/decade (ln(10)kT/q). It is mostly affected by the dielectric capacitance (C_i), so to minimize the S.S, and increase the switching speed of TFT, high-*k* dielectric materials (*e.g.* hafnium-based oxide material) have been applied in related works using pentacene-based OTFTs; the devices showed a low S.S. of 0.13 V/decade [28]. On the contrary, *S.S.* is degraded by the trap states at the interface between organic semiconductors and the gate dielectric [29]. The charge carriers can be trapped within these states and immobilized, but the trap states should be filled beforehand, as this enables the accumulation of charge carriers, finally leading to the formation of the channel region [30]. Therefore, the increased presence of trap states at the interface adversely

affects the switching speed of OTFTs and contributes to a degradation in their *S.S.* [31-34]. Although this work does not focus on the investigation of this electrical feature of TFTs, it remains an important aspect of the TFT performance and its electrical stability.

1.5 Printable materials

The TFT is made of three different types of materials, including the semiconductor, the dielectric, and the metal contact. For additive processes using IJP, these materials should be solution-processed to be printable. Conductive inks have been produced with a variety of materials, including metal nanoparticles (Au, Ag, Cu) [35-37], carbon-based ink (CNT or graphene) [38, 39], conductive polymer (poly(3,4-ethylenedioxythiophene):poly(styre-nesulfonate) (PEDOT:PSS) [40, 41], and more, for use as metal electrodes in electronic circuits. Several dielectric materials, such as polyvinylphenol (PVP) [42], polyvinyl alcohol (PVA) [43], fluorous polymer (Cytop) [44], polymethylmethacrylate (PMMA) [45], and ion gel (electrolyte gated TFTs) [46], have received a lot of attention for printing technology. For the gate dielectric, it is desired for dielectric material to have high capacitance with thinner layers and barrier a high electric field to withstand high breakdown voltage. Furthermore, the interface state between the dielectric and the semiconductor should be considered and evaluated to improve device performance, and get a stable electrical characteristic of devices since the presence of interface trap charges adversely affects *S.S* and leads V_{TH} variation [30]. However, while both metal and dielectric materials hold significance in device performance, it is essential to emphasize that semiconductors play the most critical role in substantially influencing device performance, especially carrier transport.

For printable semiconductors, OSC is widely used and studied for its good solution processability. OSC is classified into small molecule and polymeric semiconductors, i.e.,

conjugated polymers. Small molecule semiconductors generally have better charge transport property and show higher mobility than polymer semiconductors [47] since it has better crystallinity as semi-crystalline structure *e.g.* pentacene. However, it is commonly not easy to deposit and form a uniform high-quality thin film by inkjet printing [48], requiring several parameters to be optimized (where the surface conditions of the substrate, geometry of the feature and printing conditions play a role in the final printed features [49]). On the contrary, polymeric semiconductors present numerous advantages when employed in inkjet printing. They are generally more processable from solution than small molecule semiconductors since polymers have higher molecular weights and longer chain structures, which result in improved solubility in common organic solvents [50]. Moreover, these polymers are capable of being deposited on surfaces with continuous thin film, smooth and uniform surface, owing to their inherently amorphous structure and high viscosity relative to small molecule semiconductors. [47].

1.5.1 Semiconductor inks

In this work, two polymer semiconductors, regioregular poly(3-hexylthiopene-2,5-diyl) (rr-P3HT) and diketopyrrolopyrrole thieno[3,2-b]thiophene (DPPT-TT) were used for inkjet-printed TFTs. First, P3HT has been studied and developed as a channel material for TFT applications over the last few decades. Therefore, it is suitable as a prototype host material for novel hybrid nanocomposite semiconductor ink. P3HT is a p-type and conjugated polymeric semiconductor, and it has a self-assembly property to form highly ordered semi-crystalline films with good air-stability [51]. After developing and studying hybrid ink based on P3HT, (discussed in Chapter 3), the concept of the hybrid semiconductor was applied to other polymers. DPPT-TT which has

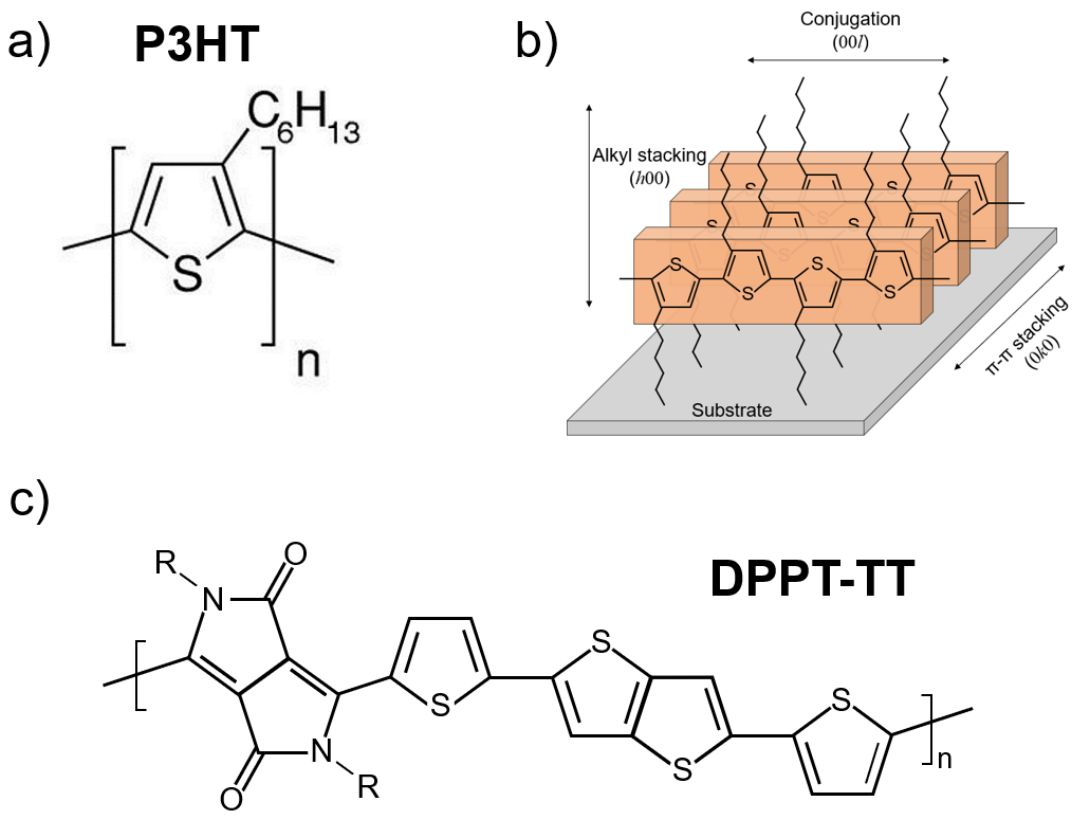

Figure 1.7: Organic polymer semiconductors, P3HT and DPPT-TT. a) The chemical molecule structure and b) stacked structure of P3HT. c) Molecular structure of DPPT-TT.

received great attention as a next-generation polymer (also known as donor-acceptor copolymer), has shown high field-effect mobility in the order of ~10 cm^2/Vs [52]. Moreover, it has ambipolar characteristic which is beneficial for complementary metal-oxide semiconductor (CMOS) electronic circuits. This study will be presented in Chapter 4.

Polymeric semiconductors typically have poor charge transport property even though it has various benefits and advantages for IJP TFT applications. To address this challenge, the fundamental understanding of the charge transport mechanism in polymeric semiconductors should be necessary because it has different structural features compared to inorganic

semiconductor which has single crystalline lattice structure such as silicon. Fig. 1.7 shows the chemical molecular structure as a monomer and schematic illustrations of the microstructure of P3HT. In the stacked structure of this conjugated polymer (Fig. 1.7b), monomers are repeated with π-conjugation and alkyl side chain (top and bottom) by forming a polymer backbone [53]. The highest charge transport property is related to these molecule chains (00*l*) through the backbone [54]. The orange box indicates the 2D P3HT layer has a stacked lamellar structure. Intermolecular charge transport is dominant through the π-π stacking (0*k*0) in this crystalline structure [54]. Moreover, the molecules are lying parallel to the edge of the substrate which is known as edge-on orientation which is the desired orientation for the charge transport through (0*k*0) [55, 56]. The charge transfer through the alkyl stacking direction is negligible (*h*00) [57], but it is a good indicator to evaluate the crystallinity of the polymer structure. In the mesoscale structure, the polymer has crystalline and amorphous domains simultaneously [57] even if, schematically presented in Fig. 1.7b, conjugated polymer chains are stacked in highly ordered structure as crystalline regions. Then in the better crystalline structure inter- and intramolecular interactions can be improved through all axes (00*l*), (0*k*0), and (*h*00). This microstructure characteristic can be analyzed by using spectroscopy systems such as UV-vis (ultraviolet-visible) and XRD (X-ray diffraction). However, charge transport properties are degraded in amorphous regions, a major difference to single crystalline inorganic semiconductors which can have very high mobility (larger than ~10 cm^2/Vs). Therefore, enhanced crystallinity of the polymeric film is key to improving the field-effect mobility of OTFT.

As described in the previous chapter, field-effect mobility is an important electrical parameter of the TFT since it is closely correlated to device performance and efficiency. Polymeric-based TFTs have relatively poor field-effect mobility compared to inorganic semiconductor materials.

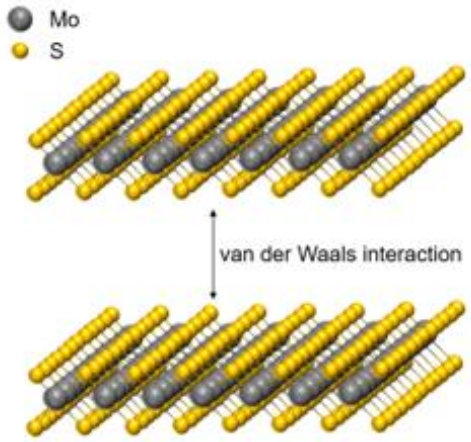

Figure 1.8: Atomic structure of layered MoS_2.

Since thin-film polymeric semiconductors have both semi-crystalline and amorphous structure, the low crystallinity of the polymeric microstructure limits the charge carrier transport in the whole polymer matrix. In other words, P3HT films have good charge transport properties through the molecular chains, but it has very poor charge transport through the disordered molecules in the amorphous region. On the contrary, single, or polycrystalline (silicon) inorganic semiconductor TFTs generally have higher field-effect mobility than polymer channel TFTs, but these semiconductors are not as adaptable for low temperature and solution processes. Meanwhile, graphene-like two-dimensional (2D) materials have been developed to be used in the form of a

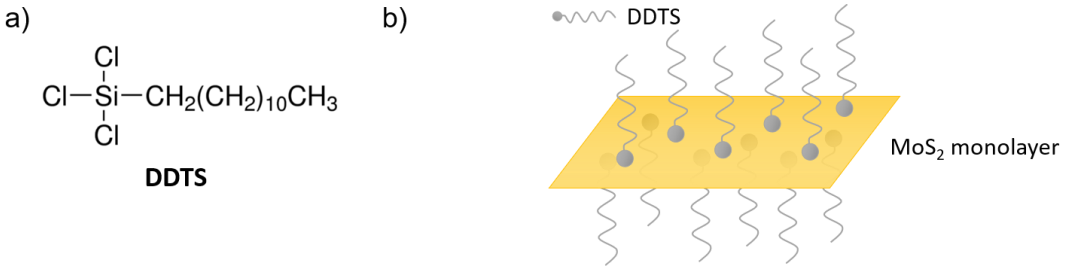

Figure 1.9: a) Chemical structure of DDTS and b) schematic illustration of DDTS treated on the MoS_2 surface.

nanoparticle suspension. Recently, there have been many attempts to print transition metal dichalcogenides (TMDCs) itself, also known as 2D semiconductors, since it has superior charge transport properties compared to organic semiconductor [58, 59]. Among the 2D materials, molybdenum disulfide (MoS_2) has been studied most and attracted great attention for its various merits of electrical, optical, and mechanical properties [60, 61]. It also has very high carrier mobility from monolayer MoS_2 (50~200 $cm^{-1}/V \cdot s$) [62, 63]. Furthermore, MoS_2 has hole transport [64], few-layer and monolayer structures having carrier mobilities of 480 $cm^2/V \cdot s$ [65] and 26 $cm^2/V \cdot s$ [66], respectively.

In Fig. 1.8, the atomic structure of MoS_2 is shown with the interlayer bonding between each layer made with weaker van der Waals forces [67]. Due to these weak Van der Waals forces, the vertically stacked structure can be easily detached by mechanical exfoliation [68]. However, it is hard to make a liquid form of MoS_2 since it does not dissolve in any solvent. One approach to use this material within a solution is to disperse thin layers of MoS_2 (nanosheets) into the liquid as a suspension. If the MoS_2 nanosheets are uniformly suspended in the liquid, it may be possible to deposit the suspension over a large area of uniform thickness in solution processible applications. Recent work of printed MoS_2-based devices showed relatively poor electrical characteristics, having low on/off current ratios [69, 70]. The result was attributed to undesired impurities introduced as traps in the liquid phase processing [69]. It may be addressed by improving the flakes arrangement in the film during the deposition process [70], but it still suffers from a very poor on/off ratio and carrier mobility (~10^{-4} $cm^{-1}/V \cdot s$). For this reason, in this work, MoS_2 is incorporated into a semiconducting mixture as an additive. The MoS_2 is added as a suspension into a polymer solution to enhance the charge transport property of the polymer for printed TFT applications.

It is important to have a stable MoS_2 suspension to improve the MoS_2 arrangement in the deposition pattern and to avoid reaggregation which may result in non-desired issues during fabrication such as nozzle clogging. The functionalization of the MoS_2 surface is a way to maintain a well-dispersed suspension of MoS_2 in a solvent. A recent report by Yu, *et al.* revealed that alkyl-trichlorosilanes (ATSs) surfactants prevent to reaggregation of MoS_2 in solution processing [71]. The other previous study also reported that the ATSs are used to treat the surface of the WS_2 (Tungsten disulfide) nanosphere (another TMD material) to enhance the tribological properties of the material [72]. In Fig. 1.9, trichloro(dodecyl)silane (DDTS) one of the ATSs to modify the surface of the MoS_2 layer may be used to make a stable MoS_2 suspension. To be used for electronic inks in inkjet printing, the restacking of MoS_2 layers in the suspension needs to be prevented, and DDTS is suitable for this role. It will be added to MoS_2 suspension as a surfactant during the process and its silane group bonds to the dangling bonds of the MoS_2 monolayer surface [71]. The enhanced stability of MoS_2 suspension (increased dispersion level) helps to form a uniform distribution of MoS_2 flakes in the polymer solution.

1.5.2 Metal ink

Printable metal ink is necessary to fabricate TFTs in a roll-to-roll (R2R) manufacturing process which enables continuous high-speed production over large areas [73]. In comparison to other conductive materials utilized in ink, silver nanoparticle (Ag NPs) inks stand out as the most appealing candidate. This distinction arises from their commendable electrical conductivity, even in the presence of conductive silver oxides, while copper oxide, on the other hand, does not display such conductivity. Moreover, Ag NPs are economically advantageous as they are more cost-

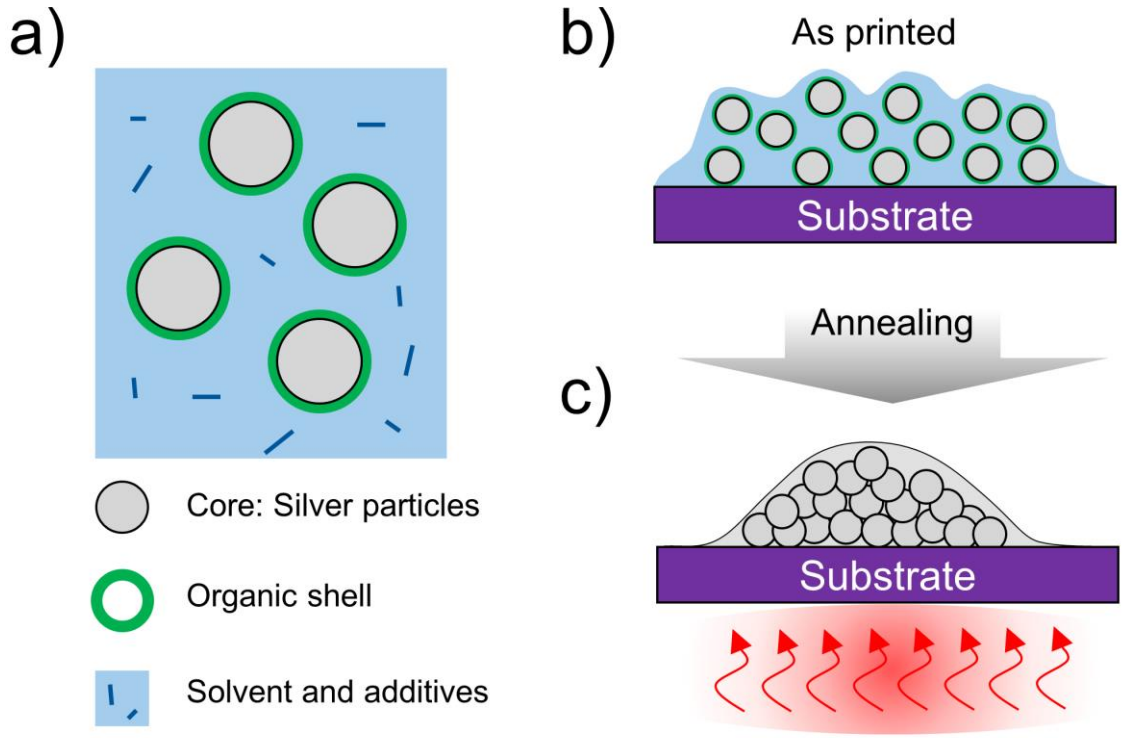

Figure 1.10: (a) Schematic illustrations of colloidal solution of silver nanoparticles and (b) as printed silver nanoparticle ink on the substrate. (c) During annealing process, solvent and additives are removed and organic shells are sintered.

effective than precious metals like gold. Additionally, Ag NPs exhibit superior adhesion to substrate surfaces when contrasted with other materials like carbon nanotubes (CNTs) or graphene. [74]. Various shapes of silver nano particles can be synthesized such as a planar structure (triangles, 5 or 6 diagonal, and round surfaces) and a three-dimensional structure (cubic and pyramidal) [75]. The morphology of nanoparticles significantly influences their optical, electrical, magnetic, and catalytic properties. Among different shapes of NPs, spherical particles, characterized by minimal surface area for a given volume, demonstrate enhanced thermodynamic stability [76].

Figure 1.10 shows how Ag NPs ink can be used in printing methods and forms into a thin film. Ag ink consists of silver nanoparticles encapsulated by an organic shell suspending in the solvent with additives which help make stable dispersions and separate particles from others. When this printed ink is annealed at the sintering temperature (or reaction temperature), the solvent and additives are removed. Then the remaining organic shell also breaks down, and the core silver nanoparticles start to agglomerate and merge with neighboring particles [77]. Finally, continuous silver thin film forms during this sintering process and the electrical conductivity of the printed ink begins to change. However, printed metal electrodes have inherent challenges. It has relatively poor film quality – structural features such as surface roughness compared to metal films deposited by conventional methods such as PVD or CVD (introduced in Chapter 1.2). Moreover, it is hard to obtain a fine edge pattern in the solution-processed metal thin film compared to the conventional photolithography process. These structural deficiencies of printed thin-film metals will result in increased contact resistance (R_C) when it is used as source and drain (S/D) electrodes in TFTs. Nevertheless, printing thin-film metals is a critical component to realize the future electronics which requires fully inkjet-printed TFTs and a roll-to-roll process which is one goal of inkjet-printing technology. The effect of the process conditions and the geometry of the printed metallic lines will be described in the last chapter in more detail. Above all, the enhanced carrier mobility of printable semiconductors by using novel hybrid nanocomposite is the primary goal of this thesis. Therefore, novel hybrid ink is investigated thoroughly with vacuum-deposited gold electrodes for preliminary research. The study of the effect of inkjet-printed Ag S/D will be followed in chapter 5.

Chapter 2
Methods

2.1 Semiconductor ink

In this study, a hybrid nanocomposite semiconductor ink was developed by blending polymeric semiconductors as a host with MoS_2 as an additive. Both polymer semiconductors and MoS_2 are prepared in a solution phase for inkjet printing.

The polymeric semiconductors P3HT and DPPT-TT are dissolved in 1,2-dichlorobenzene (DCB) in this study, and the active layer of the TFT will be created by inkjet printing this solution. The organic solvent used for these two polymers was carefully chosen because, according to earlier studies [78], DCB has a high boiling point that causes polymer solutions to dry slowly. This characteristic will allow for improved crystallinity in the dried thin film.

Using an amber glass vial to avoid exposure to ambient light [79], solid polymer powder that had been precisely weighed was placed with an estimated amount of DCB poured into the same glass vial to create a suspension with a 10 mg/ml concentration. Afterward, the glass vial was thoroughly capped and wrapped with parafilm. Then, the polymer solution in the vial was annealed on a hot plate at 85 °C for 1 hour under ambient conditions. All the solid polymer powder in the vial was thoroughly dissolved into DCB without any sediment after the annealing procedure. These are ready to be put onto an ink cylinder to be printed with an inkjet printer. Before being used in the inkjet printing process, the polymer solution, after 1 hour of annealing, was stored on the hotplate to ensure that it remained well dissolved and to prevent any aggregation at room temperature [80].

2.1.1 MoS_2 suspension

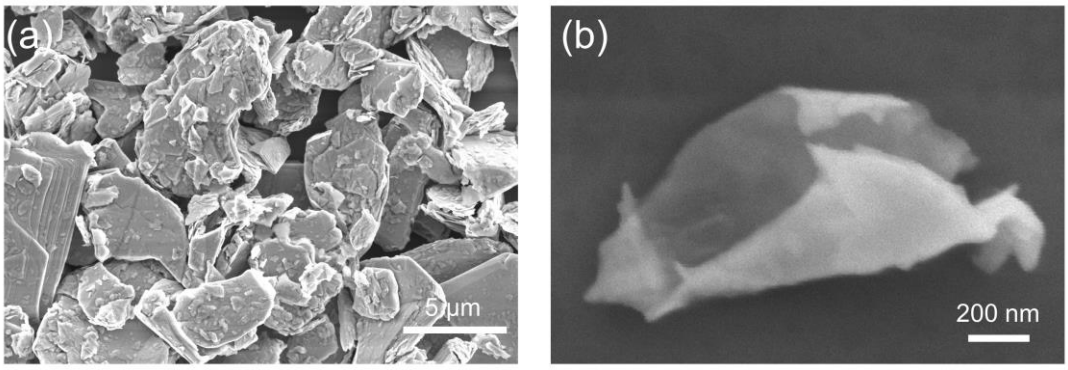

Figure 2.1: SEM image of inkjet-printed MoS_2 nano powder and few-layer MoS_2 nanosheets.

A glass vial containing 1 mg/ml MoS_2/DCB was sonicated for two hours to produce the nanosheet suspension (LS-04D Digital Ultrasonic Cleaner Bath, Limplus). Due to the mechanical force generated during the sonication process, the bulk of MoS_2 is exfoliated into thin layers during this process. The generated MoS_2 dispersion could be inkjet printed under these exfoliation conditions, and scanning electron microscope (SEM) analysis of its structure was performed (Fig. 2.1). Micrographs show bulk MoS_2 nanopowder stacked in large clumps having diameters of a few micrometers (Fig. 2.1a). They were then separated into layers during the sonication process, and the few-layered nanosheet can be observed by SEM with a lateral size of about 1 micrometer, as shown in Fig. 2.1b. Therefore, the MoS_2 nanosheets used in inkjet printing have varying thicknesses (indicating a few layers) and lateral widths. For electronics, thinner and larger lateral MoS_2 nanosheets are desired in order to scale down future electrical devices, scalable fabrication, and the creation of pristine surfaces of MoS_2. However, there is a trade-off to get thinner nanosheets, increasing the sonication power results in smaller size of nanosheets due to the scission of the flakes [81].

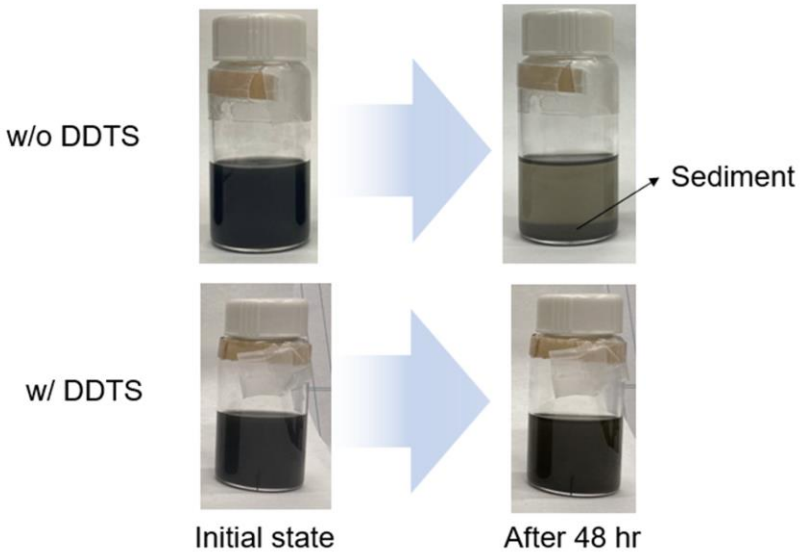

Figure 2.2: The photography of the MoS_2 suspensions with or without DDTS. Initial state of the suspension was captured after 2 hr ultra-sonication.

As stated in Section 1.5, the functionalized MoS_2 surfaces were made using the self-assembled monolayer DDTS in order to increase the few layers of thin MoS_2 nanosheet (or, to improve the exfoliation process) to obtain a stable suspension. In the sonication process, the silane group of DDTS forms a bond with dangling bonds at the surface of MoS_2 layers [71]. 0.5% (volume/volume) DDTS is used to create MoS_2 suspension in DCB. The functionalized surface inhibits the structures from stacking up again and produces a well-dispersed and stable MoS_2 suspension in liquid over a period of days. The effect of DDTS on the MoS_2 suspension resulted in an observable visible change (Fig. 2.2). Both MoS_2 suspensions with and without DDTS appear to have a dark black color in their initial stage (right after ultrasonication for two hours), which shows that the MoS_2 nanopowders are evenly distributed throughout the dispersion. However, the MoS_2 suspension prepared without DDTS had sediment and the liquid became transparent after 48 hours. This observation was because the exfoliated MoS_2 flakes agglomerated over time and fell

out of the suspension, whereas the suspension prepared with DDTS maintained its well-dispersed state. The findings of this study demonstrated that DDTS actually stabilized and coated the MoS_2 nano powder. As a result, the initial condition of the DDTS treated MoS_2 dispersion may contain more nanosheet layers with thinner layers than the other. In Chapter 3, this assumption will be verified with UV-vis analysis and determine whether or not this prepared MoS_2 nanosheet is truly useful for polymers to have improved charge transfer properties. The effect of the surfactant on device performance will be covered in Chapter 3 in order to look at the relationship between the density of MoS_2 nanosheets and a polymer semiconductor in greater detail.

2.1.2 Hybrid nanocomposite ink

As described, a hybrid nanocomposite ink was created by combining the prepared MoS_2 suspension into the polymeric solution. The entire procedure for the formulation of hybrid ink is depicted in Fig. 2.3. A different volume of MoS_2 suspension was mixed with a fixed volume of the polymer solution, as shown schematically on the bottom right in Fig. 2.3, to produce suspensions with various concentrations of MoS_2 in the solution. A higher concentration of MoS_2 in the solution, such as 6 wt%, may be a limitation for inkjet printing, since at this concentration, the ink frequently causes nozzle clogging (60 μm orifice) and was difficult to inkjet. The MoS_2 nanosheets were then thoroughly distributed in the polymer solution by sonicating the mixtures for 30 minutes.

In this hybrid semiconductor system, a polymer was the host solution and MoS_2 nanosheets were the additive. Electrically in the band diagram of each material (see Fig. 2.4), the highest-occupied molecular orbital (HOMO) level of polymers (P3HT and DPPT-TT) [82-85] and valance band maximum (VBM) of MoS_2 nanosheets [86, 87] lie in around – 5.1 ~ 5.3 eV that was an advantage for p-type transport. Since DPPT-TT is an ambipolar semiconductor, n-type transport also needs to be considered. The lowest-unoccupied molecular orbital (LUMO) level of DPPT-TT and

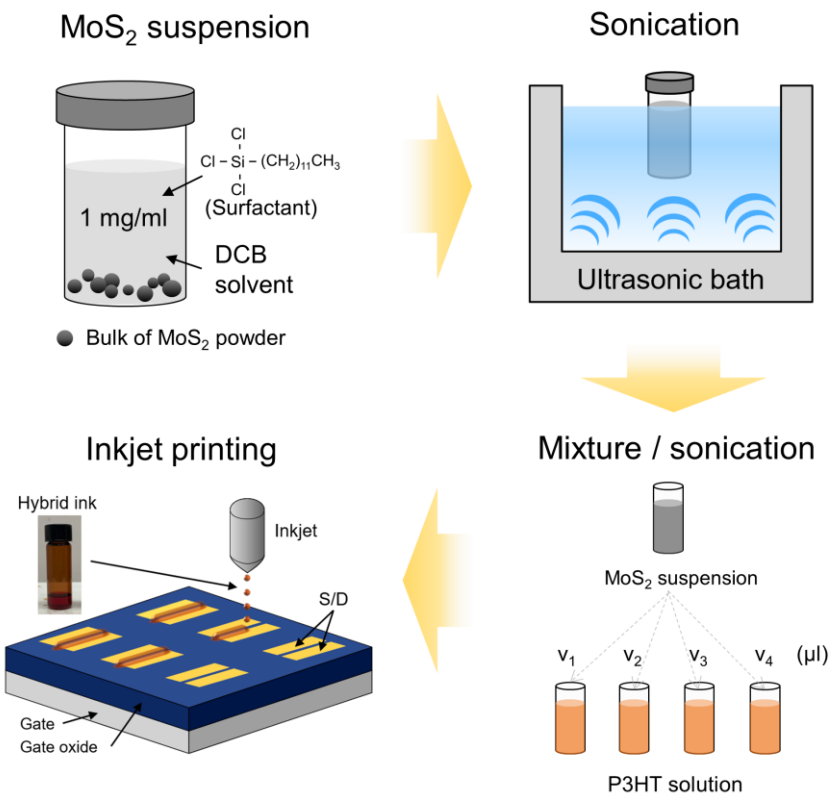

Figure 2.3: Schematic illustrations of the overall fabrication process of inkjet-printed hybrid channel TFTs. MoS_2 suspension is prepared by adding bulk MoS_2 powder in DCB as a solvent and 0.5 v/v % DDTS in a glass vial. The suspension is sonicated for two hours in the ultrasonic bath. Well dispersed MoS_2 suspension is mixed with P3HT solution with different volumes (from V_1 to V_4) to make different concentrations of a suspension in the hybrid ink. The ink is inkjet-printed on an array of S/D electrodes with a single ejector printhead.

conduction band minimum (CBM) of MoS_2 lie in around – 4 eV [88], thus this hybrid system has such a small energy barrier of 0.07 eV for electron transfer between these two materials. From the band diagrams, the energy level is well aligned for carriers to transfer between the semiconductor materials in this hybrid semiconductor system.

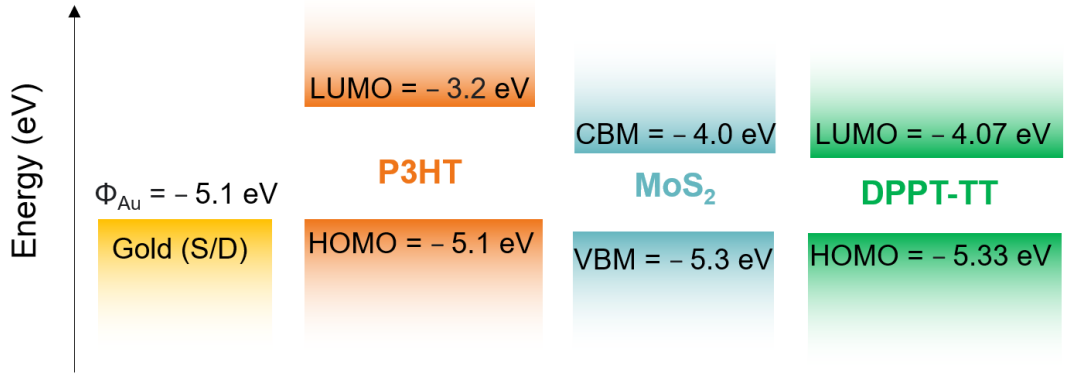

Figure 2.4: Energy band diagram of materials used for inkjet-printed TFTs showing energy-level offset between contact electrode (gold S/D) and each semiconductor.

Moreover, MoS_2 ideally has a single crystalline structure on its pristine surface because it is a two-dimensional inorganic material. This property may be employed to increase the crystalline domains of polymers when it is introduced as a suspension in the polymer matrix. Functionalizing the surface with a self-assembled monolayer (SAM) (see Appendix B) may enable the polymers to form better crystalline structures along the interface between the MoS_2 and the polymeric solution creating a more highly ordered film. The schematic images of the polymer and hybrid microstructure are shown in Fig. 2.5. The coexisting amorphous and semi-crystalline domains of the polymer are schematically illustrated in the figure. Due to its pristine surface and single crystalline lattice, MoS_2 nanosheets may enhance the number of crystalline domains in the polymer when they are added to the structure. Therefore well-exfoliated MoS_2 nanosheets which has large lateral dimension are desired for nanocomposite thin film. A higher degree of crystallinity in the polymer can result in better charge transport characteristics and enhanced device performance. This effect will be investigated and described in the subsequent chapters of this thesis.

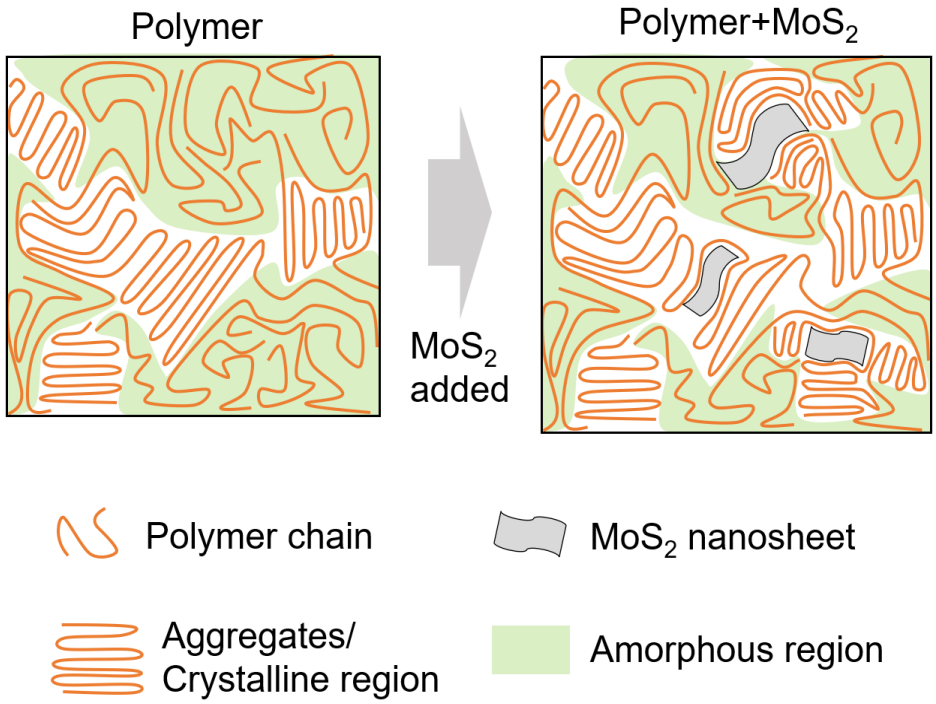

Figure 2.5: Schematic illustrations of mesoscale microstructure of polymer matrix and hybrid thin film.

2.2 Fabrication process of Inkjet-printed TFTs

2.2.1 Overview of TFT fabrication process

The fabricated devices have a BCBG TFT structure. The substrate is thermally grown 100 nm thickness SiO_2 on a heavily p-doped ($\rho \sim 0.0015$ Ω-cm and 0.03 Ω/sq, measured by four-point probe method) silicon wafer (thickness is 500 µm). The capacitance of the SiO_2 dielectric was evaluated by capacitance-voltage (*C-V*) measurement which is shown in Fig. C1. The cleaning process for the Si-wafer was accomplished by dipping in isopropyl alcohol, acetone, and sonicated in deionized water (DI-water) for 10 minutes each. After the cleaning, 3 and 30 nm thickness chrome/gold (Cr/Au) contacts were deposited using thermal evaporation and patterned using

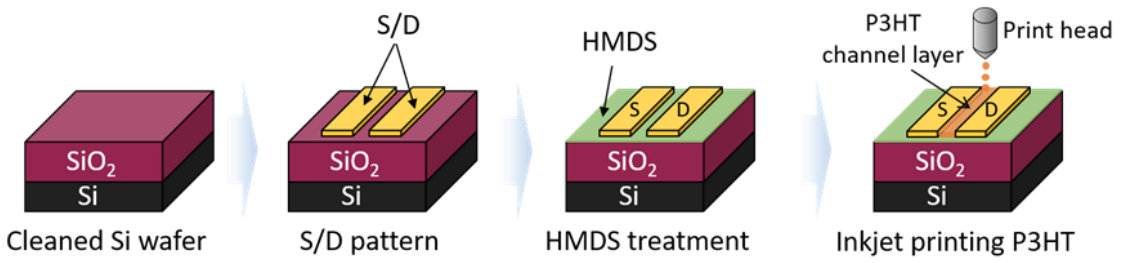

Figure 2.6: A fabrication process of inkjet-printed P3HT channel TFT.

conventional photolithography processes to form the source and drain (S/D) electrodes of the TFT. A thin Cr layer was used as an adhesion layer for gold thin film electrodes. The channel dimensions were defined by the width to channel length ratio (W/L) and was ~ 1,000 µm /10 µm. The contacts were then cleaned in an ozone environment generated by ultraviolet light followed by a solvent cleaning process using an ultrasonication bath consisting of DI-water, acetone, and isopropanol to remove residue on the surface of the substrate.

To create a hydrophobic oxide surface and avoid the formation of the coffee-ring effect, the substrate is dipped into hexamethyldisilane (HMDS) in a sealed glass petri dish and submerged overnight. Then, the substrate is rinsed with toluene and dried by blowing dry N_2. To verify the surface energy of HMDS-treated SiO_2, DI-water is drop-cast onto the substrate, using a micropipette with microliters volume, and the contact angle of the droplet is measured which is

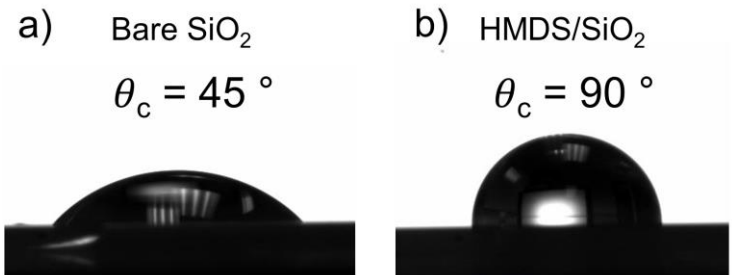

Figure 2.7: Contact angle measurement by dropping DI-water on (a) bare or (b) HMDS treated SiO_2 surface.

shown in Fig. 2.7. Since bare SiO_2 surface has higher surface energy than the HMDS treated surface, a lower contact angle is observed indicating a hydrophilic surface. The reproducibility of the HMDS treatment was confirmed by this measurement (increased contact angle after HMDS treatment on SiO_2 [89]), and deposited polymeric semiconductors on this surface were found to have improved crystallinity [90] and uniformity [91]. In this work, the condition of the substrate was systematically prepared to avoid the coffee-ring effect and achieve a uniform thickness of thin film which is discussed with more detail in Appendix A.

The prepared semiconductor ink was inkjet-printed onto the channel region that has pre-patterned S/D electrodes (Cr/Au) on the HMDS-treated substrate. After printing, the samples were annealed at 120 °C for 1 hour and cooled down in a vacuum. Then the fabricated devices were ready to be electrically characterized by *I-V* measurement in a vacuum environment, under dark conditions.

2.2.2 Detail of inkjet printing process

The inkjet printing for semiconductor ink was accomplished using a single nozzle (MicroFab) print head which has 60 μm orifice and piezo electric ejector mechanism. It was determined that the maximum size of the inorganic powder in the suspension was a few microns. Thus, the 60 μm orifice jetting nozzle was sufficient to jet the hybrid ink and prevent nozzle clogging. As previously noted, when the concentration of hybrid ink is increased to 6 wt%, the MoS_2 nano powder may be restacked and aggregated in the reservoir of the printer head, which causes nozzle clogging.

The stable jetting condition is preferred to provide a uniform printed pattern. The overall structure of the polymer in printed patterns is determined by the solution-processed polymer semiconductor, which is sensitive to and affected by the deposition process. Very stable jetting conditions, as seen in Fig. 2.8a, can be achieved by optimizing the pulse parameters given to the printer nozzle using a piezoelectric device. A single droplet with dimensions of 33 μm in diameter and 18 pl in volume was formed. The droplet velocity and jetting frequency are also important to develop uniform printing across large area in a short amount of time. The jetting frequency was 500 Hz. Droplet velocity was estimated as 1.67 m/s, estimated by the flying time of a single droplet from the nozzle to the surface of the substrate (working distance = 0.5 mm) of 0.3 ms (milliseconds). A precisely controlled uniform printed pattern can be produced in a large area, as demonstrated in Fig. 2.8b, due to its highly stable jetting condition. Printing single lines was tested with various drop spacings by varying the distance between each droplet position on the substrate. Without the erroneous printed pattern, every line is properly aligned. Achieving these conditions allows a reproducible

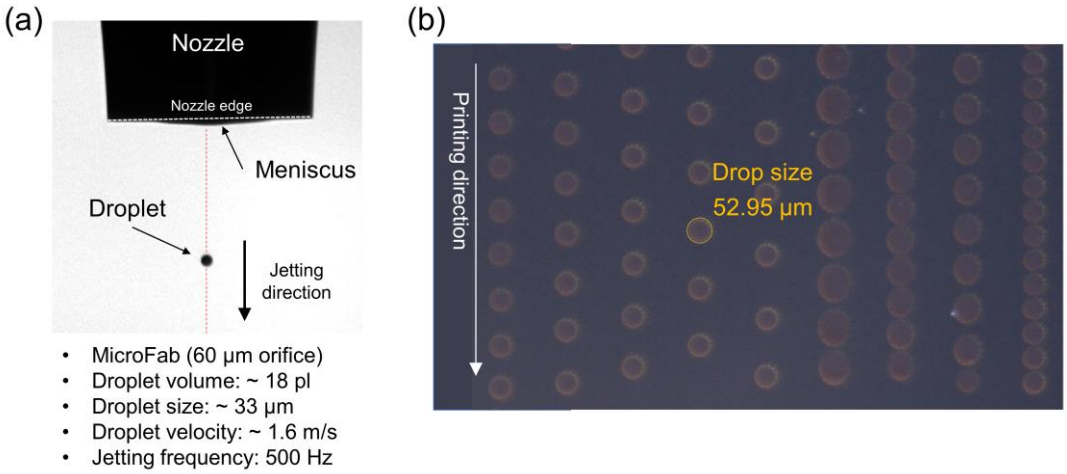

Figure 2.8: (a) Stable ejection of the semiconductor ink from a single ejector printhead in jetting behavior analysis and (b) test printed pattern with different printing space.

process to print semiconductors on channel regions to fabricate TFTs. These stable jetting settings were ideal for reproducing a consistent printed pattern and polymer microstructure.

2.2.3 Inkjet-printed P3HT channel TFT (reference device)

Reference TFT devices using printed P3HT solutions were fabricated for subsequent annealing following the inkjet printing, P3HT is visible on the channel region in Fig. 2.9a. The printed P3HT ink was effectively captured in the S/D pattern and channel region owing to the hydrophobic surface of SiO_2 (White dashed box). The deposited bare gold has a lower contact angle of ~65° compared to the HMDS-treated SiO_2 surface contact angle of 90°, confirming the dielectric surface had the higher surface energy. After printing the polymeric ink, the sample was annealed at 120 °C for 1 hour in a vacuum oven. The annealing temperature influences the crystalline structure of P3HT [92], with higher annealing temperatures contributing to enhanced crystallinity [93]. Experimental assessments were conducted at two specific annealing temperatures, 120 °C and 160 °C. However, it was observed that altering the annealing temperature within this range did not yield any discernible variation in device performance. This outcome implies that further elevating the annealing temperature from 120 °C does not result in additional improvements in crystallinity.

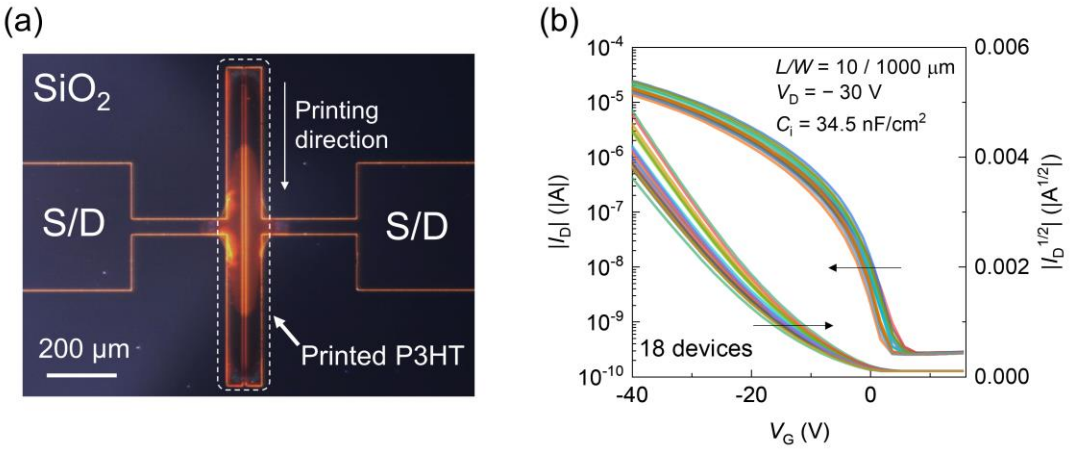

Figure 2.9: (a) Top view of printing P3HT on pre-patterned S/D electrodes and (b) transfer characteristics (I_D *vs.* V_G) of the IJP P3HT TFT

The transfer characteristics of reference devices are shown in Fig. 2.9b (the total number of devices is 18). All devices had good switching behavior, which is consistent with the TFT *I-V* characteristics discussed in Chapter 1.4. The fabrication of the printed TFTs followed these processing parameters to compare the novel ink formulations used to create the hybrid inks.

2.3 Inkjet-printed silver nano particles for electrodes

For printed roll-to-roll processing, vacuum-deposited contacts may be replaced by inkjet-printed metal electrodes. In subsequent studies in this thesis, silver nanoparticle (Ag NP) inks from ANP (DGP 40LT-15C) were used in this work. As presented in Chapter 1.5.2, the silver nanoparticles

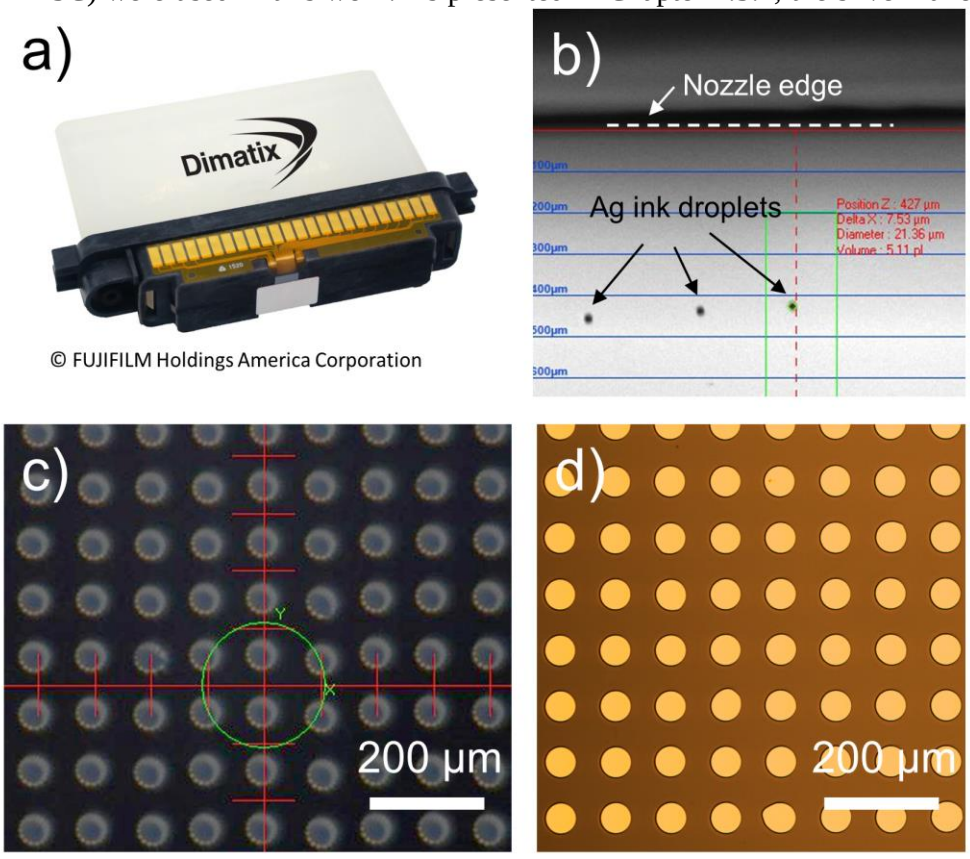

Figure 2.10: **(**a) multi nozzle printer head of the Dimatix cartridge for inkjet printing Ag NPs. (b) Ejection of silver ink droplets from the multi nozzle ejector. (c) Optical micrographs of printed Ag NPs patterned on a Si wafer surface and (d) the same printed pattern after sintering process.

consist of a core-shell structure, when the shell is sintered the core metallic particles merge with neighboring nanoparticles to form a film. Unlike printing semiconductor materials, electrodes are patterned over larger areas, electrically connecting different components. For printing large areas in a short fabrication time, multi-nozzle printheads are more favourable than the single nozzle (such as the MicroFab used for printing organic polymer semiconductors). Moreover, the silver inks can be reserved in a cartridge which is easier to store compared to single ejector printheads. Fig. 2.10a shows the multi-nozzle printer head produced by Dimatix Fuji Film. Single droplets of Ag ink from each nozzle were achieved with stable jetting conditions as shown in Fig. 2.10b. Single droplets of Ag ink have volumes of 5~7 pl, diameters of 21~24 μm and ~3.3 m/s drop velocity using a jetting frequency of 2k Hz. With this condition, printed Ag ink on a bare SiO_2 surface has a droplet diameter of 53 ~ 58 μm, shown in Fig. 2.10c. The printed pattern was annealed at 180 °C by using a hotplate (air ambient) for the sintering process. The sintering temperature was optimized by measuring the electrical resistivity discussed in Chapter 5.2.1. After sintering, the deposited silver forms a film in the pattern shown in Fig. 2.10d.

To develop this process for patterning line features on a surface, the surface energy of the substrate should be considered since it critically affects the shape of the printed pattern. To modify the surface energy of the SiO_2 substrates, HMDS was employed during the fabrication process. The HMDS forms a uniform monolayer on the SiO_2 surface, effectively lowering its surface energy. This effect is beneficial for polymeric semiconductors, as it induces a highly ordered crystalline structure. This hydrophobic surface facilitates the creation of metal electrodes with smaller features. Nevertheless, it is important to acknowledge that controlling the printed pattern under these conditions can be challenging, and certain defects may arise, such as non-continuous printed patterns and bulging sidewall features along the printed lines, causing non-uniformities that

adversely impact the electrical contacts [94-96]. Hence, in this work, a bare SiO_2 surface was used without HMDS treatment for printing the Ag inks. An HMDS treatment was applied following the printing of the metal to functionalize the dielectric surface prior to the printing of the polymeric semiconductor.

In the process of fabricating S/D electrodes for TFTs via inkjet printing, it is essential to obtain a continuous single-line printed pattern initially. The jetting conditions mentioned above made each printed Ag droplet have approximately 55 µm diameter on the SiO_2 surface. To achieve a continuous line pattern, the drop spacing, or the distance between the droplets, should be kept below 55 µm. Figure 2.11 depicts the printed Ag single line with various drop spacing values. When using a drop spacing of 60 µm, the spacing exceeds the diameter of a single droplet (55 µm), resulting in a discontinuous line due to the separation of jetted droplets. With a 50 µm drop spacing, the printed single droplets began to merge, creating a continuous line; however, line edge roughness (LER) was poor. This LER persisted even in cases with drop spacings of 48 µm and 46 µm, although it appeared relatively negligible with the 46 µm drop spacing. In the case of a 44 µm

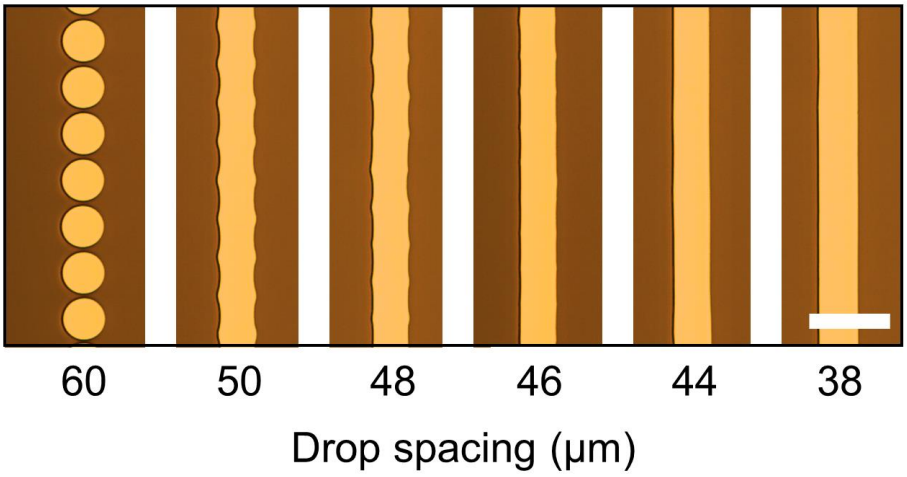

Figure 2.11: Inkjet printed Ag in single lines with different drop spacing from 60 to 38 µm. The line edge roughness diminished from 46 µm of drop spacing. Scale bar is 100 µm.

drop spacing, the LER was reduced, and a flat line edge was achieved, as observed through optical microscopy. Subsequently, decreasing the drop spacing to 38 µm led to a slight increase in linewidth compared to the 44 µm drop spacing due to the higher volume of ink printed within the designated area. Consequently, the optimal smallest feature of the printed Ag thin film without LER was attained at a 44 µm drop spacing under our specific printing conditions.

Using these printing conditions, a 6 × 3 S/D array was successfully printed for the fabrication of TFTs, as shown in Figure 2.12a. Under optical microscopy at high magnifications (Fig. 2.12b), all print patterns were found to have uniform line widths. Specifically, employing the printing conditions as demonstrated in Figure 2.11 with a 44 µm drop spacing, resulted in the achievement of a flat edge without LER for the inkjet-printed Ag S/D electrodes, where the channel length measured 30 µm, and the channel width measured to be 1 mm. The TFT fabrication process with Ag S/D electrodes is discussed in Chapter 5.2.2.

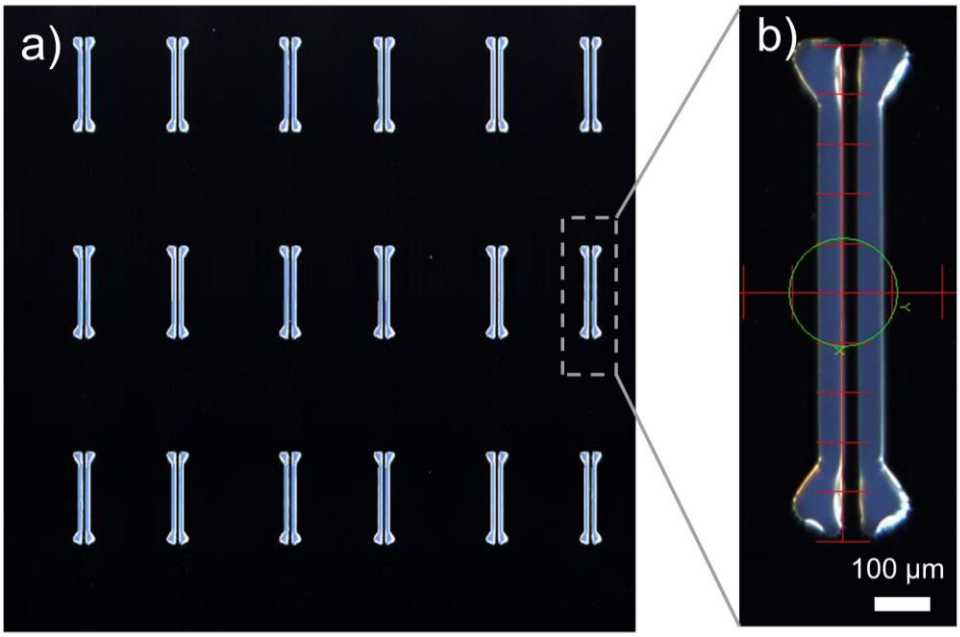

Figure 2.12: (a) As-inkjet-printed Ag S/D 6 x 3 array for TFT applications. (b) Printed S/D pattern having 1 mm width and 30 µm channel length.

Chapter 3
Inkjet-printed nanocomposite channel (P3HT+MoS_2) TFTs

3.1 Introduction

As a first step to study the enhanced performance of inkjet-printed polymer channel TFT by adding MoS_2 nanosheets, P3HT was initially used as a host polymeric semiconductor material. Both semiconductors have been widely used and extensively studied for their materials properties and electronic applications. Moreover, an alkyl-trichlorosilane self-assembled monolayer (DDTS) was used as a surfactant for MoS_2 particles suspended in P3HT solutions to explore how the exfoliation level of MoS_2 nanosheets functions and impacts the charge transport property of P3HT. Optical absorption measurement from the ultraviolet to the visible wavelengths (UV-vis) was carried out to evaluate the effect of the surfactant on the exfoliated MoS_2 nanosheets [87, 97-99]. Optical absorption measurements were used to investigate the effect of the MoS_2 surface functionalization on the suspension concentration and MoS_2 thickness for inkjet-printed hybrid inks used to fabricate TFTs. The printed devices were comprehensively characterized by *I-V* measurements, atomic force microscopy (AFM), UV-vis., and X-ray diffraction (XRD) analysis to determine the influence of the ink formulation, printing process, and thin-film structure on the electrical characteristics and performance parameters of the TFT devices.

3.2 Results and discussions

3.2.1 Effect of MoS_2 surface functionalization on ink formulation

The formulation of the hybrid ink requires well-exfoliated MoS_2 nanosheets suspended in the polymeric matrix, enhancing the electrical interface between the polymeric solution and the MoS_2 suspension while minimizing interfacial and structural defects [100, 101]. Unfortunately,

conventional liquid-phase exfoliation methods, do not yield suspensions having high density or large lateral size with single or few-layer MoS_2 nanosheets [87, 102, 103] compared to films formed by chemical vapor deposition or mechanical exfoliation. Thin layers of MoS_2 will disperse more easily in the solution, preventing agglomeration of the nanosheets. The clustering of the suspended MoS_2 leads to a higher density of interface defects formed by overlapping multilayers of MoS_2. To overcome this challenge, alkyl-trichlorosilane was added to the DCB solvent to functionalize the surface of MoS_2 during the sonication process to create a more uniform dispersion of the suspended flakes and enhancing the exfoliation process for creating few-layer MoS_2 structures [71].

To determine the effect of the surface functionalization, two suspensions (MoS_2 in DCB) were made, with and without the DDTS additive. The suspensions were found to be visually similar in terms of optical transparency when the inks were first formulated (Fig. 2.2) but samples without the surface treatment were found to settle out of the suspension as shown by the increased optical transparency of the ink after 48 hours. For UV-vis spectral analysis, both suspensions were diluted with 1 mg/ml to 0.1 or 0.05 mg/ml which are shown in the inset of Fig. 3.1. The suspension with DDTS showed a uniform pale yellowish-green color, that remained visually unchanged over several days suggesting a stable suspension. In contrast, the exfoliated MoS_2 nanosheets without the DDTS treatment have a different color (grey) of suspension suggesting it may be different in terms of its size, layer thickness, and distribution in the solvent [98].

To determine the cause of the observed differences in the suspension, the structural properties and the effect of the DDTS functionalization on the suspended nanosheets were characterized by optical absorption using UV-vis spectroscopy. The optical absorption of the suspended MoS_2 in DCB was compared for two separate formulations of the suspension. Fig.

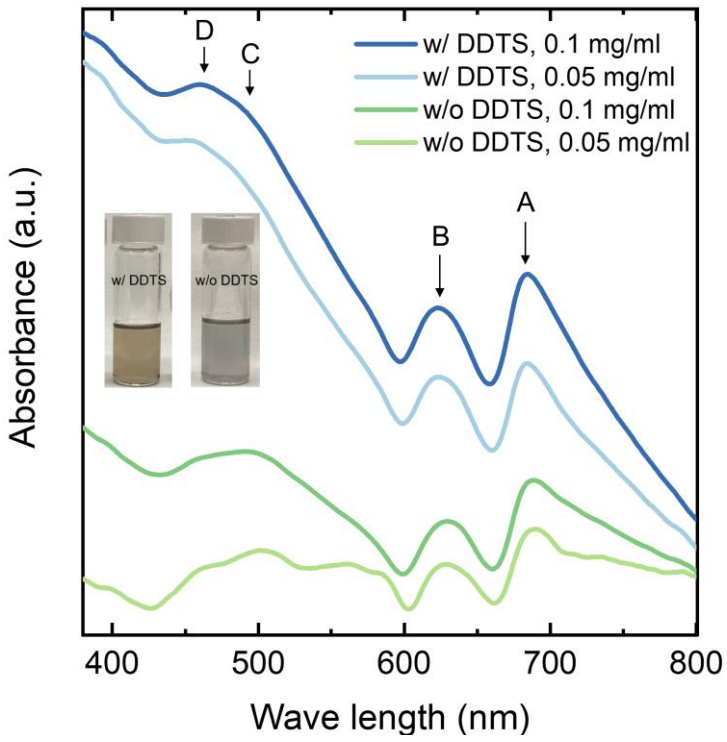

Figure 3.1: Normalized UV-vis absorption spectra of two MoS_2 suspensions with (blue) or without (green) DDTS. Inset shows the photograph of prepared MoS_2 suspension with (left) and without (right) DDTS.

3.1 shows the measured optical absorption for MoS_2 suspended in DCB, with and without the DDTS treatment. The A and B absorption peaks, at 625 and 700 nm, respectively, originate from excitonic peaks of few-layer nanosheets and represent the 2H phase of the MoS_2 [69, 87, 97, 98]. The C and D peaks, at 500 and 460 nm, respectively, are related to the thickness of the MoS_2 structures where bulk MoS_2 has an indirect bandgap and monolayer structures have a wider direct bandgap [87, 104]. The absorption was found to increase for the DDTS-treated suspension indicating an increase in a few layers of MoS_2 nanosheets. The C peak absorption at 500 nm also showed a slight blue shift for the DDTS-treated flakes further showing an

increase in bandgap energy of the MoS_2 due to an increase in the creation of few-layer structures from the exfoliation process [87, 99].

Furthermore, the ratio between the C-D peaks and A-B peaks of the MoS_2 suspension without DDTS was higher at 0.1 mg/ml than at 0.05 mg/ml indicating an increasing density of few-layer MoS_2 nanosheets in the higher MoS_2 concentration suspensions. These observations support the increasing density of few-layer MoS_2 in a suspension may be accomplished through functionalization of the MoS_2 surface by the DDTS treatment.

The MoS_2 suspensions were then mixed into the P3HT solutions to create the hybrid nanocomposite. This mixture was then inkjet-printed onto patterned thermal SiO_2 on highly doped Si wafers to create bottom common-gate/bottom electrode TFT structures. The electrical characteristics and structural properties of the printed TFTs were then investigated.

3.2.2 Inkjet-printed hybrid nanocomposite inks for TFT fabrication

Inks with and without the MoS_2 surface functionalization were used to print TFTs to further determine the effect of the hybrid ink formulation on device performance. Printed TFTs from the nanocomposite P3HT/MoS_2 ink were characterized with MoS_2 concentrations from 0.25 wt% to 2 wt%. Generally, a transparent orange color tint of the P3HT solution, showing a fully dissolved (amorphous state) P3HT solution [105, 106] darkened with increasing concentrations of suspended MoS_2 (inset of Fig. 3.2a).

The saturation field-effect mobility of the inkjet-printed TFTs was extracted as a function of the MoS_2 concentration in printed hybrid nanocomposite inks (Fig. 3.2a). To obtain a reliable and comparable reference point, a total 18 baseline devices were characterized shown in Fig. 3.2. Reference devices were fabricated using jet-printed P3HT-only inks. The average extracted field-

effect mobility of the reference devices was ~0.011 $cm^2/V{\cdot}s$. For inks containing MoS_2 suspensions in the P3HT, the printed devices the extracted field-effect mobility increased with increasing MoS_2

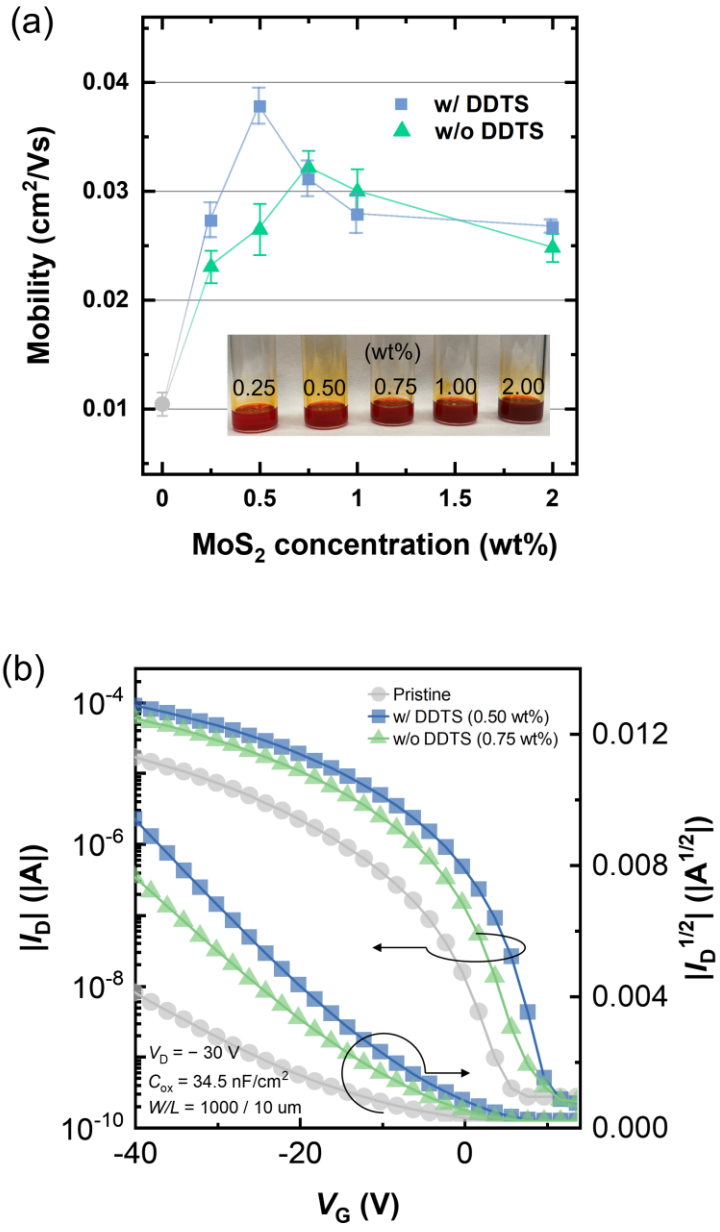

Figure 3.2: Summary of electrical characteristics of all device performance such as (a) mobility changes as a function of MoS_2 concentrations, (b) transfer characteristics of three devices pristine P3HT film transistor and hybrid channel TFT w/ or w/o DDTS.

concentration, with a maximum μ_{sat} ~ 0.038 $cm^2/V \cdot s$ (at 0.5 wt%) and 0.032 $cm^2/V \cdot s$ (at 0.75 wt%) for the nanosheets treated with and without DDTS, respectively. Together with the favorable band offset for hole transport between the P3HT and MoS_2, the carrier mobility values are higher for the inks with the suspension due to the network of electrically connected single crystalline regions within the disordered P3HT film [107, 108].

The effect of the surface functionalized on the electrical behavior of the printed TFTs is shown in the *I-V* transfer characteristics (I_D vs. V_G) for both hybrid nanocomposite and baseline TFTs (Fig. 3.2b). All devices demonstrated well-defined switching behavior with an on/off current ratio of ~10^5 and subthreshold swing of ~ 3 V/decade with the nanocomposite TFTs having higher on-current levels (regardless of any DDTS surface functionalization) compared to baseline TFTs. The electrical characteristics of all fabricated devices are summarized in Table 1. For the DDTS functionalized MoS_2, the highest extracted field-effect mobility was measured at 0.5 wt% MoS_2

Table 1. Electrical properties for all Inkjet-printed TFTs with P3HT (reference), P3HT + MoS_2 w/ or w/o DDTS channel.

Semiconductor	MoS_2 (wt%)	μ_{sat} (cm^2/Vs)	V_{th} (V)	ON/OFF ratio ($\times 10^5$)
P3HT	0	0.0105 ± 0.0015	− 9.44 ± 0.89	0.79 ± 0.15
P3HT + MoS_2 w/o DDTS	0.25	0.0231 ± 0.0014	− 6.61 ± 0.46	1.87 ± 0.44
	0.50	0.0265 ± 0.0023	− 5.37 ± 0.79	2.64 ± 0.41
	0.75	0.0322 ± 0.0014	− 4.95 ± 1.06	3.68 ± 0.52
	1.00	0.0300 ± 0.0019	− 4.24 ± 0.83	2.64 ± 0.48
	2.00	0.0248 ± 0.0012	− 4.07 ± 0.69	1.82 ± 0.15
P3HT + MoS_2 w/ DDTS	0.25	0.0273 ± 0.0016	− 4.21 ± 0.53	4.69 ± 0.13
	0.50	0.0378 ± 0.0016	− 3.62 ± 0.34	4.77 ± 0.60
	0.75	0.0311 ± 0.0016	− 1.88 ± 0.50	1.70 ± 0.17
	1.00	0.0279 ± 0.0017	− 1.31 ± 0.49	1.53 ± 0.33
	2.00	0.0267 ± 0.0007	− 0.50 ± 0.29	1.06 ± 0.22

concentration, while the devices without DDTS had a maximum value at a concentration of 0.75 wt%. Referring to the UV-vis spectra (Fig. 3.1), the DDTS functionalized MoS_2 nanocomposite inks were found to have a higher density of few-layer MoS_2 nanosheets after sonication, shown by the higher C-D peaks and the increase in the ratio between the C-D to A-B peaks in the UV-vis spectrum. This result supports the hypothesis that a more effective exfoliation process to create the nanosheets is enabled by the DDTS surface treatment compared to suspensions created without the surfactant.

The threshold voltages (V_{TH}) were extracted from the linear extrapolation of the $\sqrt{I_D}$ vs. V_G plots. In Fig. 3.3b, the pristine P3HT-only ink formulation has a typical V_{TH} of − 9.4 V while the V_{TH} of the TFTs fabricated from the hybrid nanocomposite inks had more positively shifted threshold voltages [109-111]. The V_{TH} shift may be due to trapped charges at the interface formed along the MoS_2 nanosheets within P3HT films as bulk trap states [112]. The increased concentration of MoS_2 nanosheets may increase this trap density within the nanocomposite films. To further understand the effect of the trap density on the TFT electrical stability, constant dc gate-bias stress tests were conducted to assess the effect of trap density for devices created with different ink formulations. Fig. 3.3c shows the current change as a function of time for samples processed using the different ink formulations. The normalized $|I_{DS}|$ vs. time measurements, for TFTs operating under $V_G = -40$ V and $V_D = -10$ V, show the electrical stability as the MoS_2 concentration for different ink formulations. The normalized current was observed to decrease between 33% for P3HT-only films to 70% for the highest concentration of MoS_2 (treated with DDTS suspended) in P3HT. Comparing devices fabricated with inks having 2 wt% MoS_2 in P3HT, the current decay was observed to be higher for ink formulations having the surfactant treatment (blue diamonds, in Fig. 3.3c) compared to suspensions without (green reverse triangles). The results further support the effect of the

surfactant to effectively separate layers of MoS_2, increasing its density in the suspension. This increasing nanosheet density raises the interface density for charge trapping that may be responsible for the observed V_{TH} shift in the TFT electrical characteristics. The inclusion of the suspension has improved the transport properties for the printed TFTs but at the expense of the electrical stability of the devices. Continuing investigations are being made to determine this

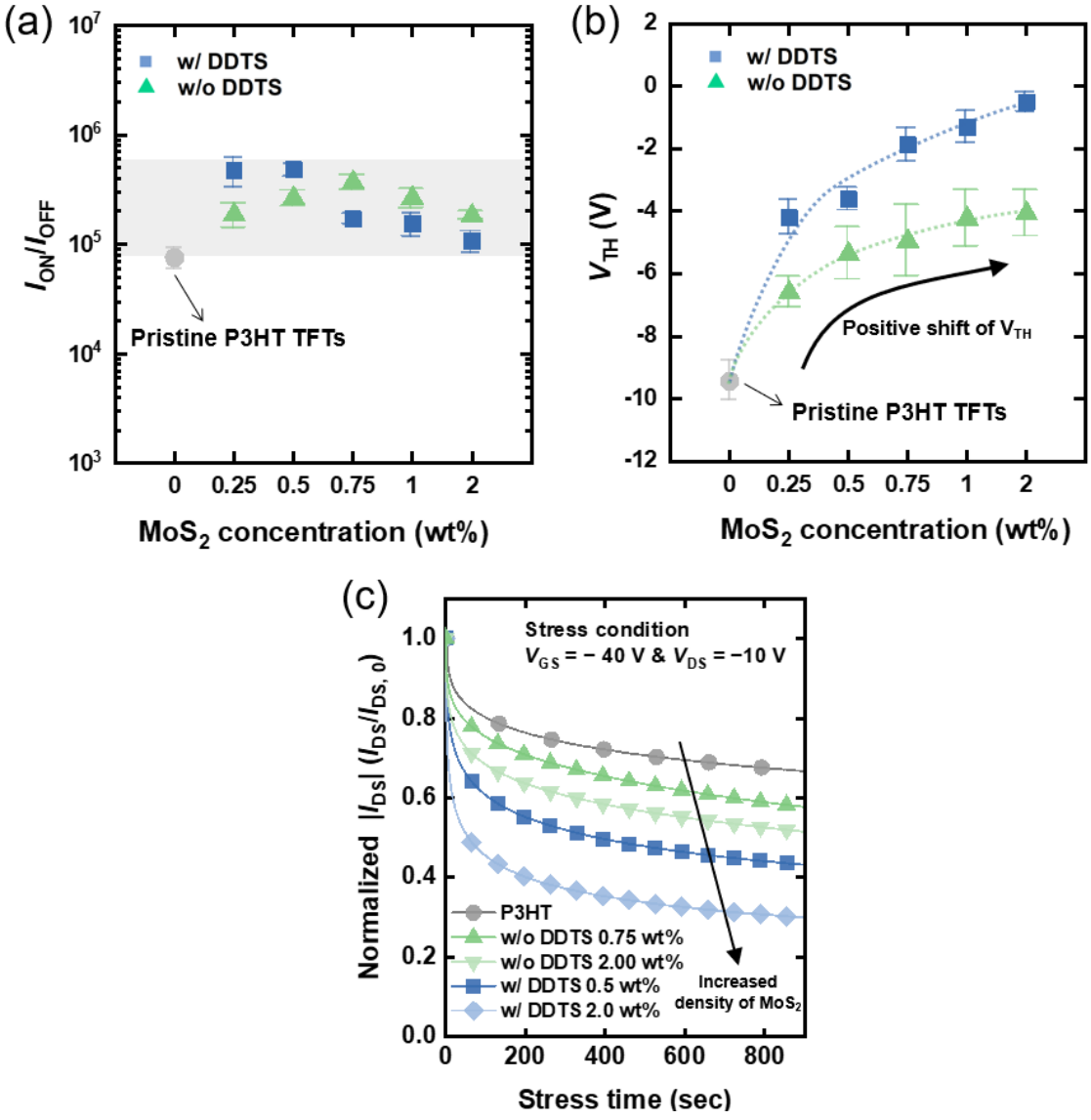

Figure 3.3: Summary of electrical characteristics, (a) on/off ratio and (b) threshold voltage (V_{TH}), of all devices as a function of MoS_2 concentrations, and (c) DC bias stress result of different devices.

interface effect for different polymeric semiconductors. The accumulation layer of the printed TFT is also relatively thin and the observed changes in the device parameters may not be only due to transport between the MoS_2 and the P3HT. Evidence for a structural dependence on the MoS_2 concentration was observed by increasing the MoS_2 concentration up to 2 wt%, resulting in decreasing field-effect mobility to a value of ~0.026 $cm^2/V{\cdot}s$ for both DDTS treated and nontreated suspensions.

The possibility of the MoS_2 acting as a dopant in the P3HT could affect the transport properties of the semiconductor as a function of the MoS_2 concentration. Considering the higher intrinsic carrier concentration of MoS_2 compared to P3HT ($n_i \sim 10^{18}$ cm^{-3} to 2.5×10^{18} cm^{-3} [113]) and P3HT with $n_i \sim 10^3$~10^5 cm^{-3}) the conductivity of P3HT thin film may increase with increasing MoS_2 suspension. The n_i of P3HT was approximately estimated by using the equation $n_i^2 = N_c N_v\, e^{-Eg/kT}$, where N_c and N_v are the effective density of states, E_g denotes band gap, k is Boltzmann constant, and T is temperature. However, it is important to note that as the concentration of MoS_2 increased from 0.5 wt% to 2 wt%, there was a decrease in carrier mobility. Additionally, the off-state current leakage remained at a consistent level despite the increase in MoS_2 concentration, suggesting the associated enhancement in bulk conductivity did not change. This outcome is substantiated by the corresponding demonstration of a similar on/off ratio, as depicted in Fig. 3.3a. Consequently, the charge transport characteristics of the hybrid film may be dependent on a separate property of the film. This possibility was investigated for the structural quality of the P3HT, given the doping effects are negligible and the relatively large energy barrier for charge injection of charge at the interface of the MoS_2-P3HT interface of 200meV due to their band offset. The mobility degradation due to a structural degradation of the P3HT with higher MoS_2 concentration will be discussed and analyzed with more detail in Chapter 4.

3.2.3 Study of the microstructure and the electrical characteristics of hybrid thin film

As shown in Fig. 3.2a, further increases in the MoS_2 concentration were observed to degrade the saturation field-effect mobility exposing an upper limit to the concentration of MoS_2 suspension in the hybrid nanocomposite inks. As the concentration of MoS_2 nanoparticles in the polymeric semiconductor solution increases, interfaces between the organic/inorganic materials increase, imposing a structural influence on the formation of the polymeric thin film in addition to the electrical changes measured in the *I-V* characteristics. The introduced MoS_2 nanosheets act as surfaces for the P3HT to crystallize during film formation. This influence may affect the long-range ordering of the polythiophene film formation where structural nanofibers have been observed for high-quality materials [105, 114-116]. As the concentration of the MoS_2 increases, the higher density of nucleation sites disrupts the long-range ordering through the film, resulting in the introduction of interface defects between the MoS_2 and P3HT that degrades the structural quality of the P3HT thin film. While the MoS_2 network is intended to improve the electrical and structural characteristics of the P3HT device, high concentrations of MoS_2 in the nanocomposite inhibit the crystalline formation of the P3HT resulting in the degradation of the carrier transport properties.

To determine if the structural properties of the film are affected by the MoS_2 concentration, atomic-force microscopy (AFM) was performed to characterize the surface morphology of the films. In Fig. 3.4, the surface morphology of pristine P3HT and hybrid film with 0.5 wt% MoS_2 (with DDTS functionalization) was characterized by AFM. Fig. 3.4b shows that the formation of nanofiber-like aggregates was observed in the 0.5 wt% MoS_2 on the P3HT surface, suggesting an enhancement of the structural quality of the polymeric thin-film matrix. These devices had the highest extracted

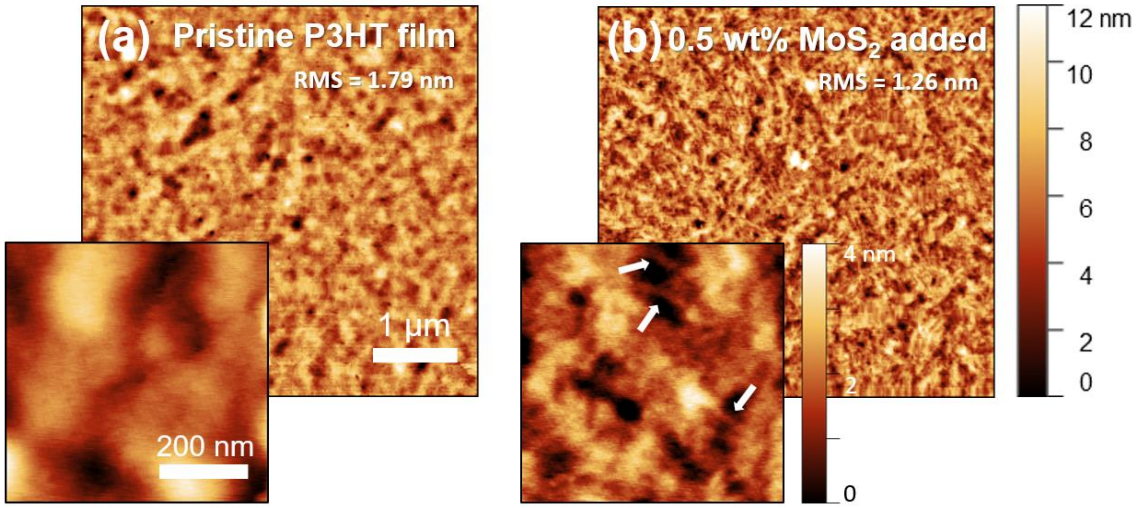

Figure 3.4: AFM height images of pristine (a) P3HT film and (b) the hybrid film which has 0.5 wt% of MoS_2 concentration. Inset shows the higher resolution of same AFM scan. The nanofiber-like structures were observed in the 0.5 wt% MoS_2 (highlighted by the white arrows).

field-effect mobility. This observation suggests a structural change may be responsible for the changes in the transport properties.

The degree of crystallinity was characterized further between pristine P3HT films and hybrid nanocomposite films by UV-vis spectroscopy, shown in Fig. 3.5. In the result of UV-vis absorption for the pristine P3HT film, 0-0 ($\lambda \sim 600$ nm), 0-1 ($\lambda \sim 550$ nm), and 0-2 ($\lambda \sim 520$ nm) peaks are clearly observed showing a well-ordered P3HT-based film [117-120]. The absorption spectra of three films having different MoS_2 concentrations are normalized at the 0-2 transition to compare

Table 2. UV-vis results for comparison.

Semiconductor	Exciton bandwidth, W_{ex} [meV]
P3HT	110.5
Hybrid 0.5 wt%	92.0
Hybrid 2.0 wt%	94.9

the peaks related to the crystallinity of the film (0-0 and 0-1) [119, 120]. The two peaks of the

hybrid film have a higher intensity compared to pristine P3HT films, indicating larger crystalline polymer domains in the thin film [118-120]. This degree of crystallinity can be quantified and determined by estimating the exciton bandwidth (W_{ex}) with the following equation [117, 118]:

$$\frac{A_{0-0}}{A_{0-1}} = \left[\frac{1-\left(\frac{0.24\,W_{ex}}{E_p}\right)}{1+\left(\frac{0.073\,W_{ex}}{E_p}\right)}\right]^2 \tag{3.1}$$

where $A_{0\text{-}0}$ and $A_{0\text{-}1}$ are peak intensities of 0-0 and 0-1 vibrational transitions. The main intramolecular vibration peak (E_P) of P3HT is at 0.18 eV [116-118]. Table 2 shows the extracted exciton bandwidth, W_{ex}, decreasing with 0.5 wt% MoS_2 concentration which indicates an increase in the crystalline order of the thin film [121]. A slight increase in W_{ex} is extracted for 2 wt% MoS_2 samples suggesting a lowering in the structural quality as the MoS_2 concentration increases.

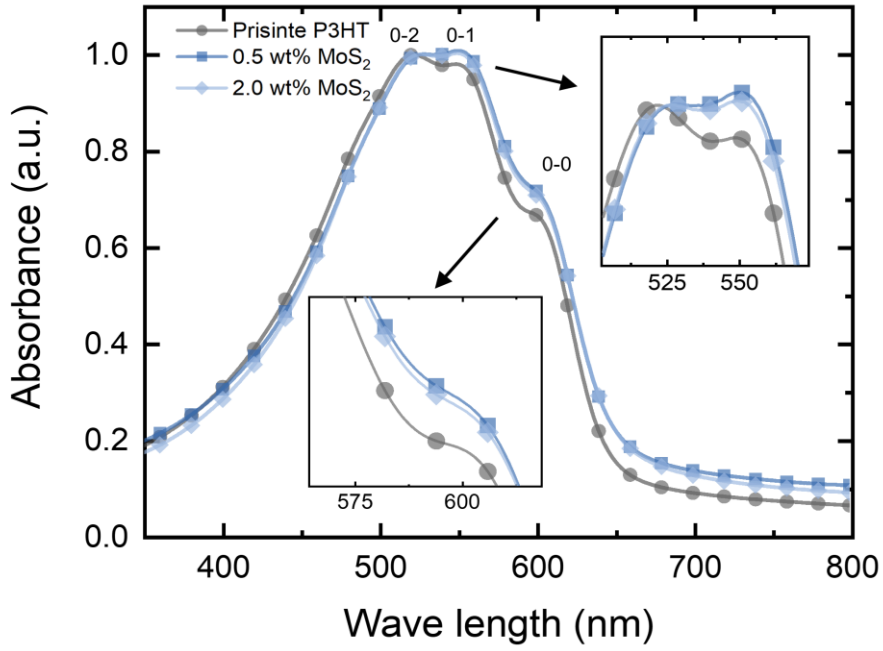

Figure 3.5: UV-vis spectroscopy results of pristine P3HT and hybrid (0.5 or 2 wt% MoS_2 with DDTS) thin films on glass substrate.

To confirm the UV-vis observations, XRD measurements were conducted to further evaluate the degree of crystallinity of the hybrid nanocomposite films [122-124]. Fig. 3.6 shows the out-of-plane and in-plane reflections of the polymeric thin film, respectively. The inset of Fig. 3.6 shows the orientations of the thin-film microstructure for the alkyl chain lamellar stacking, π-π interchain stacking, and π-conjugation in the polymeric film that are represented by the (100), (010), and (001) reflections, respectively [124, 125].

For the out-of-plane reflections, the (100), (200), and (300) peak intensities of the printed films were found to be higher in the hybrid nanocomposite films compared to a pristine P3HT film. The (100) reflection at an angle $2\theta = 5.5°$ was found to be strongest for the 0.5 wt% MoS_2 indicating this concentration resulted in a highly ordered alkyl side chain in the P3HT structure [122, 126]. The (200) and (300) peaks (at $2\theta = 10.8°$ and 16.3°, respectively) are observed in the inset of Fig.

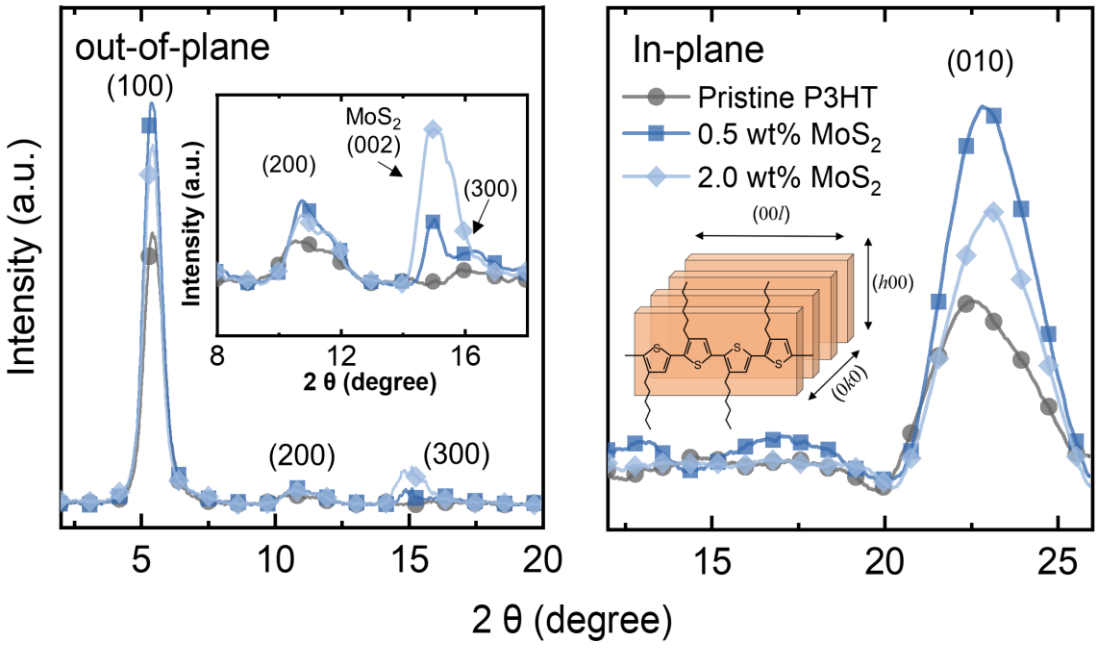

Figure 3.6: Out-of-plane (left) and in-pane (right) XRD pattern of pristine P3HT and hybrid (0.5 or 2 wt% MoS_2 with DDTS) thin films on silicon wafer.

3.6, but the (300) diffraction peak is not clearly defined as this peak overlaps with the MoS_2 (002) reflection $2\theta \approx 15°$ [127, 128]. This (002) MoS_2 peak was only observed in the hybrid thin film made with higher concentrations of MoS_2 suspension (from 0.5 wt% to 2.0 wt%). The in-plane XRD spectroscopy also shows the 0.5 wt% MoS_2 hybrid film had the highest (010) peak intensity due to the stronger π-π interactions in the hybrid films compared to P3HT alone [124]. The XRD measurements support the UV-vis results, showing the highest quality films were obtained with a 0.5 wt% MoS_2 concentration in P3HT, correlating to the highest extracted field-effect carrier mobilities in the TFT devices. As the concentration of the MoS_2 increases, the P3HT structural properties were found to degrade and this degradation was correlated to the reduction in the extracted TFT field-effect mobility.

The observations from the AFM, UV-vis absorption, and XRD data suggest the added MoS_2 suspension to the polymer matrix increases the structural quality due to the formation of nanofiber-like aggregates responsible for enhancing the transport properties of the TFTs. The MoS_2 creates nucleation sites for the nanofiber-like aggregates to form a more ordered film shown in the absorption and XRD characterization. Further studies are continuing to determine how this dependence affects different solution-processed semiconductors to determine the trade-offs for structural and electrical enhancements achievable using these hybrid nanocomposites.

3.3 Conclusions

Few-layer MoS_2 nanosheets were incorporated as a suspension into polythiophene-based electronic inks. The hybrid nanocomposite inks were inkjet-printed for the fabrication of TFT devices. The ink formulation was accomplished using an exfoliation process with MoS_2 suspended in a solvent solution containing a surfactant. The exfoliation of the MoS_2 layers was accomplished

by sonicating a mixture of DDTS in a DCB solution to create a suspension of the MoS_2 nanosheets. UV-vis spectroscopy showed that adding the surfactant increases the creation of few-layer MoS_2 nanosheets, resulting in improved electrical and structural properties of the inkjet-printed P3HT channel TFTs. The printed TFTs from inks formulated with DDTS showed the highest field-effect mobility compared to formulations without surfactant. The TFT performance was also found to be dependent on the concentration of MoS_2 nanosheets within the nanocomposite ink. The field-effect mobility was observed to increase by as much as 3× with increasing MoS_2 concentration. This effect was found to decrease for TFTs having MoS_2 concentrations > 0.5 wt% in P3HT. The dependence of the TFT performance on higher concentrations of MoS_2 additives may be attributed to a degradation in the P3HT structural quality, as shown by XRD. Further discussion on this performance degradation is introduced in the following chapter.

Chapter 4
Inkjet-printed ambipolar nanocomposite channel (DPPT-TT + MoS_2) TFTs

4.1 Introduction

In the previous chapter, hybrid nanocomposite ink using P3HT as the host material was investigated. Then it was found that solution-processible MoS_2 nanosheets could enhance device performance. The ideal ratio of MoS_2 to P3HT was found and the optimal conditions for MoS_2 nanosheets (used surfactant) to allow P3HT to crystallize more effectively. Given this knowledge and the results based on P3HT, it would be fascinating to apply the MoS_2-based nanocomposite semiconductor to the second-generation conjugated polymer semiconductor, also known as the donor-acceptor copolymer (DA copolymer) or ambipolar polymer, beyond the P3HT. Recently, for the active layer material for OTFT, DA copolymer semiconductors have attracted increasing attention as a high-performance polymeric semiconductor, producing devices having field-effect mobilities up to 10 cm^2/Vs in TFTs with ambipolarity [52]. However, this performance is significantly reduced when processed using inkjet-printing methods compared to the conventional spin-coating approach [129]. In the former, the inkjet-printing method does not easily result in the formation of highly ordered crystalline structures due to the static nature of the drying process during film formation. Therefore, a combination of a 2D material suspension (MoS_2) in the polymeric thin film may be created through formulating composite inks that are deposited and patterned using additive processes to enhance the charge transport within this polymer.

Here, the structural and electrical enhancements of inkjet-printed TFTs were demonstrated using a nanocomposite electronics ink comprising of MoS_2 suspended within DPPT-TT. The effect of introducing MoS_2 nanoparticles in the DA copolymer thin film was investigated by extracting the

electrical parameters of fabricated devices and correlating the carrier transport properties of both holes and electrons to the structural changes within the thin-films formed from the composite inks. By optimizing the appropriate concentration of MoS_2 nanoparticles into the ink polymer the electrical properties of the devices were correlated to the molecular structure of the polymer. The structural characteristics of hybrid nanocomposite thin film characterization were studied by employing AFM, ultraviolet–visible-near infrared spectroscopy (UV-vis-NIR), and XRD. The structural qualities were compared to the electrical behavior of the TFT devices to evaluate the effect of MoS_2 on the formation of the thin-film and the extracted device parameters.

4.2 Results and discussions

4.2.1 Inkjet-printed ambipolar polymeric semiconductor TFTs

The inkjet printing process for the TFT fabrication is schematically illustrated in Fig. 4.1. The inset shows an optical micrograph of the as-printed device structure. The high-contrast regions are the source and drain electrodes that border the channel region showing well-aligned printed

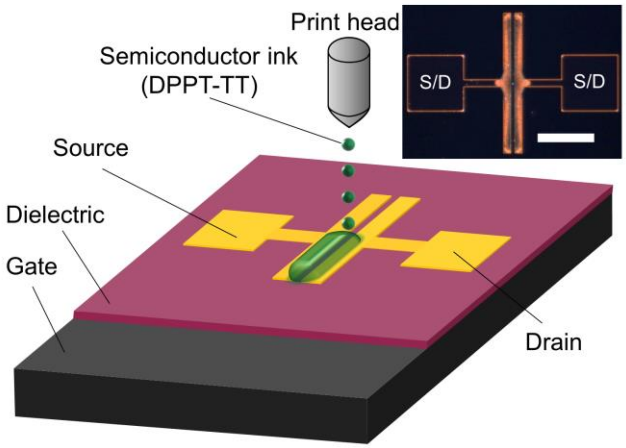

Figure 4.1: Schematic structure of the inkjet-printed DA copolymer channel TFTs. Inset optical microscope top view of a fabricated TFT.

patterns. For comparison, the reference devices using pristine solutions and hybrid channel TFTs (inks containing the nanosheet suspensions) were all prepared and processed in the same fashion. Once the pristine DPPT-TT and suspension containing DPPT-TT inks are printed, their electrical characteristics are evaluated and compared to reference devices.

With these printed devices, the *I*-*V* measurements were conducted in a vacuum, under dark conditions. The transfer characteristics of the reference devices are shown in Fig. 4.2, having well-behaved switching characteristics with a current on/off ratio > 10^5. Ambipolar behavior was also observed under different bias conditions. In both hole and electron transport, when $|V_D|$ increased from 10 to 40 V at the low V_G regime, the off-current level was observed to be high, decreasing the current on/off ratio of the transistor. This observation is due to the ambipolar characteristics of the semiconductor [130]. With low V_G and high V_D conditions, the applied potential bias induces carriers to accumulate at the channel layer that led to increased off-currents that are dependent on

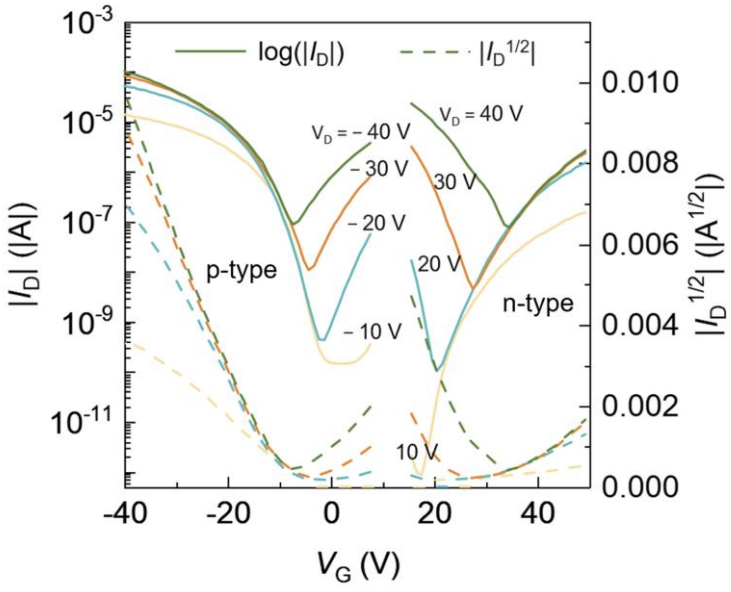

Figure 4.2: Transfer characteristics of inkjet-printed pristine DPPT-TT channel TFTs as a reference device showing ambipolar characteristics.

V_D. However, for lower | V_D | (<10 V), the devices show a clear off-state level (~10^{-9} A and 10^{-12} A for p-type and n-type, respectively). The threshold voltages were extracted to be – 8 V ($V_{TH, h}$) for p-channel operation, and 36 V ($V_{TH, e}$) for n-channel operation. The electrical parameters at saturation for the hole mobility are ~0.066 $cm^2/V{\cdot}s$ and ~0.005 $cm^2/V{\cdot}s$ for the electron mobility. These results will be compared to the hybrid channel TFTs in the following section.

4.2.2 Effect of MoS_2 suspension on TFT characteristics

In Fig. 4.3, the prepared inks for pristine (left vial) and hybrid (right vial with 0.5 wt% MoS_2 suspension) DPPT-TT inks mixed in DCB are shown. Following dilution, both mixtures appear to be visually similar having a pale-green color (see Fig. 4.3a). However, after 30 min of ultra-sonication, the color of the hybrid mixture became visually darker (Fig. 4.3b). The observation may be due to pre-aggregation [131, 132] of the polymer induced by the MoS_2 flakes or a change in the optical absorption of the solutions due to the suspended MoS_2 flakes in the mixture [87].

To further understand how this change affected the mixture, inkjet-printed DPPT-TT based TFTs were fabricated and characterized. Fig. 4.4 shows the output characteristics of the hybrid channel

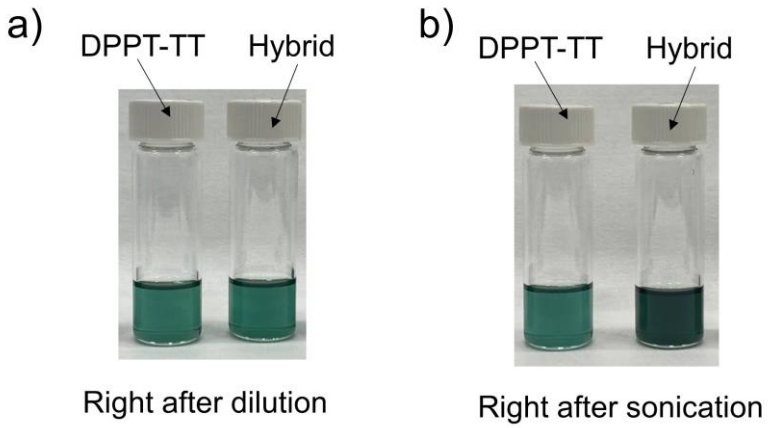

Figure 4.3: Photography of prepared DPPT-TT and hybrid ink in glass vial at (a) right after dilution and (b) ultra-sonication.

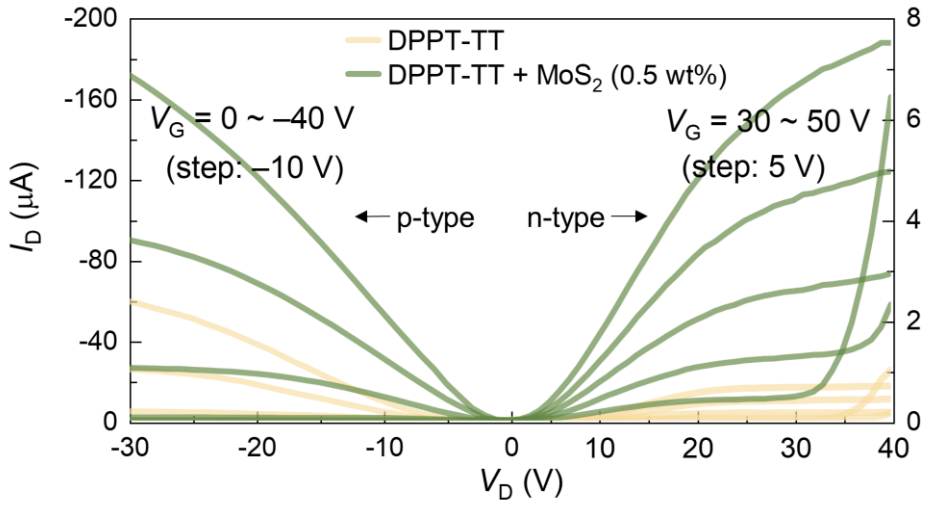

Figure 4.4: Output characteristics of the inkjet-printed pristine DPPT-TT and hybrid (w/ 0.5 wt% MoS_2) channel TFTs.

TFTs and reference devices, consisting of pristine DPPT-TT inks used for the TFT fabrication. The output characteristics showed improvement in both electron and hole transport for the hybrid ink devices compared to the reference TFTs. The TFTs from the hybrid inks have higher drain

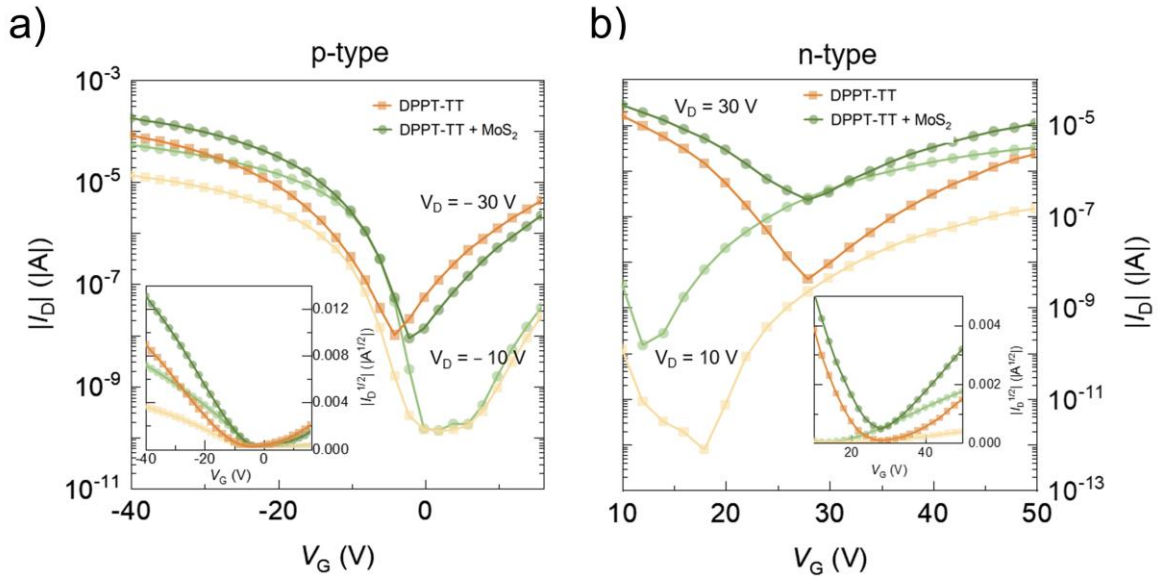

Figure 4.5: Transfer characteristics (log) of pristine DPPT-TT and hybrid (w/ 0.5 wt%) channel TFTs in (a) p-type and (b) n-type transport. Inset shows the transfer characteristics (linear) plotted as the square root of $|I_D|$ versus V_G.

currents (I_D) at the same bias conditions compared to the reference device. For the n-channel operation (electron transport, right side of Fig. 4.4), the gate voltage (V_G) was swept from 30 to 50 V; at V_G < 30V, hole conductivity dominated the *I-V* characteristics and is not plotted for the n-channel devices [133]. Fig. 4.5a and b show the transfer characteristics of two different devices. In both p- and n-channel operation, the hybrid channel devices showed improved drain current levels in both the linear (V_D = ±10 V) and saturation regime (V_D = ±30 V).

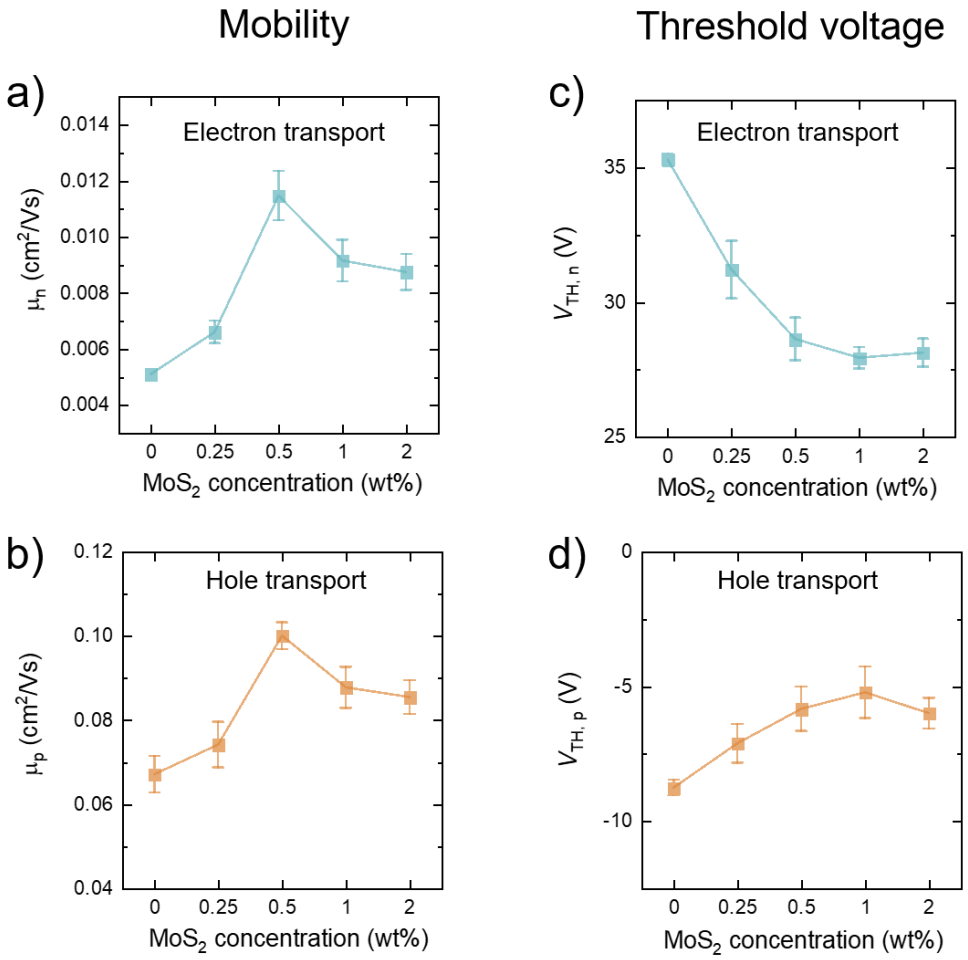

Figure 4.6: (a) Electron and (b) hole mobility changes as a function of MoS_2 concentrations. Threshold voltage changes in (c) electron and (d) hole transport which dependent on MoS_2 concentrations.

To investigate the effect of the MoS_2 nanosheet suspension within this polymeric semiconductor, the concentration of MoS_2 was varied between 0.25, 0.5, 1.0, and 2.0 wt%. The calculated field-effect mobility and V_{TH} of the fabricated TFTs are summarized in Fig. 4.6. The mobility changes over different MoS_2 concentrations were similar in both p- (Fig. 4.6b) and n- (Fig. 4.6a) channel devices. The increased mobility was observed for a suspension concentration starting at 0.25 wt% MoS_2 compared to the reference devices with no additives. Hybrid channel devices with 0.5 wt% MoS_2 suspensions showed the highest carrier mobility, but the mobility decreased with further increasing MoS_2 concentrations for values of 1.0 and 2.0 wt%. This observation may be caused by a structural change in the thin film layer as the ink dries [134, 135]. The crystalline structure of the thin-film has been observed to change with increasing MoS_2 concentration in polythiophene inks, leading to degraded electrical performance. While a decreasing mobility with higher MoS_2 concentration was observed, the carrier transport was still better than the reference device. This behavior suggests the added MoS_2 nanosheet still played a role in improving the charge transport properties through the polymer and the single-crystal MoS_2 layers. On the other hand, the suspension may also cause a degradation in the structural quality of the DA copolymer. To further understand this observation, consideration of the microstructure of the polymer thin film was investigated and discussed in the following section with additional detail.

The extracted threshold voltage varied as a function of MoS_2 concentrations in both n- and p-channel transport which are shown in Figs. 4.6c and 4.6d respectively. For the n-type reference device, V_{TH} ~ 35.3 V shifts towards the negative bias direction with increasing MoS_2 suspension

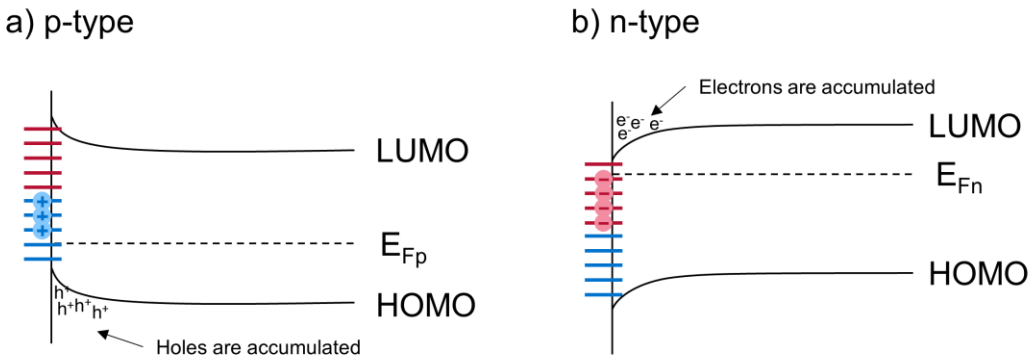

Figure 4.7: Energy band diagram at interface between oxide and semiconductor in (a) p-type and (b) n-type transport.

concentrations. The largest ΔV_{TH} = 7 V occurred after adding 1 wt% MoS_2 with V_{TH} ~ 27.9 V. For the p-channel reference device, V_{TH} ~ − 8.8 V and shifts to − 5.2 V after adding 1 wt% MoS_2. This V_{TH} shift in the positive bias direction has been observed in p-type polymeric semiconductors with additives [111, 136-138]. The direction of the V_{TH} shift can be understood by considering interfacial trap states and the applied gate bias. In p-type or n-type transport, V_{TH} can be shifted by the additional charges of a donor-like (positive charges) or acceptor-like (negative charges) interface trap states, respectively, increasing the trapped charge in the polymeric thin film [139]. In Fig. 4.7, the E_{Fp} or E_{Fn} refers to the Fermi energy level for p- and n-type semiconductors, respectively. The energy states between midgap and E_{Fn} are shown as red lines and the energy states between E_{Fp} and midgap are shown as blue lines that depict acceptor-like trap states and donor-like trap states, respectively. Thus, when V_G is applied to the devices, E_{Fp} or E_{Fn} shifts downward or upward relative to the band bending at the semiconductor surface. In this case, empty donor traps have a positive charge and occupied acceptor-like trap states have a negative charge that can alter the threshold voltage. Since MoS_2 added hybrid channel layer has more interface trap states than that of pristine DPPT-TT, and the observed threshold voltage shift is positive in p-type

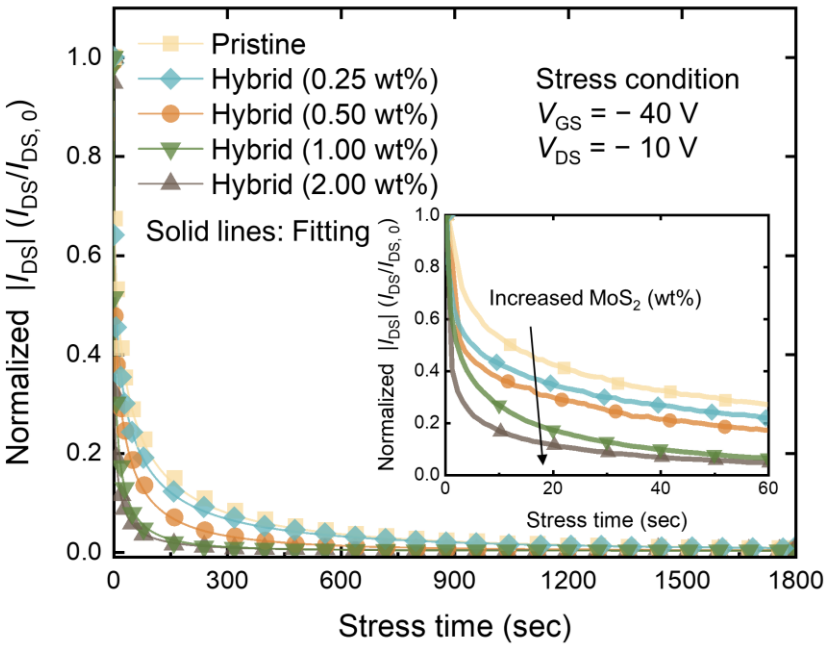

Figure 4.8: Normalized source/drain current $|I_{DS}|$ of the pristine DPPT-TT and hybrid channel TFTs with different concentrations of MoS_2 as a function of stress time under DC bias.

transport, the interface trap states have more donor-like trap states which will have positive charge when the gate bias is applied. Therefore, V_{TH} could be shifted to the positive bias direction.

Moreover, the threshold voltage shift may be explained by the introduction of interface states generated at the surface of the MoS_2 suspension. When the MoS_2 nanosheet concentration increases in the polymer matrix, interface traps between the polymer and nanosheet will form. This possibility was analyzed using constant gate bias stress to observe the electrical instability in the fabricated devices (see Fig. 4.8). The current (I_{DS}) degradation was measured under a dc gate bias over time. The rapidly degraded current was faster with hybrid thin film TFTs compared to pristine DPPT-TT channel TFTs. The rapid change in the drain current vs. time implies that more charge trap states are induced by the inclusion of the MoS_2 into the polymer matrix. For these situations,

the V_{TH} shift is dependent on the MoS_2 concentrations, and the interface formed by the nanosheet interface with the polymeric semiconductor. Assuming the interface states between the gate dielectric and semiconductor, are constant and behave as acceptor-like trap states and donor-like trap states located in the band gap and near LUMO or HOMO level [140], the defect states introduced by the addition of the suspension were the main contributor to the threshold voltage shift observed at different suspension concentrations. This assumption can be investigated by

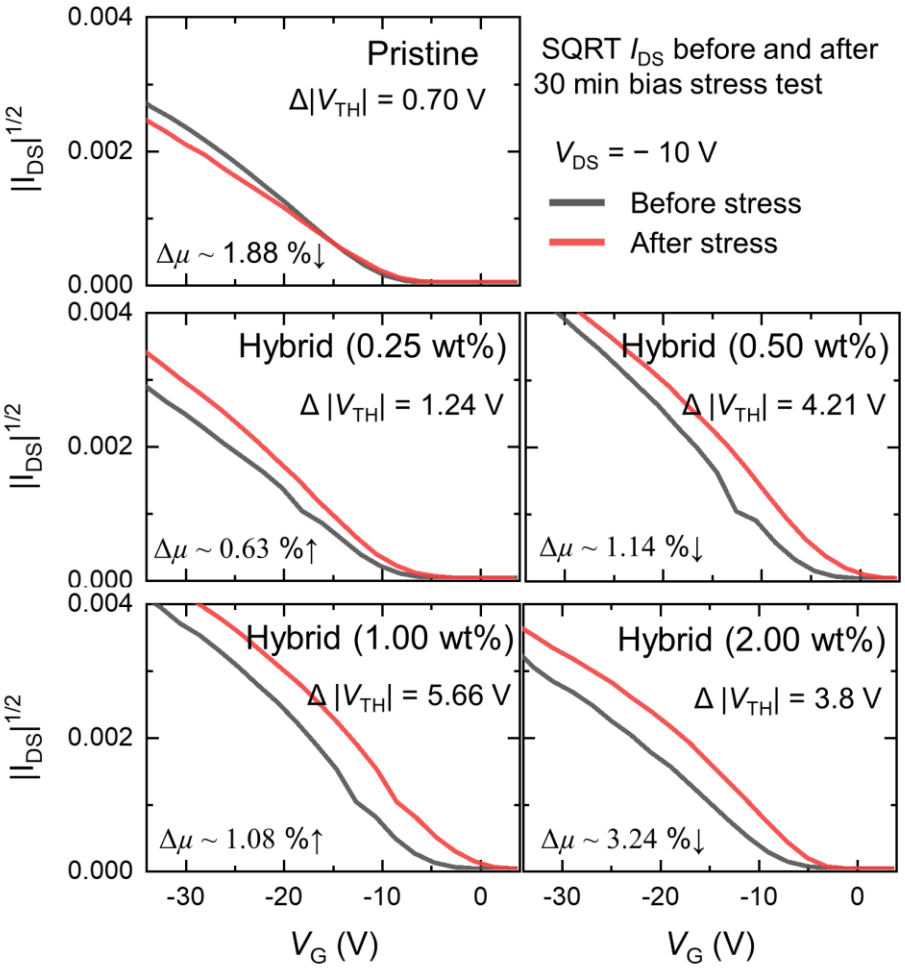

Figure 4.9: $|I_{DS}|^{1/2}$ vs. V_G transfer curves of devices before and after 30 min dc bias stress test to obtain bias induced $|\Delta V_{TH}|$.

measuring a gate bias-induced V_{TH} shift. The transfer characteristics for each device were measured before and after the bias stress test as plotted in Fig. 4.9. The V_{TH} was extracted by the linear extrapolation method from the square root of I_{DS} *vs*. V_G. After bias stress, an observed positive ΔV_{TH} of the hybrid channel TFTs was obtained (depicted as a shift from black to red line). $|\Delta V_{TH}|$ is smallest from the pristine channel TFT ($|\Delta V_{TH}| \sim 0.7$ V) and it is slightly increased to 1.24 V for the TFTs with 0.25 wt% MoS_2. As the MoS_2 concentration increased, the hybrid channel TFTs showed increasing $|\Delta V_{TH}|$ up to 3~5 V compared to the pristine channel TFT. The threshold voltage shift is due to the higher concentration of interface states due to the MoS_2 nanosheet suspensions and the DPPT-TT film. The increased trap states are correlated to V_{TH} shift shown in Fig. 4.6c and d. Assuming this trap density is like other interface states found in the TFT structure, the MoS_2-induced trap density can be estimated by comparing the total trap density (N_{Trap}) of each device. It can be calculated by using the equation: $N_{Trap} = C_{ox}|\Delta V_{TH}|/q$. The calculated N_{Trap} for each device are 1.51×10^{11} cm^{-2}, 2.67×10^{11} cm^{-2}, 9.07×10^{11} cm^{-2}, 1.22×10^{12} cm^{-2}, and 8.18×10^{11} cm^{-2} for pristine, hybrid w/ 0.25 wt% MoS_2, hybrid w/ 0.5 wt% MoS_2, hybrid w/ 1.0 wt% MoS_2, and hybrid w/ 2.0 wt% MoS_2 channel TFTs, respectively. Therefore, the change in trap density for suspension concentrations > 1 wt% of MoS_2 increased by approximately ten times from the pristine film devices. Furthermore, the carrier mobility of the device may experience degradation following the DC bias stress test. However, in this study, the inkjet-printed DPPT-TT and hybrid channel TFTs exhibited remarkable stability in terms of their mobility over a 30-minute bias stress. The alterations in mobilities for each device after the measurements are shown in the bottom-left corner of the plot (Fig. 4.9). These changes in mobility were observed to be within a few percentage points

range, suggesting minimal deviation. This stability is further emphasized by the fact that the extracted mobilities of the fabricated devices showed a maximum change of 7% (as indicated by the error bars), as illustrated in Figure 4.6b.

4.2.3 Improved crystallinity of DPPT-TT by MoS_2 nanosheets

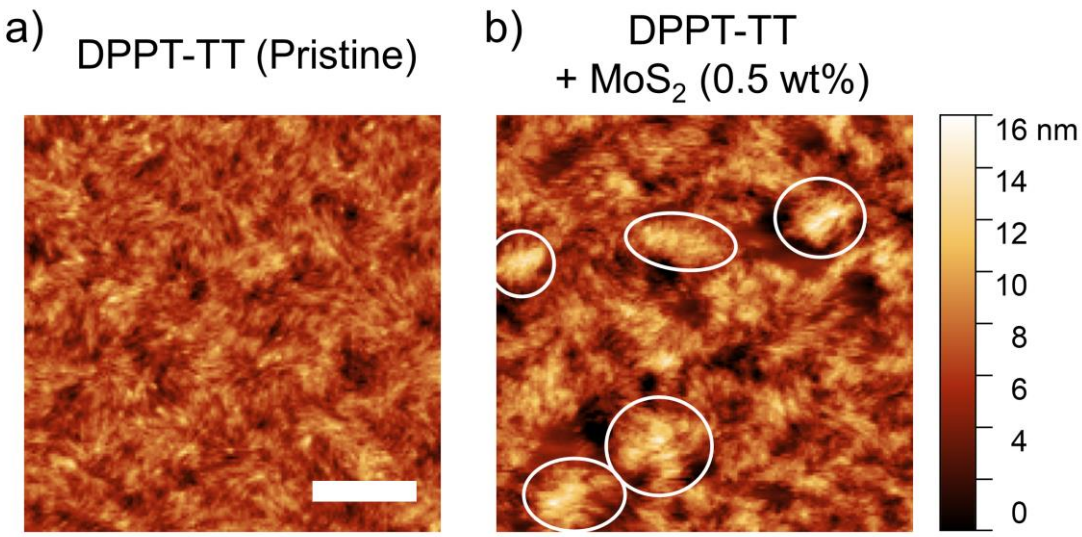

Figure 4.10: AFM image of a) pristine DPPT-TT and b) hybrid nanocomposite film on channel region of TFTs. Scale bar is 1 µm. White circle indicates the closely packed nano fibers and strongly aggregated structure.

Further investigation into the structural effect of the nanosheet suspension on the DA copolymer film provides additional insight into the observed changes in the electrical properties of the TFTs. To investigate the reason for the observed electrical improvement, the microstructure of the DPPT-TT-based thin film was analyzed. The morphology of the backchannel of the TFT was first examined by AFM measurements, comparing the pristine DPPT-TT with the hybrid thin film (at 0.5 wt% MoS_2). The AFM scans are shown in Fig. 4.10a and b. Well-defined fibrillar-like structures can be seen in the pristine film surface, which are loosely packed within the amorphous

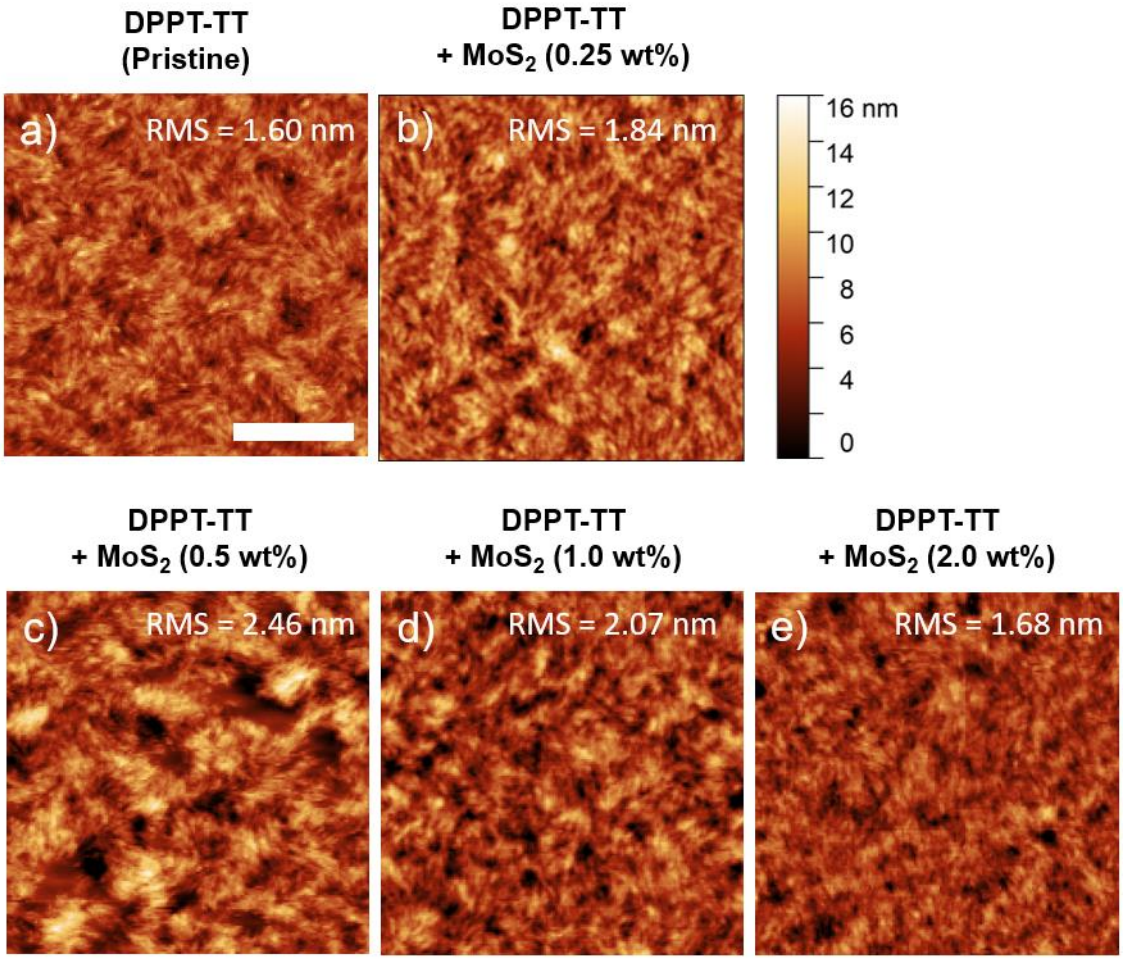

Figure 4.11: AFM height images of all fabricated DPPT-TT thin film with different MoS_2 concentrations such as a) 0, b) 0.25, c) 0.5, d) 1.0, and e) 2.0 wt%. Scale bar is 1 μm.

regions of the film [141]. In the hybrid film, an improved crystallinity of the DPPT-TT may be seen from the AFM scans showing closely packed nanofibers that make up a more strongly aggregated structure (in the white circle). These features suggest a more ordered film that leads to the increased mobility brought on by the suspension of MoS_2 nanosheets in the DPPT-TT thin film. A larger, densely packed polymer domain is created when this polymer is mixed with 0.5 wt% of MoS_2. In this densely packed structure, the polymer has improved π-π stacking, having better inter-

and intramolecular interactions, resulting in enhanced charge transport within the thin film. This observation suggests the suspended nanosheets act as nucleation sites for the ordering of the DA copolymer as the ink dries to form a thin film. At a MoS_2 concentration of 0.5 wt% suspension in the ink, the hybrid channel device showed better mobility than the pristine DPPT-TT channel device in both p- and n-type conductivity (See Fig. 4.6a and b). As the suspension concentration increases, the increasing MoS_2 concentration creates smaller clusters of ordered domains in the thin film. With increasing concentrations of 1.0 and 2.0 wt%, the densely aggregated domains become smaller as the density of nucleation sites for domain formation increases compared to film morphology with 0.5 wt% of MoS_2 (See Fig. 4.11). The increased domain density and decreased domain size introduce more boundary layers between domains that act as scattering sites within the bulk semiconductor [142].

To further investigate the effect of MoS_2 nanosheet on the microstructure of the DPPT-TT matrix, ultraviolet-visible-near infrared (UV-vis-NIR) spectroscopy was carried out, comparing pristine DPPT-TT with the hybrid films (Fig. 4.12). In these samples, the observed (0-0) and (0-1) peaks indicate the existence of a highly ordered aggregation of the polymer, corresponding to the order of intra-chain transfer [143, 144]. The intensity of these peaks increased with the hybrid film containing MoS_2 nanosheet compared to the pristine film. The inset clearly shows that the intensity of (0-0) and (0-1) peaks were moderately increased with 0.25 wt% of MoS_2 and highest when 0.5 wt% of MoS_2 was added, but these peaks decreased with further increased MoS_2 concentration to 1.0 and 2.0 wt%. The increasing structural quality with the addition of the nanosheets suggests there is improved intermolecular interaction between the DPPT-TT polymer chains, resulting in the number of well-ordered DPPT-TT aggregates. However, the hybrid film having 1.0 and 2.0 wt% MoS_2 showed degradation in the (0-0) and (0-1) peaks compared to the

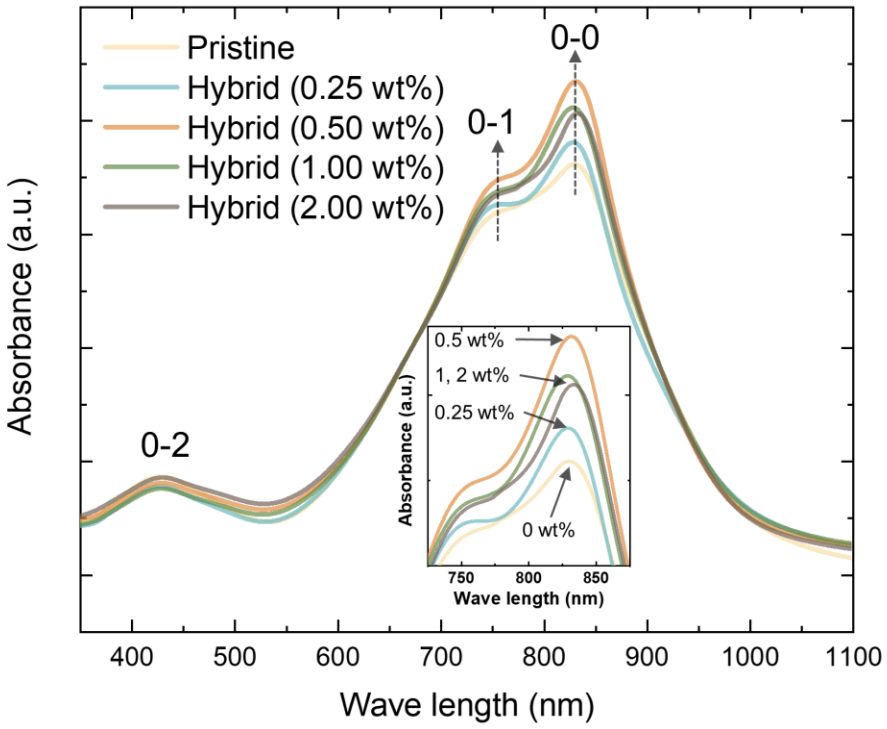

Figure 4.12: UV-vis of pristine DPPT-TT and hybrid thin film with different MoS_2 concentrations (0.25, 0.50, 1.00, and 2.00 wt%). Inset shows the magnified scale of 0-0 and 0-1 peaks of the same spectroscopy results.

film with the 0.5 wt% MoS_2 samples. This result further suggests the MoS_2 may have crossed a concentration threshold in the polymer matrix (higher than 0.5 wt% of MoS_2 in this work) resulting in the hybrid films having less ordered polymeric chains and weaker intermolecular interaction.

To further examine this hypothesis, x-ray diffraction (XRD) was employed to help verify the film structure changes with added MoS_2 suspension. Improved crystallinity in the polymeric thin film is shown in Fig. 4.13. The (*l*00) peak is the reflection from the alkylchain direction (lamellar stacking) that shows the degree of molecular ordering [145]. The pristine thin film XRD showed the (100), (200) reflection, and a weaker (300) peak. The diffraction peaks observed near $2\theta = 15°$

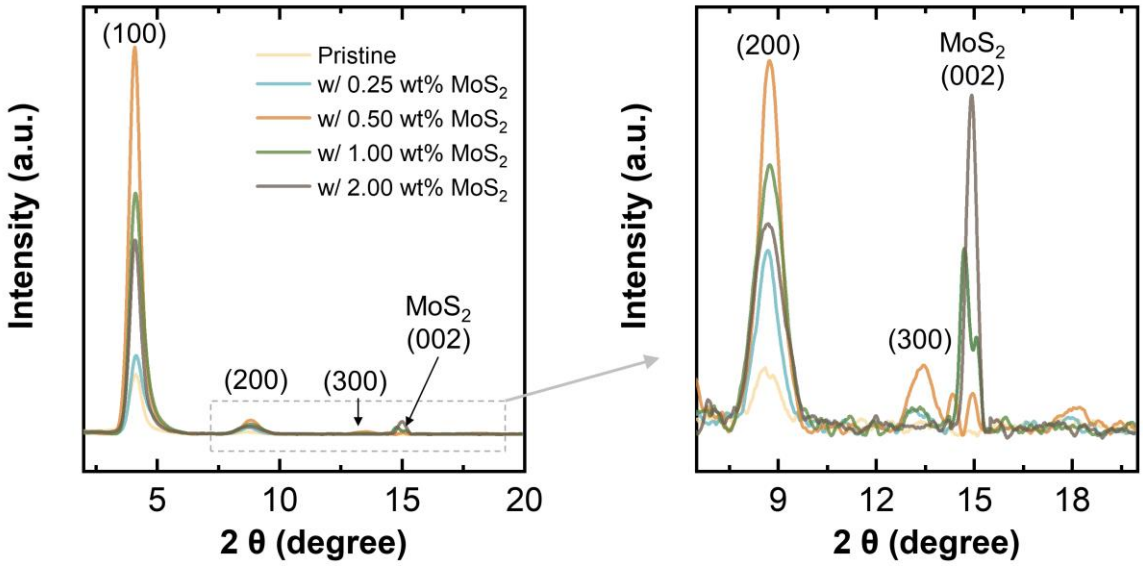

Figure 4.13: XRD spectroscopy results of pristine DPPT-TT and its hybrid thin film with different MoS_2 concentrations (0.25, 0.50, 1.00, and 2.00 wt%). Right figure shows the magnified y-scale to clearly compare (200) and (300) peaks of DPPT-TT and showing (002) peak of MoS_2 nanosheets.

are caused by the (002) reflections of the MoS_2 nanosheet suspension in the DPPT-TT thin film [127, 128]. For the 0.5 wt% suspension in the polymeric ink, the XRD scan showed a strong (100), (200) diffraction peak along with an observable (300) reflection (right side on Fig. 4.13), showing the improved structural quality of the thin-film layer compared to the pristine DPPT-TT. The figure on the right magnifies the y-axis of the intensity vs. 2θ angles (range in the grey dashed line) to compare the (200) and (300) peaks of different thin films. The two peaks from the hybrid film with 0.5 wt% MoS_2 showed a strong intensity, indicating the improved ordering of the DPPT-TT microstructure. On the other hand, further increasing the suspension concentration to 1 or 2 wt% resulted in a degradation in the structural order shown by the XRD scans. For the higher suspension concentrations, the (100) and (200) reflections were attenuated compared to the 0.5 wt% suspension and the (300) peak was not observable from the hybrid film with 2.0 wt% MoS_2 sample,

like what was observed in the pristine films. The results further support the effect of the MoS_2 suspension having both an electrical and structural effect on the DPPT-TT. The hybrid thin films showed strong and clear intensity peaks in XRD spectra, showing a highly ordered lamellar stacked polymer microstructures formed due to the addition of MoS_2 nanosheets in the polymer matrix, supporting the results from the AFM and UV-vis-NIR characterization. As the suspension concentration increased the structural ordering degraded, resulting in a decrease in the electrical performance observed in the extracted electrical parameters from the *I-V* measurement.

4.3 Conclusions

This work demonstrates the use of MoS_2 nanosheets suspended in a DA copolymer film as an effective additive for enhancing the charge transport properties in inkjet-printed TFT devices. The DA copolymer and MoS_2 nanosheet mixtures were formulated to be used as a semiconductor ink for inkjet printing. *I-V* measurements of the fabricated TFTs determined the optimal concentration of MoS_2 suspensions to be 0.5 wt%. These devices showed enhanced field-effect mobility in both hole and electron transport compared to the pristine inks. Hole and electron mobilities were increased by 52 % and 130 % each for the 0.5 wt% hybrid inks compared to pristine inks without the suspension. The improved carrier transport was determined to be affected by structural changes in the DA copolymer film nucleating from the surfaces of the nanosheets, resulting in ordered structures within the polymeric film. The microstructure of DPPT-TT based thin film was analyzed by AFM, UV-vis-NIR, and XRD characterization. The results showed that introduced MoS_2 nanosheets induced the strongly aggregated polymer domains and a high degree of molecular ordering within the polymer. As the concentration of the suspension increased (> 0.5 wt% MoS_2), the structural quality of the film was found to degrade due to a higher density of nucleation sited for aggregation of the polymer with higher MoS_2 concentration. As a result, the density of domain

boundaries formed in the film caused an increase in carrier scattering that reduced the electrical performance of the TFT.

Chapter 5
Inkjet-printed silver nanoparticles for source/drain electrodes of TFT

5.1 Introduction

Previous research work has demonstrated the enhanced performance of polymer channel thin-film transistors (TFTs) through the incorporation of MoS_2 nanosheets. However, the TFTs fabricated in previous studies have utilized vacuum-deposited source and drain (S/D) electrodes. To advance this research, the investigation is expanded to fully inkjet-printed TFTs, which is crucial for the development of roll-to-roll processing. This method offers a significant advantage over traditional fabrication techniques.

This chapter presents a study on inkjet-printed silver nanoparticles (Ag NPs) as electrodes for thin-film transistors (TFTs). One of the main challenges associated with the inkjet printing of conductive materials, such as gold, silver, copper nanoparticles [35-37], carbon nanotubes (CNTs) [38], or PEDOT:PSS [40, 41], is the difficulty of depositing a highly uniform and flat thin film when compared to thermally vacuum-deposited electrodes. Consequently, this geometric difference results in an increased contact resistance (R_C), which is an inherent limitation of printed electrodes for TFT applications. Generally, the organic semiconductors have poor morphology near the surface of electrodes in BCBG structure and cause higher contact resistance (R_C) [146-148]. Conventional Si-based MOSFET has 0.1 Ω·cm of R_C. On the contrary, well-controlled low R_C of OTFT has been reported as less than 100 Ω·cm, but usually higher R_C has been reported from a few kΩ·cm to a few hundreds MΩ·cm with various organic semiconductors and electrode materials when contact engineering is applied (such as employing a self-assembled monolayer (SAM) or charge injection layers between the electrodes and semiconductors) [131, 146, 149].

Although contact engineering for TFTs has been developed and reported to reduce contact resistance and improve device performance, the current work presents a new approach to improve the TFT performance which suffers from printed electrodes using a hybrid semiconductor. The combination of inkjet printing and hybrid semiconductor technology appears very promising for the realization of high-performance inkjet-printed TFTs.

5.2 Results and discussions

5.2.1 IJP Ag NP thin-film conductivity

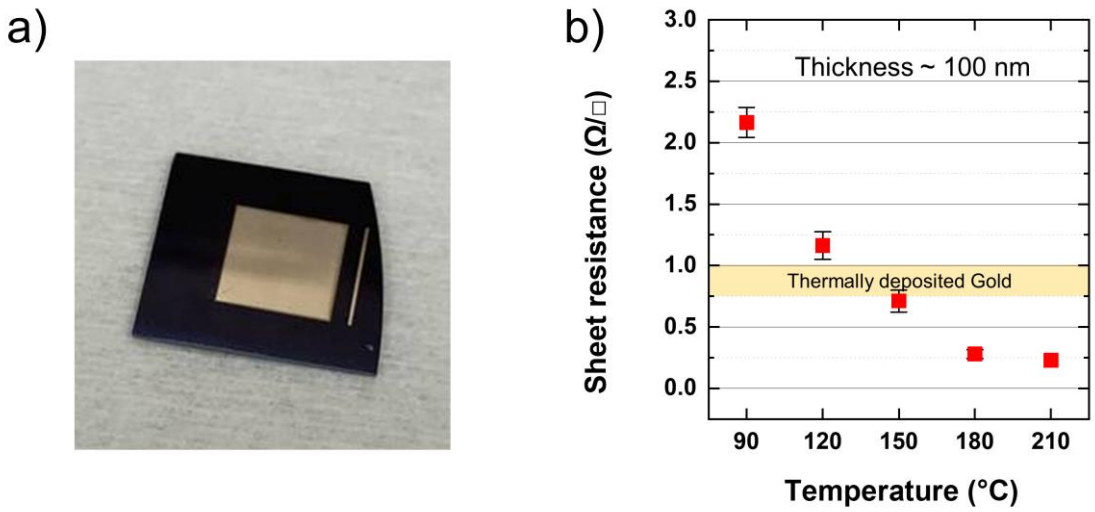

Figure 5.1: (a) Inkjet-printed Ag square shaped thin film (1 × 1 cm) on SiO_2/Si wafer. (b) Sheet resistance of printed Ag thin film as a function of sintering temperature.

For S/D electrodes of the TFTs, a low resistivity for a printed Ag film is desired since the film conductivity of the metal and the work function of the semiconductor are directly related to charge injection at the contact. The contact resistance is determined from these properties that affect the charge injection [150]. As discussed earlier in Chapter 1.5, the sintering process, and the formation of thin films from Ag NPs inks need to be optimized to form printed metallic contacts. The

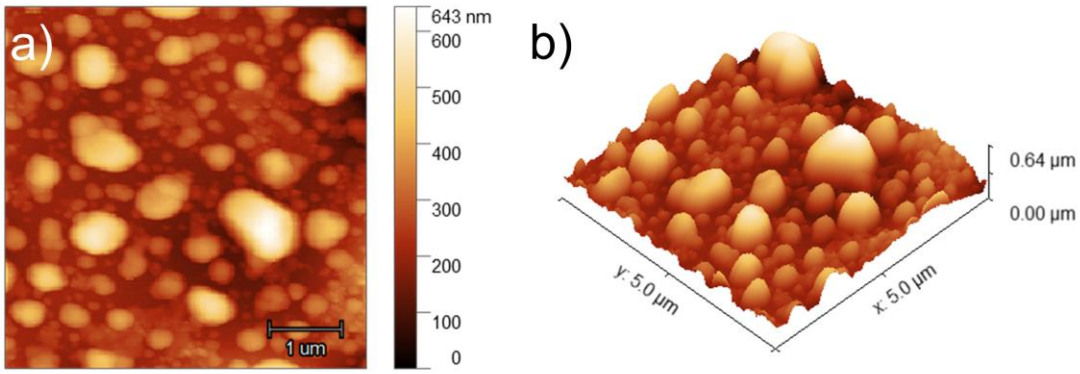

Figure 5.2: AFM height image of printed Ag thin film sintered at 240 °C in (a) 2D and (b) 3D view.

optimum sintering temperature is dependent on annealing methods, the surface energy of the substrate, and the volume of printed ink on a given area. During the sintering process, changes in the film density, the surface wetting of the film, electrical conductivity, and pattern geometry affect the final electrical contact between the metal and semiconductor. The optimized sintering temperature of this inkjet-printed Ag thin film was explored with this fixed process condition introduced in Chapter 2.3. To evaluate the resistivity of the printed Ag thin film, large area (1 × 1 cm) square shapes were printed (Fig. 5.1a.) and sintered at temperatures of 90 °C, 120 °C, 150 °C, 180 °C, 210 °C, and 240 °C. The sheet resistance of the inkjet-printed Ag film as a function of Ag sintering temperature (T_{Ag}) was measured by using a four-point probe system and shown in Fig. 5.1b. The sheet resistance decreased with increasing T_{Ag}. The higher T_{Ag} induced Ag NPs to coalesce having a more continuous electrical transport path and improving the conductivity. However, when T_{Ag} is 240 °C, the sheet resistance could not be measured because the Ag NPs formed discontinuous islands (Fig. 5.2) as a result of the Ag ink dewetting from the oxide surface, resulting in an electrical open circuit in the line patterns. The sheet resistance values, using sintering temperatures of 180 °C and 210 °C, were comparable to previous reports [151]. An

annealing temperature of 150 °C was also selected as a comparison to other samples since the sheet resistance at 150 °C was still below the value from the thermally deposited gold film (the yellow region in Fig. 5.1b). The reference gold film had a 30 nm thickness, with sheet resistances in the range of 0.75 ~ 1 Ω/sq.

The film resistivity can be calculated from the four-point probe measurements by using the equation for sheet resistance: $R_s = \rho/t$, where R_s is the sheet resistance, ρ is resistivity, and t is the thickness of the film. A thermally deposited gold thin film (t ~ 30 nm) and the printed Ag thin film (t ~ 100 nm) sintered at 210 °C had resistivities of ~2.57×10^{-2} μΩ·m and 2.28×10^{-2} μΩ·m, respectively. The gold thin films are very close to its intrinsic electrical resistivity of 2.2×10^{-2} μΩ·m at room temperature, but the printed Ag thin film was slightly higher than the intrinsic resistivity of the bulk silver (approximately 1.65×10^{-2} μΩ·m at room temperature). However, the resistivity of the printed Ag film was similar or lower than recently reported values (2~3×10^{-2} μΩ·m [152] and 6.45×10^{-2} μΩ·m [153]). Consequently, the Ag thin film fabricated in this study were comparable to previous reported values demonstrating a state-of-the-art level of electrical conductivity and a viable candidate for an electrode in TFTs.

To investigate the effect of T_{Ag} on the morphologies of the film, three different sintering temperatures, 150 °C, 180 °C, and 210 °C are selected since their electrical property (sheet resistance) was comparable to that of vacuum-deposited gold thin film. The surface morphologies of these samples were investigated by SEM, which is shown in Fig. 5.3. When T_{Ag} increases from 150 °C to 210 °C, the SEM characterization was used to observe the structural transformation of the nanoparticle as a function of annealing temperature. At T_{Ag} = 150 °C (Fig. 5.3a), the Ag nanoparticles were found to form a thin necked region between particles. At T_{Ag} = 180 °C (Fig. 5.3b), most of the Ag nanoparticles sintered with neighbouring particles, forming a more

continuous film, transformed from the spherical shape of a single Ag nanoparticle shown in the SEM image. At T_{Ag} = 210 °C (Fig. 5.3c), the Ag nanoparticles were observed to form large Ag clusters and empty voids due to the dewetting of the Ag from the substrate surface. This film has

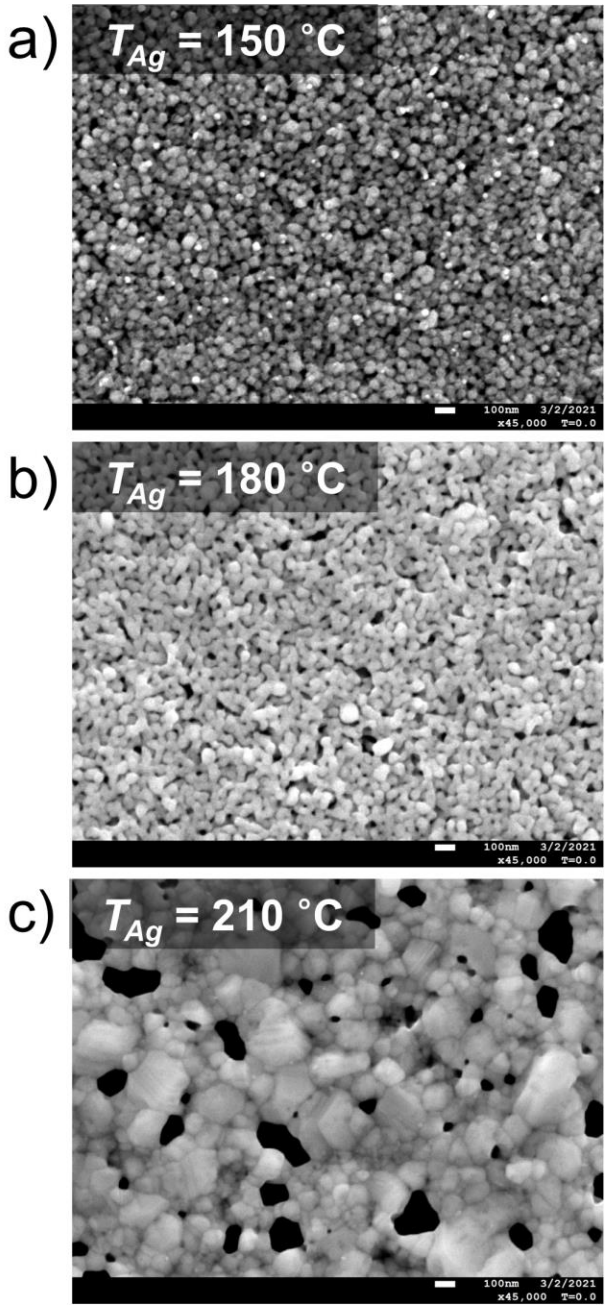

Figure 5.3: SEM images of surface of printed Ag thin films sintered at different temperatures: (a) 150 °C, (b) 180 °C, and (c) 210 °C.

the lowest sheet resistance among prepared samples. From these results, a temperature of 210 °C was determined to be the optimized condition for printed Ag thin films, achieving the best electrical conductivity.

5.2.2 Effect of morphology on the contact resistance of TFTs

In this section, the effect of the printed Ag morphology on the contact resistance (R_C) of the TFTs is explored. For source/drain (S/D) electrodes in TFTs, the metal contact should have a uniform and very well-defined edge in a line shape. Figure 5.4b shows inkjet-printed Ag NPs pattern for S/D contacts that have well defined sidewall and uniform patterning of the electrodes.

Using the printing conditions described in Chapter 2.3, the Ag lines were sintered to form a metallic pattern. Following the sintering process, the surface of the substrate was treated with HMDS and P3HT was printed onto the S/D pattern (Fig. 5.4c). The as-printed P3HT ink was confined within the S/D regions defining the channel, since the HMDS-treated SiO_2 surface has a lower surface energy than that of the Ag film. In Fig. 5.4d, a plan-view image of a fabricated BGBC

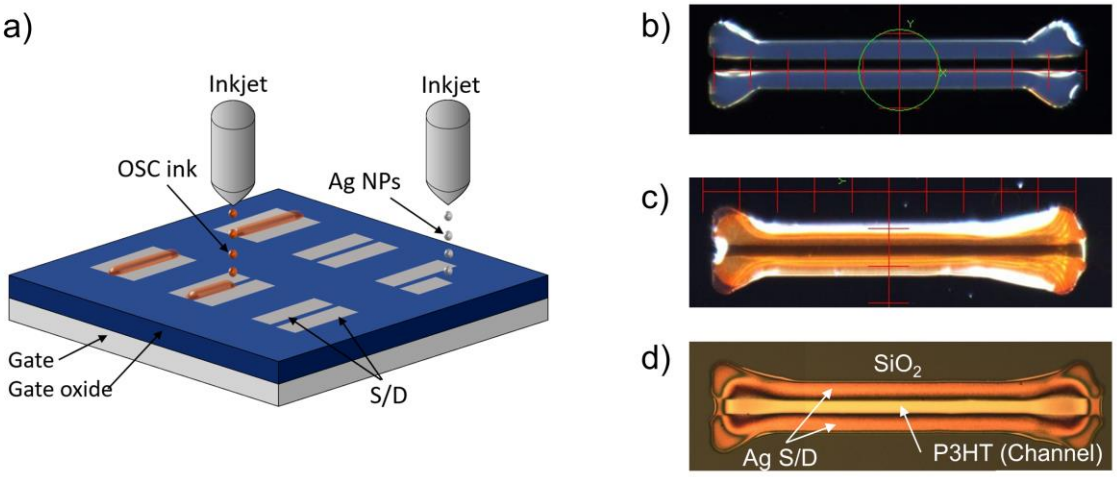

Figure 5.4: (a) Inkjet printed Ag S/D and polymer ink for a TFT fabrication process. (b) As-printed Ag S/D pattern. (c) As-printed P3HT on Ag S/D pattern and it is kept in printed area. (c) Optical micrograph of a fabricated BCBG TFT structure. The S/D and channel regions are well defined.

inkjet-printed P3HT channel and Ag S/D TFT is shown. The device has a geometry with a 30 µm channel length and 900 µm channel width (decreased from 1 mm due to the evaporated solvent).

In the previous section, the different morphologies of printed Ag were obtained by changing T_{Ag}. The P3HT channel of the TFTs were fabricated using Ag S/D contacts sintered with three different T_{Ag}. The measured transfer characteristics of the TFTs are shown in Fig. 5.5. All fabricated TFTs showed good switching behavior with high current on/off ratios. The on/off ratio of each device was measured to be 2.7×10^3 for TFTs sintered at 150 °C to 9.0×10^3 for TFTs sintered at 210 °C.

The extracted μ_{sat} for each device are summarized in Fig. 5.6. The μ_{sat} increased with higher sintering temperatures. In this context, the sole distinguishing factor among the samples was the

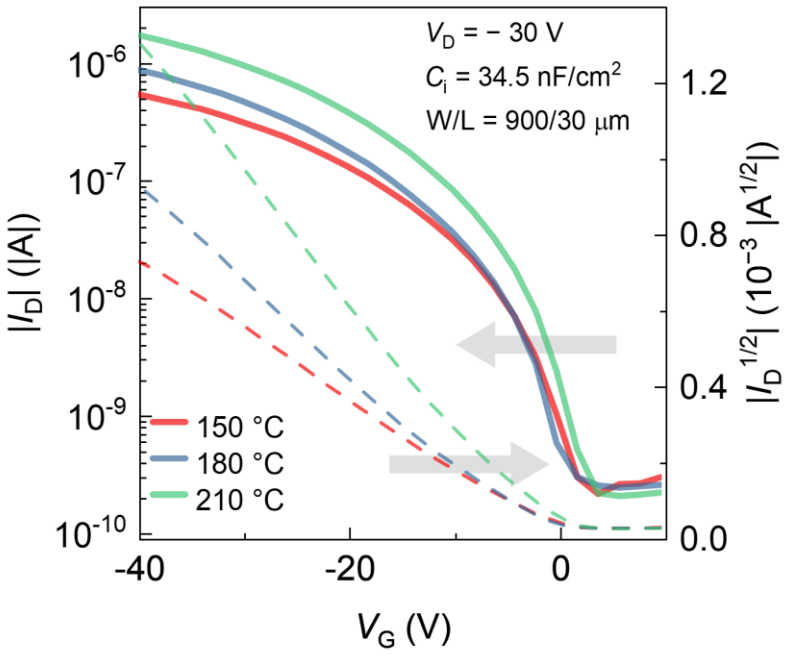

Figure 5.5: Transfer characteristics of inkjet-printed P3HT TFTs with Ag S/D which prepared at different sintering temperatures such as 150, 180 and 210 °C. Logscale and square root of drain current level on left and right axis, respectively.

annealing temperature, which impacted the metallic resistivity. The R_C of the TFTs can be calculated by the *Y*-function method (YFM) that could be used to extract the R_C independent of V_G [149, 154, 155]. Thus, it is more suitable for co-planar TFT structures than staggered structures since the latter structure may be affected by a current crowding effect at the interface between electrodes and a semiconductor [156], where R_C was dependent on the V_G in the co-planar structure [157]. To extract the contact resistance, the *Y*-function ($Y = \frac{I_D}{\sqrt{|g_m|}}$) is extracted as a function of V_G within the linear regime (V_D = − 1 V) by using the *I*-*V* measurement result of each device. Additionally, the obtained contact resistance from the YFM method was verified as compared to the transfer length method (TLM) method (see Fig. C2).

The calculation of the R_C involves extracting the slope of the *Y*-V_G curve in the linear region for each device, and the results are shown in Figure 5.6a [158]. It was observed that the R_C diminishes with an increasing sintering temperature. Notably, the change in R_C exceeds one order of magnitude

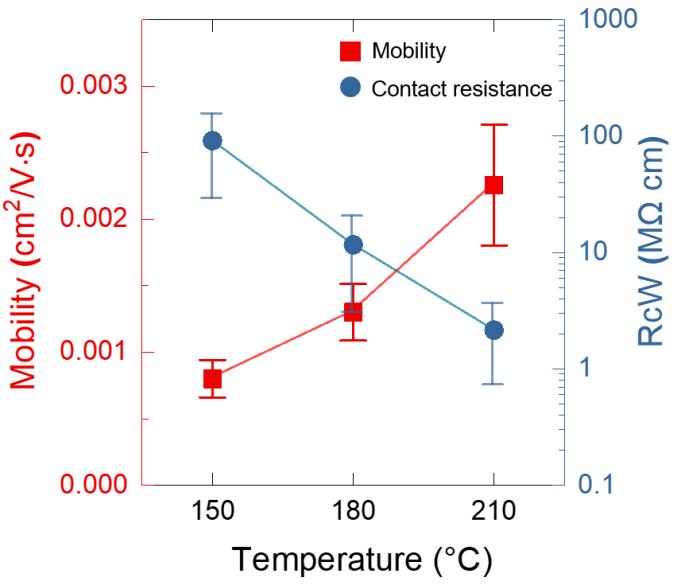

Figure 5.6: Carrier mobilities and contact resistance as a function of sintering temperatures.

from 150 °C and 210 °C sintering temperatures. It is worth mentioning that although the sheet resistance of the two different sintering temperatures, namely 180 °C and 210 °C, was comparable at approximately 0.25 Ω/sq (Figure 5.1), the extracted values for both μ_{sat} and R_C exhibited

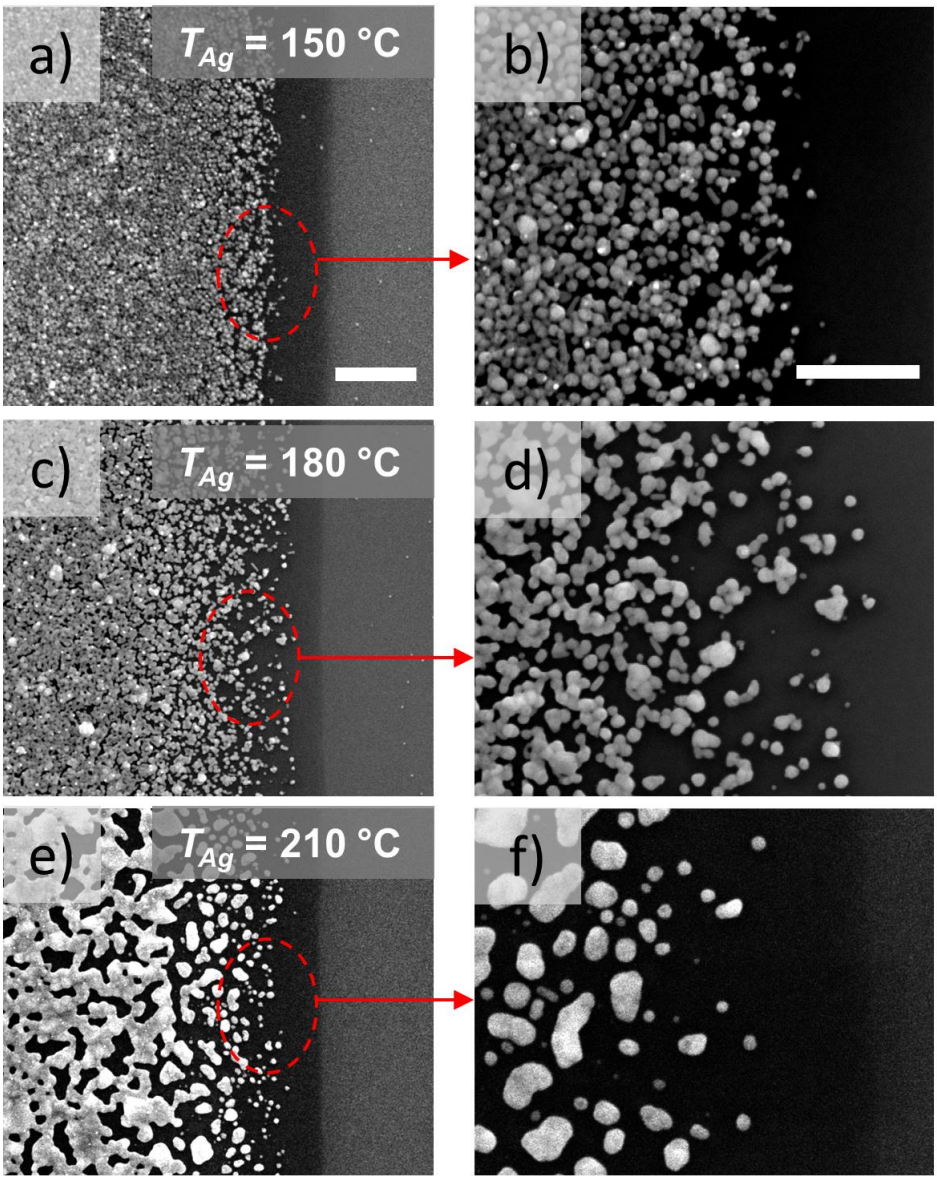

Figure 5.7: SEM micrographs at the edge of the printed silver electrodes which are sintered at: (a) 150 °C, (c) 180 °C and, (e) 210 °C (scale bar is 1 µm). The right column (Figs. 5.7 b, d, f) shows a higher magnification image of the line edge of printed pattern.

improvements with higher sintering temperatures up to 210 °C were nearly identical but the contact resistance was found to increase by nearly 10×.

The printed Ag thin films also have a non-flat and non-uniform surface that were observed in the SEM scan (Fig. 5.3). This morphology may be the reason for the increasing the R_C of the devices. Fig. 5.7 shows SEM images at the edge of different sintered Ag S/D electrodes. The large clusters of a continuous Ag film form in the bulk of the Ag S/D region (left side in the SEM image) with a 210 °C sintering temperature is applied. However, when the Ag film is sintered at 150 °C, most of the Ag nanoparticles were not sintered well. The formation of the typical necked structures was absent at this temperature suggesting the nanoparticles did not fully form a film during the sintering process. The resulting structures were like discrete Ag NPs creating an inefficient conductive pathway in the metallic film. The film sintered at 180 °C was found to have an improved sintering process, with most of the particles having merged with their adjacent particles. From these results, the large cluster shape of Ag film (T_{Ag} = 210 °C) was more structurally effective for charge injection and has relatively reduced R_C due to a wider and larger contact area as an interface to the semiconductor.

Unlike the bulk of the printed Ag film, the islands formed in the printed pattern were created near the edge of the contact where the semiconductor and the S/D are in contact. The morphology of this interface is dependent on the surface energy of SiO_2 surface which is not typically treated with a SAM prior to printing the Ag in the TFTs reported in this thesis. When the printed Ag ink is dried, the contact line at the edge of the printed pattern is pinned due to the high surface energy of the SiO_2 surface. When the Ag nanoparticles were sintered and merged into a solid, the nanoparticles near the edge (Fig. 5.7 b, d, and f) do not participate in the agglomeration to the bulk, dewetting from the oxide surface and forming small island clusters This island-like pattern creates

a discontinuous electrical contact at the edge of the channel region, limiting charge injection into the semiconductor and affecting the TFT parameters; the surface roughness may also affect the formation of the polymeric film, and hinders the ordering of the crystalline structure. These islanded edges along the printed electrodes are a typical feature of printed metal lines and are a critical difference compared to vacuum deposited and photolithographically defined contacts used to fabricate the devices in the previous chapters.

The reason for the increased R_C from a TFT with the Ag S/D sintered at 210 °C may be due to improved charge injection at the line edge between the semiconductor-metal contact interface. To verify this assumption, the surface morphology of the P3HT was characterized using the AFM

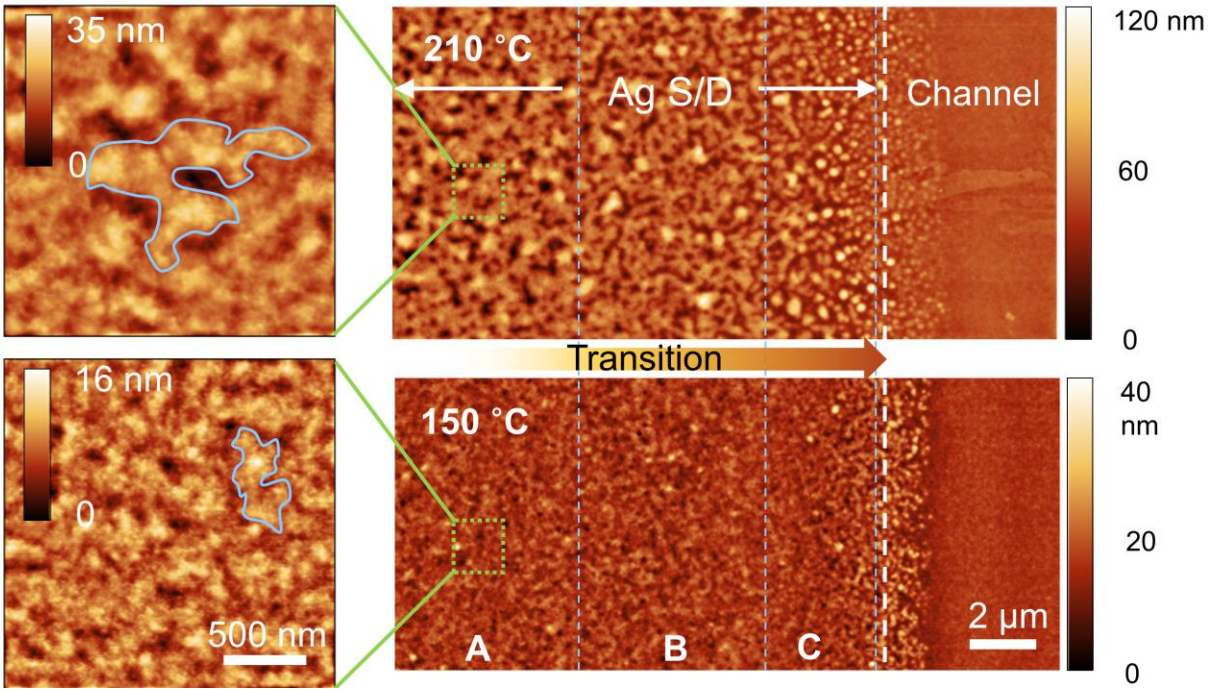

Figure 5.8: AFM height images of P3HT film from two different devices having different sintering temperatures, 210° C (top) and 150 °C (bottom) with higher magnification AFM images (left) of the surface at the middle of S/D region.

height mode on fabricated TFTs near the S/D and channel region of two different devices (150 °C

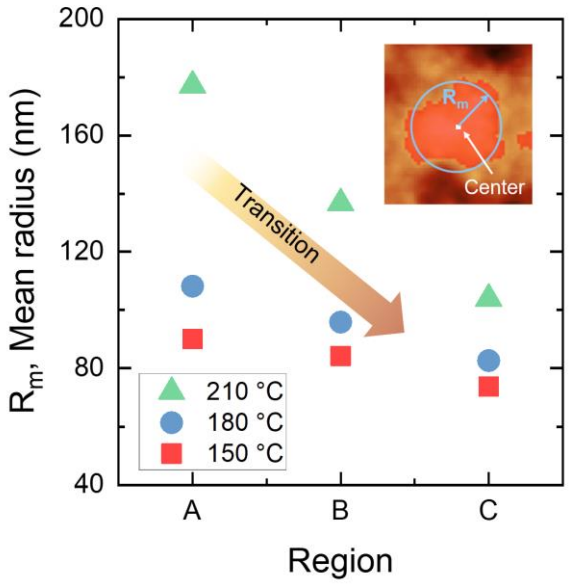

Figure 5.9: The average mean radius of each grain of P3HT film in three regions on the S/D region.

and 210 °C) shown in Fig. 5.8. The overall different P3HT domain size can be distinguished from the AFM image. The polymer domain size on the Ag S/D area of the TFT sintered at 210°C is larger than that on the Ag S/D region of TFT sintered at 150°C. It is depicted as the highlighted blue outline in the higher magnification AFM scan on the left side of Fig. 5.8. The polymer is predisposed to have long-range ordered microstructure within a large domain [160]. Even if the size of the P3HT domain is continuously decreased from the S/D electrode region to the channel region, the larger domain size of the 210°C samples can be maintained at the edge of S/D region.

To quantify this result, the three regions are divided into A, B, and C. Then, from the AFM image, the domain distribution of P3HT film is calculated by setting the threshold height by using an image processing software. The mean radius (R_m) (see inset of Fig. 5.9) was used to decide the average domain size and the average R_m is extracted from all domains in the AFM image for each

region, A, B, and C shown in Fig. 5.9. In the case of 210°C (green triangle), the R_m has a 180 and 140 nm in region A and B, respectively, but it decreases to ~100 nm in region C. However, in the case of the 150°C annealing temperature (red square outline), the average domain size is smaller than 100 nm in all regions. In region C where the interface is located, the polymer domain size of the 210 °C annealed samples is larger than the other annealing conditions. The 150°C sample showed the Ag nanoparticles were poorly sintered, which causes a high surface roughness and suggests the P3HT film to be more disordered compared to the other sample regions. On the contrary, in the case of 210°C, the large flat area of Ag electrodes gives more area for the P3HT film to form on a flat uniform surface for larger polymeric domains. The larger domains provide better microstructures that result in improved carrier transport in the semiconductor [160]. Therefore, the TFT with the Ag S/D sintered at 210 °C showed improved μ_{sat} and reduced R_C due to the better charge injection property.

This study has yielded insights into the interplay between the electrical properties of TFTs (in terms of contact resistance and extracted carrier mobility) and the morphologies of Ag and P3HT films. The aforementioned factors have been found to be contingent upon the morphology of the P3HT film, which in turn, is influenced by the morphology of the Ag film.

5.2.3 Comparative study of contact resistance between vacuum deposited gold and printed silver electrodes

In the previous section, it was revealed that the R_C of the fabricated IJP TFTs depends on the morphology of the printed silver thin-film structure. Since the vacuum-deposited metal electrodes were more uniform with less surface roughness than the printed silver electrodes, it is worthwhile to compare these two different electrodes. The devices fabricated in previous studies (chapters 3 and 4) had thermally vacuum-deposited gold electrodes. The extracted electrical characteristics,

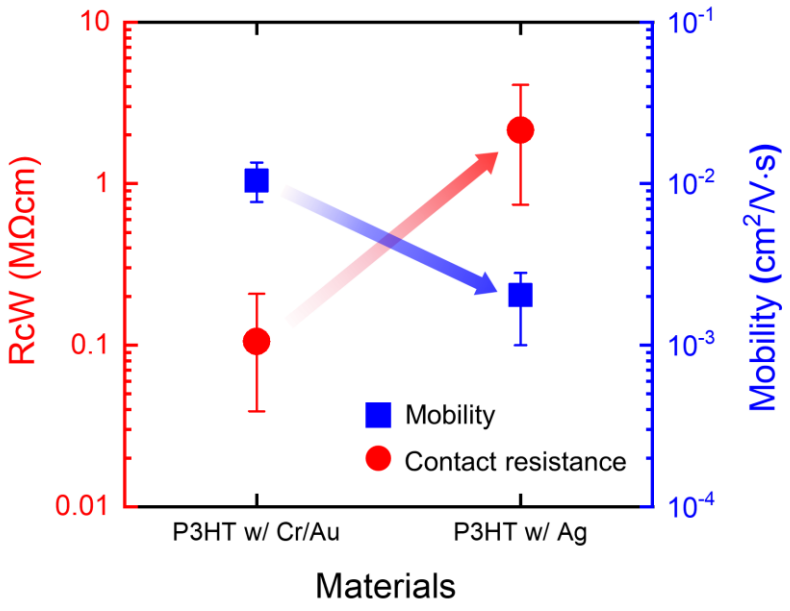

Figure 5.10: Comparing two different electrodes: thermally deposited gold and inkjet-printed silver. The electrical characteristics of the TFT contact resistance (left axis) and field-effect carrier mobility (right axis) for each electrode structure.

contact resistance, and field effect mobility, of inkjet-printed P3HT channel TFTs with different electrode materials, are summarized in Fig. 5.10. As expected, thermally vacuum-deposited gold gives lower contact resistance compared to inkjet-printed TFTs with silver electrodes, since vacuum deposition can create a uniform and smooth surface of metal electrodes which leads to better electrical contact. On the other hand, the inkjet printing method results in surface roughness and non-uniformity of metal electrodes which increase contact resistance and degrade the extracted field-effect mobility.

In addition, the R_C effect is also observed in the output characteristics of devices (see Fig. C3) which is compared to the device having the vacuum deposited gold contact. Since the inkjet-printed Ag S/D caused higher contact resistance than the Au S/D, the S-shaped curve is more clearly observed in the linear regime of output curves from the TFTs with printed Ag S/D.

The work function of the metal is also considered since it is related to the barrier height for charge injection due to band bending at the interface between the semiconductor and metal contact. It is known that the vacuum deposited gold thin film has a −5.2 eV work function and inkjet printed silver is −4.9 eV. The work functions may be modified by using pentafluorobenzenthiol (PFBT) which is widely used and well-known as a modifier for inkjet-printed silver films [150]. In this case, the work function of the printed silver film increases to −5.24 eV [150], but the experimental result conducted in this study shows that the electrical characteristics did not change (Fig. C4a) after the surface of the printed silver film was treated with PFBT (Fig. C4b, c).

The BCBG configuration of the TFT may lead to a more pronounced degradation of device performance, particularly concerning contact resistance. As depicted in Figure 5.11, the bottom contact, also known as the co-planar structure, exhibits a smaller charge injection area at the interface between the semiconductor and metal electrodes compared to the top contact TFT structure. This is due to the fact that the channel layer forms at the bottom of the organic semiconductor within a few nanometers from the dielectric-semiconductor interface [161], resulting in a small areal contact for charge injection area in the co-planar structure. Conversely, the top contact structure provides a wider area for the charge injection, as indicated by the red arrows in Figure 5.11b. Charge carriers can effectively transport through this larger injection area. Nevertheless, the bottom-contact TFT structure is necessary in TFT fabrication technology for improved processability. For instance, metal electrodes typically require higher processing temperatures, exceeding 200 °C, than organic materials. Polymer semiconductors are sensitive to high temperatures. Consequently, fabricating the top contact structure may risk damaging the organic semiconductor layers underneath the metal electrodes or necessitate a meticulous selection

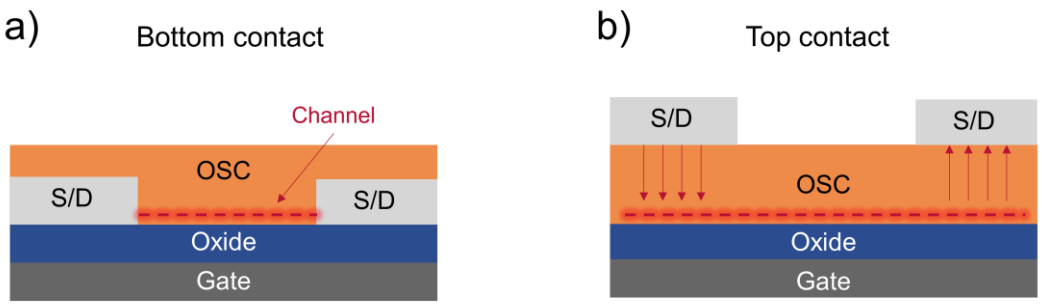

Figure 5.11: TFT structures for a: (a) bottom contact and (b) top contact. Channel layer is depicted as red dashed lines. In the bottom contact structure, the channel meets at the edge of the S/D electrodes, and charge carriers are injected over a smaller area compared to the top contact structure where charge carriers are injected and flows in relatively large area than bottom contact.

of materials for the electrodes. Therefore, in a bottom contact structure, a thorough investigation of the interface region at the edge becomes crucial, as its characteristics significantly affect the contact properties.

In the previous chapter, a non-uniform morphology was observed in the printed Ag thin film under SEM analysis. This nonuniformity represents a major distinction from vacuum-deposited metal thin films, which typically exhibit a uniform and smooth flat surface, as evidenced by the AFM scan shown in Figure 5.12. The AFM images depict thermally deposited Au and printed Ag electrodes before the P3HT film is printed, resulting in bare metal electrodes without the presence of the polymer. The root mean square roughness (RMS) of the gold electrode is approximately 11 nm, significantly lower than that of the silver film (~28 nm RMS). Furthermore, the RMS of Au is mainly due to the presence of hillock-like structures (bright areas in the AFM scan), with much of the surface area appearing flat. In contrast, the printed silver film exhibits substantial roughness. In the 3D view of the AFM image, the gold film demonstrates a vertical flat edge, whereas the

printed silver film displays considerable roughness. Given that the accumulation layer is formed just a few nanometers from the surface of the organic semiconductor (OSC) film [161], the interface between the electrodes and the OSC can be distinctly defined with Au. However, it appears to be rougher when the electrodes are printed with Ag. This structural difference at the edge in these two metal contacts may explain why inkjet-printed silver electrodes lead to higher contact resistance when compared to thermally vacuum-deposited gold even as the bulk conductivity (Fig. 5.1b) suggests the silver contacts should have lower contact resistance.

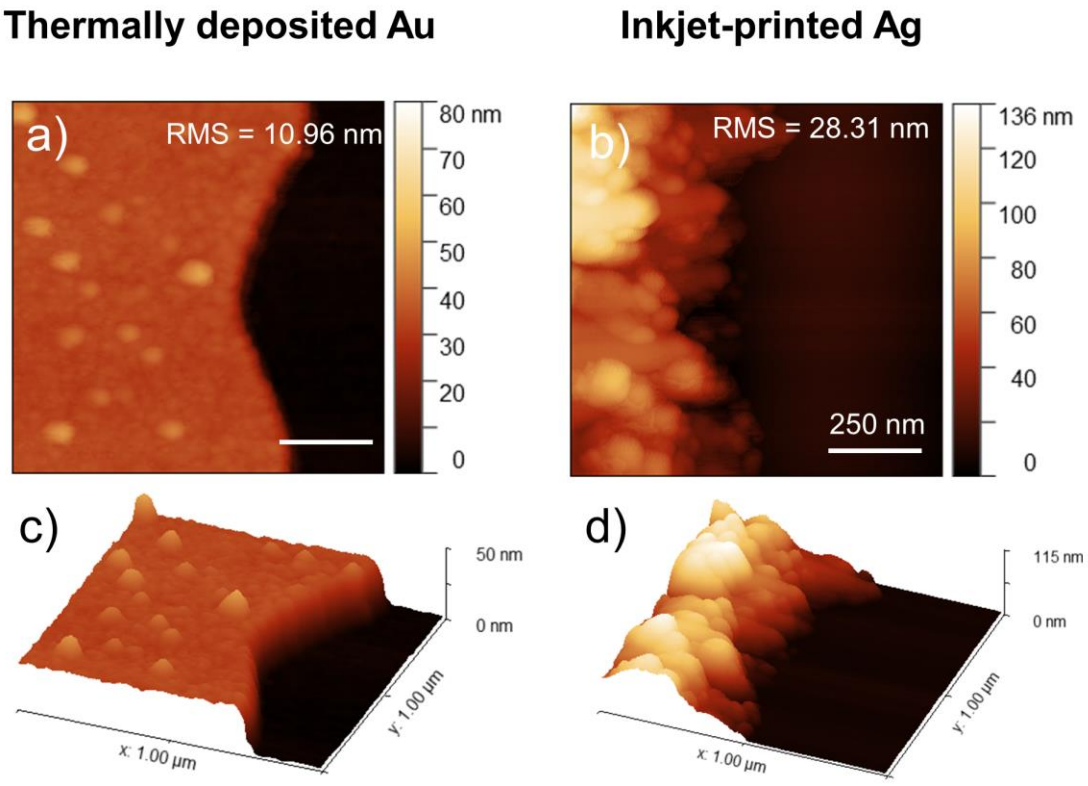

Figure 5.12: Comparing two different electrodes, thermally deposited gold and inkjet-printed silver thin film electrodes of the TFT structure. The AFM height image at the edge of (a) gold and (b) silver electrodes. 3D view for same edge of (c) gold and (d) silver thin film.

SEM analysis more clearly reveals this structural difference showing an island formation near the edge of printed Ag electrodes shown in Fig. 5.13. The pattern of the Au contact has flat edges, and the S/D region is clearly defined by the photolithography process (Fig. 5.13a) Unlike the continuously deposited vacuum deposition method, the printed silver thin film has discontinuities, especially at the edge of the printed electrodes, that may create a series resistance between the formed accumulation layer in the semiconductor and the electrode. This edge roughness may increase the carrier scattering [162] due to poor packing or ordering of polymer chains [163] along the edge of the printed contact line, then these effects degrade the overall charge transfer or injection between the electrodes and semiconductor. Hence, a higher contact resistance is observed compared to TFTs with vacuum-deposited gold contacts.

Fig. 5.14 presents schematic illustrations of printed Ag S/D electrodes and the various components of resistances in the TFT structure. At the edge of the printed silver, a tapered cross-sectional profile (see Fig. 5.14b) is also observed due to wetting of the Ag ink on the substrate surface. This cross-sectional profile along with the islands of discontinuous film necessitates

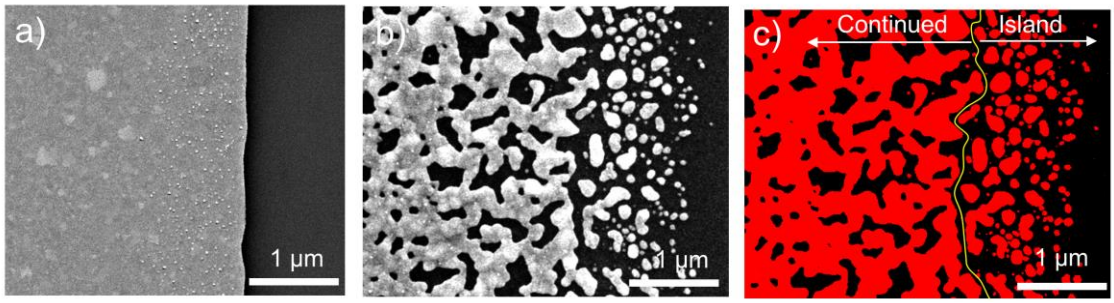

Figure 5.13: SEM micrographs at the edge of the: (a) gold and (b) silver electrodes. (c) Image processed SEM micrograph enhancing the contrast of the island features along the edge of the printed line. The solid line in the middle separates two regions, a continuously connected nonuniform film (left side) and a discontinuous island formation region (right side) which does not contribute the electrical conductivity as S/D electrodes.

consideration of an additional contact resistance component, denoted as R_{C_edge}, which arises from the profile at the edge of the line and the thickness of the accumulation layer in the semiconductor. As a result, the total resistance (R_T) can be expressed as a resistance in series with the channel resistance (R_{ch}) and the contact resistance that has two distinct components: the traditional contact

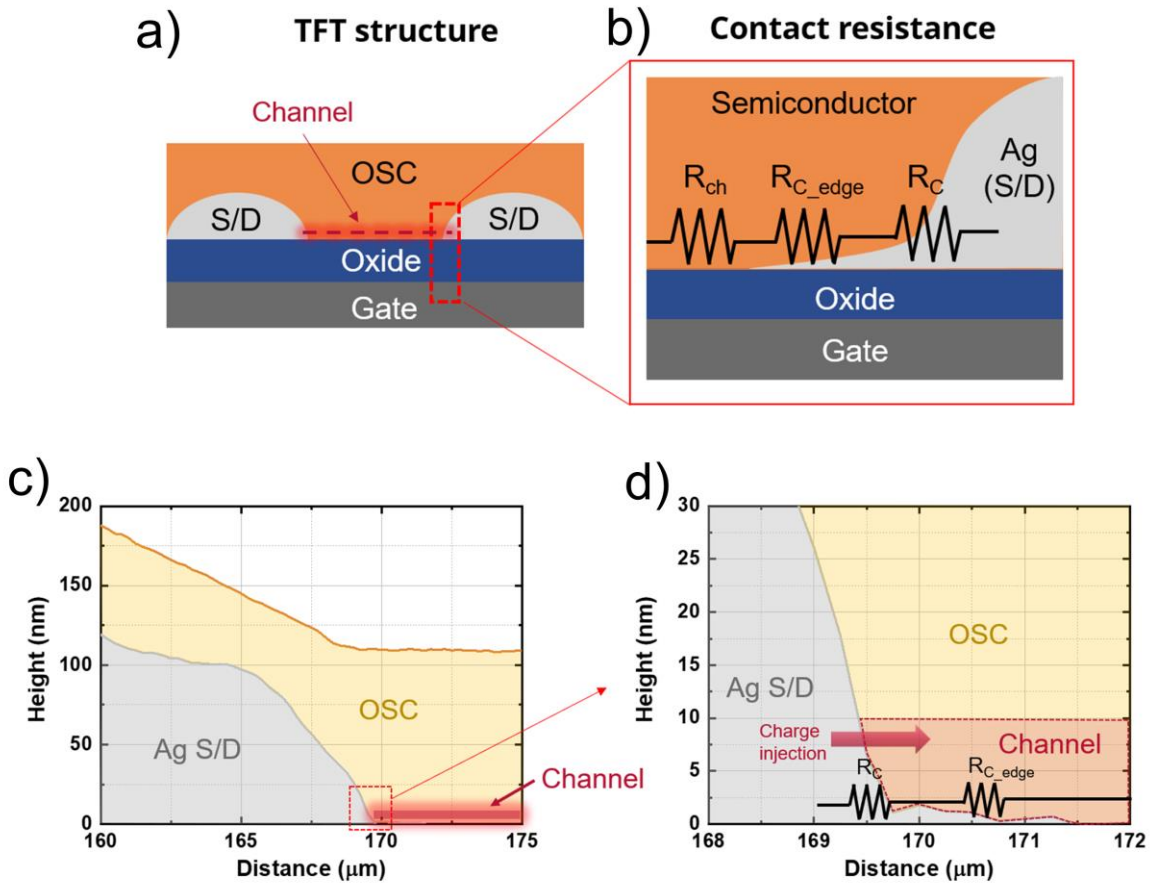

Figure 5.14: (a) Schematic illustrations of BGBC TFTs with inkjet-printed Ag S/D. (b) Components that make up the contact series resistance in the TFT device. (c) Cross-sectional profile of the contact region of the device: P3HT (OSC) – yellow region and printed Ag S/D – silver region. The accumulation layer is depicted as the red line at the bottom of OSC film; charge injection is along the edge of Ag S/D contact. (d) Cross-sectional profile schematically showing the surface roughness along the edge of the printed Ag contact due to the island formation of the Ag.

resistance (R_C) and the newly introduced edge resistance (R_{C_edge}). The surface roughness at the edge was quantified using a surface profilometer (DETAK), as illustrated in Figure 5.14 (c) and (d). Measurements near the edge of the Ag S/D revealed a thickness of a few nanometers. This cross-sectional gradient gives rise to a new resistance component, R_{C_edge}. The formation of the accumulation layer along at the interface of the semiconductor and the dielectric is within a few nm [161] , and this tapered discontinuous edge along the printed Ag line results in a contact resistance that is not found in photolithographically patterned contacts having a vertical profile. This profile of the Ag thin film at the surface hinders carrier transport and degrades charge injection from the metal to the semiconductor.

5.2.4 Nanocomposite channels TFT with Ag S/D

The root-cause of the high contact resistance in printed Ag S/D TFTs was investigated in the previous section. When compared to thermally vacuum-deposited gold S/D TFTs, the tapered cross-sectional profile of the edge of the printed Ag line creates a potentially higher contact resistance, resulting in a limitation of using inkjet-printed metal electrodes for S/D electrodes in TFT applications. By using an inkjet printing method, it is difficult to deposit thin metallic films having a uniformly flat and smooth surface and vertical edge. Therefore, as an intrinsic challenge, the poor quality of the structure of printed metal electrodes is inevitable that may lead to degraded device performance. However, a solution processible conductive or metallic ink is still necessary for fully inkjet-printed TFT fabrication in a roll-to-roll (R2R) process, which enables flexible and large area electronics with lower cost and mass manufacturing. To realize this technology, the degraded performance due to the printed metal needs to be overcome. A hybrid nanocomposite ink was investigated to address this challenge.

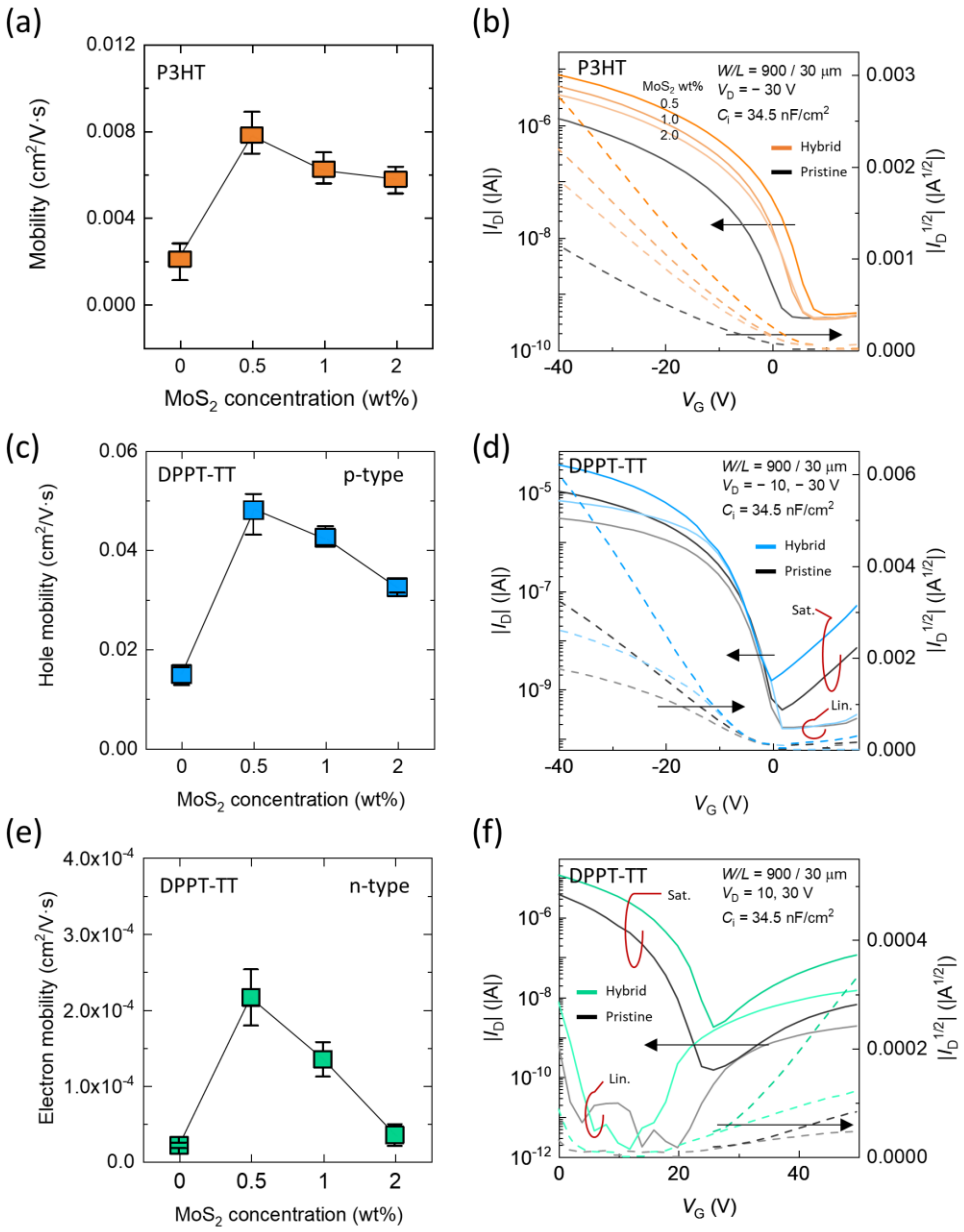

Figure 5.15: The mobility of TFTs with Ag S/D contacts as a function of MoS_2 concentration in (a) P3HT and (c) p-type or (e) n-type DPPT-TT channels. Transfer characteristics of each sample to compare between pristine and hybrid channel TFTs.

The application of hybrid nanocomposite semiconductor inks based on P3HT and DPPT-TT, was employed for inkjet-printed Ag S/D TFTs. In the preceding chapters 3 and 4, it was established

that these hybrid nanocomposite semiconductors effectively enhanced the device performance when combined with vacuum-deposited gold S/D, by improving the crystalline structure of the polymeric films, especially along the interface of the metal-semiconductor contact. Consequently, it was hypothesized that incorporating hybrid nanocomposite semiconductors in inkjet-printed Ag S/D TFTs could also lead to improved device performance. Fig. 5.15 summarizes the extracted mobility and transfer characteristics of all fabricated TFTs with the IJP Ag S/D. In both P3HT and DPPT-TT based hybrid channel TFTs, enhanced device performance was observed compared to pristine channel TFTs. It was further observed that an increase in MoS_2 concentration resulted in a degradation of device performance. Notably, the highest mobility for all fabricated TFTs was achieved when 0.5 wt% of MoS_2 was loaded. This can be seen in the transfer characteristics of Fig. 5.15 b, d, and f, when compared to the pristine channel TFT.

Fig. 5.16 shows the changes in contact resistance and mobility when applying hybrid nanocomposite to TFTs with Ag S/D electrodes. The red circles and blue squares represent the contact resistance and mobility of the devices, respectively. As observed, the transition from vacuum-deposited gold to inkjet-printed Ag S/D electrodes led to an increase in contact resistance and a decrease in mobility. However, the incorporation of MoS_2 in the hybrid channel TFTs demonstrated improved performance with printed Ag S/D electrodes. In particular, the mobility increased from 2×10^{-3} $cm^2/V \cdot s$ to 8.9×10^{-3} $cm^2/V \cdot s$ with the addition of MoS_2 in the P3HT. This performance is comparable to the device with vacuum-deposited gold contacts. Although the contact resistance of the hybrid channel TFT with printed Ag S/D electrodes remains in the similar range of 1 $M\Omega \cdot cm$, it slightly decreased. The enhanced crystalline quality of the polymeric semiconductor was responsible for overcoming the high contact resistance in the TFT contacts.

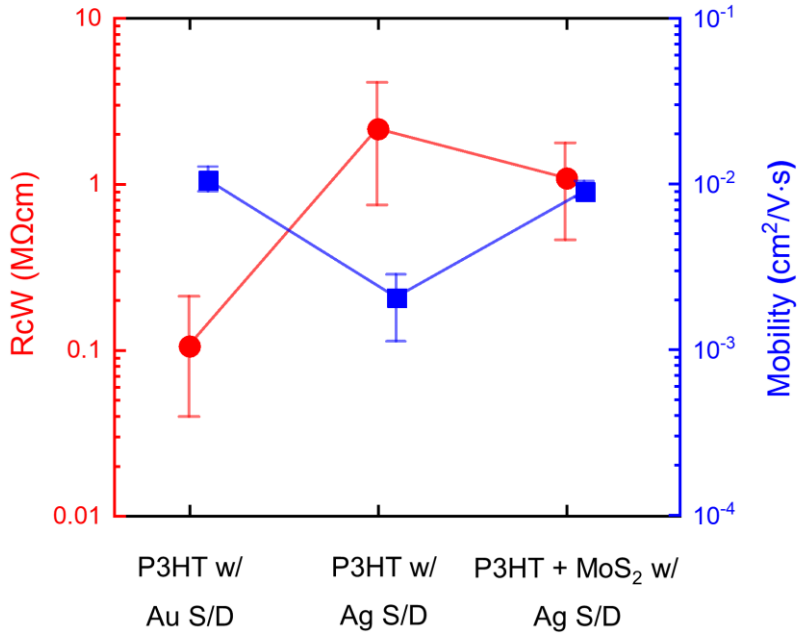

Figure 5.16: Contact resistances and mobility changes for P3HT-based pristine and hybrid channel TFTs with different contact materials.

This result demonstrates that the newly developed P3HT and MoS_2 hybrid nanocomposite semiconductor ink may be used to address the inherent limitation of degraded mobility resulting from printed metal electrodes, by enhancing the charge transport property. Beyond P3HT, DPPT-TT, which exhibits superior charge transport characteristics, was also used as the channel material for inkjet-printed TFTs with printed Ag S/D electrodes. The hybrid semiconductor, mixed with MoS_2 suspension, was also investigated.

The R_C and μ_{sat} of inkjet-printed P3HT or DPPT-TT channel TFTs with either vacuum-deposited gold or printed Ag S/D electrodes are summarized in Figure 5.17. The grey circles and yellow squares in the figure represent printed Ag and vacuum-deposited Au S/D, respectively. Notably, TFTs with printed Ag S/D consistently showed higher contact resistance compared to those with

vacuum-deposited gold S/D in each case. The primary reason for the elevated contact resistance originated from the printed silver contacts.

When the semiconductor material transitions from P3HT to hybrid P3HT to DPPT-TT to hybrid DPPT-TT, their charge transport properties are improved for both photolithographically-defined and printed contacts (Figure 5.17a). As previously explained, the contact resistance can be slightly improved by enhancing the charge transport property of semiconductors, but R_C remains nearly constant. Even with the application of the hybrid ink for the channel material, the contact resistance did not exhibit significant improvement in both P3HT and DPPT-TT. Overall, devices with gold contacts demonstrate better mobilities due to the higher contact resistance of silver S/D (Fig. 5.17b). The mobility of P3HT-based TFTs with Ag S/D decreased from 1.0×10^{-2} $cm^2/V \cdot s$ (gold S/D) to 1.8×10^{-3} $cm^2/V \cdot s$. When the hybrid semiconductor is applied, the mobility increases from 1.8×10^{-3} $cm^2/V \cdot s$ to 8.9×10^{-3} $cm^2/V \cdot s$, which closely resembles the performance of devices with gold contacts (indicated by the red dashed line in the figure).

In the case of DPPT-TT channel TFTs, the mobility also shows improvement upon the application of the hybrid semiconductor for both types of contacts. The mobility of pristine DPPT-TT channel TFT with Ag S/D is 1.5×10^{-2} $cm^2/V \cdot s$, slightly superior to the pristine P3HT channel TFT with gold contacts (1.0×10^{-2} $cm^2/V \cdot s$). This result indicates a significant problem of degraded mobility in any polymer materials due to the contact resistance resulting from printed metallic lines. However, by using the hybrid semiconductor, the mobility is improved to 4.8×10^{-2} $cm^2/V \cdot s$, a three-fold increase. As a result, this improved performance can be comparable to the device with pristine DPPT-TT and gold S/D, with a mobility of 6.7×10^{-2} $cm^2/V \cdot s$, even if silver contacts lead to higher R_C.

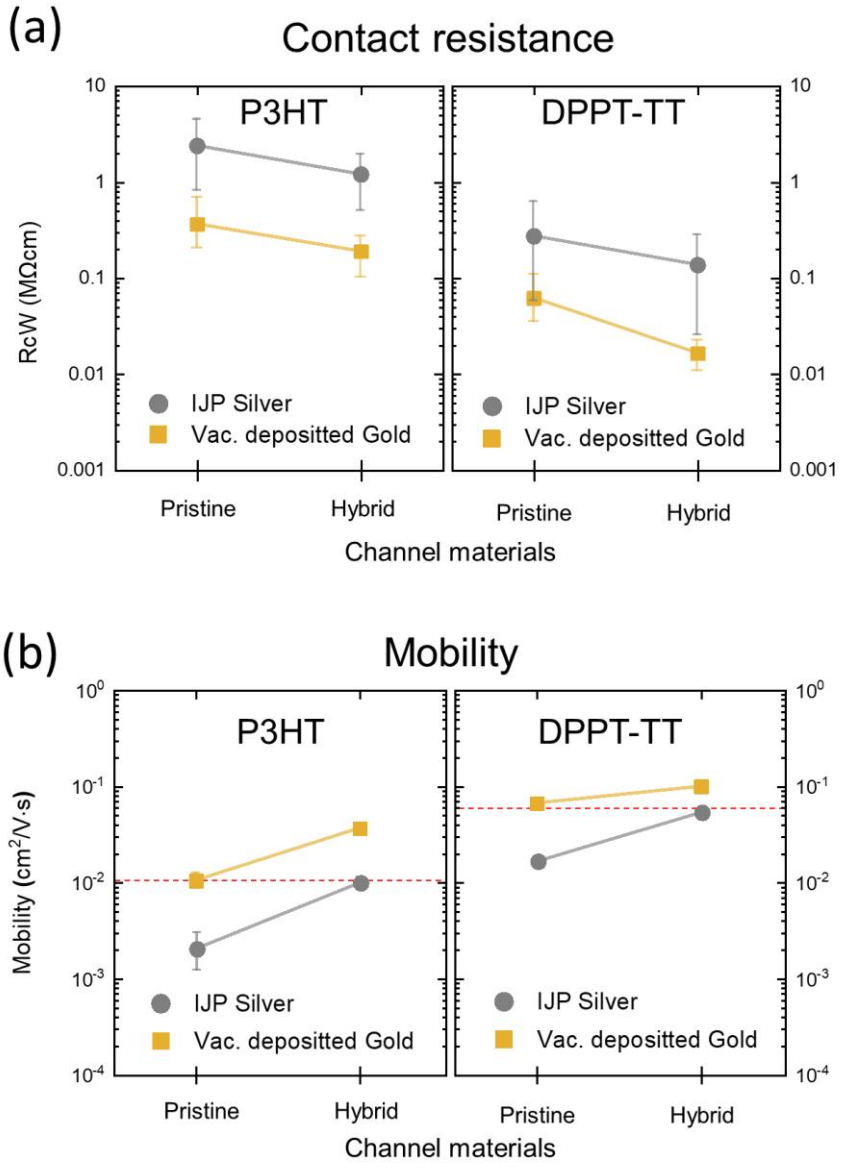

Figure 5.17: (a) Contact resistances and (b) mobility changes for P3HT (left) and DPPT-TT (right) channel materials, with inkjet-printed silver (grey circle) and vacuum deposited gold (yellow square) contacts. Nine different devices are measured in each different case. A total of 72 TFTs were measured to extract contact resistances and mobilities.

These findings demonstrate the prospective utilization of hybrid nanocomposite semiconductors as an effective strategy to enhance the performance of fully inkjet-printed TFTs. Future

investigations to explore the contact engineering, with advanced polymer semiconductors and their integration with 2D materials in nanocomposite semiconductors hold the potential for a synergistic and impactful synergy. This convergence of research endeavors is expected to yield significant advancements and unlock the potential for achieving higher performance levels in fully inkjet-printed TFTs.

5.3 Conclusions

To find the optimized sintering temperature of inkjet-printed silver electrodes for TFT application, various sintering temperatures were tested. By using 4-probe measurement, the 100 nm thickness printed Ag film on SiO_2/Si wafer showed that increased sintering temperature increases conductivity and decreases resistivity until 210 °C, after this point it loses its conductivity. The effect of sintering temperature on Ag film morphology is studied, and SEM analysis shows that the printed Ag thin film sintered at 210 °C has a large cluster and domain for complete merging of Ag nanoparticles each other. Lower sintering temperatures 150 °C and 180 °C makes not completely sintered all Ag nanoparticles, but 180 °C sintered Ag thin film showed similar sheet resistance to 210 °C sintered samples. Thus, three 150, 180, and 210 °C sintering temperatures are chosen to be used for S/D electrodes of TFTs for comparative study.

The relation between the morphology of Ag film and TFT performance was investigated. The device performance varied with the sintering temperature. When it increased, the contact resistance and field effect mobility of devices were also improved. AFM reveals that this is because the polymer film morphology forms differently on the different structural surfaces of silver electrodes. Higher sintering temperature (210 °C) makes printed silver nanoparticles completely merge and form a large flat surface, even if it has bigger vacancies in the Ag film. The large polymer domain

could be formed on this surface condition. It should have better charge injection area or properties between the Ag electrodes and polymers. Thus, it can reduce the contact resistance of TFT.

However, it still has higher contact resistance than the TFT with vacuum deposited gold S/D. Through the SEM and AFM, non-flat edge and surface roughness of printed Ag S/D is the major reason to increase the contact resistance of device, especially it is more severe in BCBG structure. Finally, the use of hybrid nanocomposite ink overcomes the intrinsic challenge of printed metal electrodes that leads to high contact resistance. As studied in previous chapters, both P3HT and DPPT-TT polymer semiconductors had enhanced crystallinity when it mixed with MoS_2 nanosheets. These hybrid nanocomposite channel TFTs improved mobility of devices which is comparable to the TFTs which have pristine polymer channel and vacuum-deposited gold.

Chapter 6
Conclusions and Future Work

6.1 Conclusions

The first study conducted showed the integration of few-layer MoS_2 nanosheets as a hybrid composite material with P3HT-based electronic inks for the fabrication of TFT devices. The addition of a surfactant increased the creation of few-layer MoS_2 nanosheets, resulting in improved electrical and structural properties of the P3HT thin film. The field-effect mobility of the TFTs was dependent on the concentration of MoS_2 nanosheets within the nanocomposite electronic ink, with a marginal effect observed for TFTs having MoS_2 concentrations > 0.5 wt% in P3HT.

In the second study, results were shown for the use of 2D materials as additives for enhancing charge transport properties in inkjet-printed TFTs based on DA copolymers (DPPT-TT). The addition of MoS_2 in a DA copolymer matrix enhances carrier mobility in both hole and electron transport. In electrical stability measurements, the addition of MoS_2 nanosheets into the polymers in thin film increased the charge trap states and leads to further instability of the devices which was degraded with increasing concentration of MoS_2 (~2 wt%). The microstructure analysis of thin films based on DPPT-TT was conducted using AFM, UV-vis-NIR, and XRD characterization techniques. The findings indicated that the incorporation of MoS_2 nanosheets led to the formation of strongly aggregated polymeric domains and a heightened level of molecular ordering within the polymer matrix. However, with increasing concentration of the MoS_2 suspension (> 0.5 wt% MoS_2), the overall structural quality of the film exhibited degradation due to a higher density of nucleation sites due to the increased concentration of nanosheet sites in the suspension. Consequently, an increased density of domain boundaries was observed within the film by optical

absorption and x-ray diffraction characterization, leading to enhanced carrier scattering that adversely affected the electrical performance of the TFTs.

In the third study, the optimal sintering temperature was examined for inkjet-printed silver electrodes in TFT applications. It was found that increasing the sintering temperature (T_{Ag}) increased conductivity and decreased resistivity of printed silver thin film up to T_{Ag} = 210° C. The correlation between the morphology of the Ag film and the performance of the TFTs was investigated, and the device performance that varied with sintering temperature. Higher sintering temperature (210 °C) led to improved contact resistance and field-effect mobility of devices. AFM analysis revealed that the improved performance was due to the formation of a large flat surface with completely merged printed silver nanoparticles at 210 °C. This surface condition allowed the formation of a larger polymer domain with better charge injection properties between the Ag electrodes and polymers, resulting in reduced R_C. However, the R_C of devices with printed Ag S/D remained higher than that of TFTs with vacuum-deposited gold S/D. The non-flat edges and surface roughness of the printed Ag S/D were the primary reasons for the increased R_C of the device, particularly in the BCBG structure. To overcome this inherent limitation of printed metal electrodes leading to high R_C, hybrid nanocomposite inks were utilized. The P3HT and DPPT-TT polymer semiconductors, when mixed with MoS_2 nanosheets, resulted in improved mobility of the devices. This improvement in mobility was comparable to TFTs with pristine polymer channels and vacuum-deposited gold, ultimately addressing the issue of high contact resistance caused by the printed metal electrodes.

6.2 Future work

To build upon the research conducted in this thesis, further investigations can be undertaken in all three areas.

1. Regarding the MoS_2 suspension for inkjet printing, the introduced DDTS-treated MoS_2 suspension exhibited improved dispersion, exfoliation, and stability, especially when used in conjunction with a surfactant. However, DDTS, an alkyltrichlorosilane, poses a potential challenge due to its non-conductive nature and long alkyl chains, which may hinder charge transfer between MoS_2 nanosheets and polymers. To enhance the overall charge transport properties of the hybrid nanocomposite, alternative alkyltrichlorosilanes with shorter chains as additives [71] or other methods such as ion intercalation (alkali metal) [164] and hydroxide based intercalators (NaOH and LiOH) [165] capable of functionalizing MoS_2 nanosheets could be explored.

2. In the study of polymers and MoS_2 hybrid nanocomposite semiconductors, while MoS_2 has been utilized in this mixture, other 2D materials or polymers can also be integrated into this hybrid system. For example, black phosphorus (BP), known for its superior electron mobility compared to MoS_2, [166] could be incorporated. It also possesses solution-processibility achieved through liquid-phase exfoliation, allowing for the production of few-layer nanosheets [167]. Notably, this method aligns with the approach employed for the MoS_2 suspension proposed within this thesis. An additional advantageous trait of this material is its similarity in bandgap (~1.5 eV) to that of MoS_2 in a few-layered nanosheet structure [167]. When integrated with a DA copolymer, this could yield improved n-type transport with higher electron mobility through the inorganic semiconductor and improved thin-film semiconductor ordering. Moreover, other 2D semiconductors like WS_2 (tungsten disulfide) or WSe_2 (tungsten diselenide) with p-type transport properties [166] and higher hole mobilities than MoS_2, when employed in p-type polymeric semiconductors, could enhance

the hole conductivity by increasing the hole majority carriers to the HOMO levels of the polymeric semiconductor (creating excess holes during operation). As one of the 2D materials, boron nitride (BN) nanosheets can be considered a promising candidate for hybrid nanocomposites when combined with polymers. While a limited number of studies have explored nanocomposites comprising BN and P3HT, similar to MoS_2 nanosheets, BN nanotubes have shown potential as templates to enhance the crystalline structure of P3HT. These investigations have revealed that P3HT chains tend to align along the BN nanotubes in an aggregated configuration.

However, the nanocomposite with BN has not yet found applications in TFT devices. Therefore, their introduction as a semiconductor in TFTs holds particular interest, especially considering that BN is inherently an insulating material, in contrast to MoS_2. In this context, improved electrical properties of nanocomposite semiconductor can be investigated from the perspective of structural enhancements without electrical interactions with the polymer, thus presenting an intriguing avenue for further exploration.

3. Addressing the high contact resistance of inkjet-printed metal electrodes in fully inkjet-printed TFTs can be achieved by refining the inkjet printing method for the semiconductor and metallic inks. The line edge roughness of printed metal electrodes can be reduced by modifying the substrate's surface energy using various self-assembled monolayer (SAM) layers or surface treatment methods such as UV-ozone and O_2 plasma to get hydrophobic or hydrophilic surface, respectively. The deposited pattern depends on the surface energy of the substrate related to evaporation dynamic (more detail in Appendix A). The surface modifications could result in tradeoffs of continuity for the printed features; printing on hydrophobic surfaces could result in discontinuous lines. The printing methodology could be modified to account for these wetting conditions with the adoption of double-inkjet printing or employing a side wall (bank pattern)

approach that could prove beneficial. In the case of double-inkjet printing, the second inkjet printing of metal can fill in the gaps or vacancies of the initially printed metal electrodes, resulting in a better edge of pattern. Similarly, using a printed side wall can assist in achieving a flat edge for the metal electrode. For instance, a bank pattern can be initially printed as a sacrificial layer (like a role of photoresist in the lithography process), followed by printing the metal electrode on the bank pattern at the edges. After removing the bank pattern through solvent cleaning, a uniform and flat-edged metal electrode can be obtained. In future research endeavors, these proposed methods could be implemented in fully inkjet-printed TFT applications to reduce contact resistance and enhance device performance.

Bibliography

[1] Arias A C, MacKenzie J D, McCulloch I, Rivnay J and Salleo A 2010 Materials and Applications for Large Area Electronics: Solution-Based Approaches *Chemical Reviews* **110** 3-24

[2] Baran D, Corzo D and Blazquez G 2020 Flexible Electronics: Status, Challenges and Opportunities **1**

[3] Gao X, Lin L, Liu Y and Huang X 2015 LTPS TFT Process on Polyimide Substrate for Flexible AMOLED *Journal of Display Technology* **11** 666-9

[4] Huang X, Yu Z, Huang S, Zhang Q, Li D, Luo Y and Meng Q 2010 Preparation of fluorine-doped tin oxide (SnO2:F) film on polyethylene terephthalate (PET) substrate *Materials Letters* **64** 1701-3

[5] Wang K Y, Chung T-S and Amy G 2012 Developing thin-film-composite forward osmosis membranes on the PES/SPSf substrate through interfacial polymerization **58** 770-81

[6] Forrest S R 2004 The path to ubiquitous and low-cost organic electronic appliances on plastic *Nature* **428** 911-8

[7] Yan H, Chen Z, Zheng Y, Newman C, Quinn J R, Dötz F, Kastler M and Facchetti A 2009 A high-mobility electron-transporting polymer for printed transistors *Nature* **457** 679-86

[8] Yap Y K and Zhang D 2014 *Encyclopedia of Nanotechnology,* ed B Bhushan (Dordrecht: Springer Netherlands) pp 1-8

[9] 2010 *Chemical Vapour Deposition: An Integrated Engineering Design for Advanced Materials,* ed Y Xu and X-T Yan (London: Springer London) pp 1-28

[10] Chung S, Cho K and Lee T 2019 Recent Progress in Inkjet-Printed Thin-Film Transistors **6** 1801445

[11] Żołek-Tryznowska Z 2016 *Printing on Polymers,* ed J Izdebska and S Thomas: William Andrew Publishing) pp 87-99

[12] Lin Y, Liu C-F, Song Y-J, Yang L, Zeng W-J, Lai W-Y and Huang W 2016 Improved performances of inkjet-printed poly(3-hexylthiophene) organic thin-film transistors by inserting an ionic self-assembled monolayer *RSC Advances* **6** 40970-4

[13] Ma J, Hashimoto K, Koganezawa T and Tajima K 2013 End-on orientation of semiconducting polymers in thin films induced by surface segregation of fluoroalkyl chains *J Am Chem Soc* **135** 9644-7

[14] Chaudhary V, Pandey R K, Prakash R, Kumar N and Singh A K 2019 Highly aligned and crystalline poly(3-hexylthiophene) thin films by off-center spin coating for high performance organic field-effect transistors *Synthetic Metals* **258**

[15] Choudhary K, Chen A X, Pitch G M, Runser R, Urbina A, Dunn T J, Kodur M, Kleinschmidt A T, Wang B G, Bunch J A, Fenning D P, Ayzner A L and Lipomi D J 2021 Comparison of the Mechanical Properties of a Conjugated Polymer Deposited Using Spin Coating, Interfacial Spreading, Solution Shearing, and Spray Coating *Acs Appl Mater Inter* **13** 51436-46

[16] Shockley W 1952 A Unipolar "Field-Effect" Transistor *Proceedings of the IRE* **40** 1365-76

[17] Tao X and Koncar V 2016 *Smart Textiles and their Applications,* ed V Koncar (Oxford: Woodhead Publishing) pp 569-98

[18] Newman C R, Frisbie C D, da Silva Filho D A, Brédas J-L, Ewbank P C and Mann K R 2004 Introduction to Organic Thin Film Transistors and Design of n-Channel Organic Semiconductors *Chemistry of Materials* **16** 4436-51

[19] Weis M 2012 Gradual channel approximation models for organic field-effect transistors: The space-charge field effect **111** 054506

[20] Goetz K P and Jurchescu O D 2019 *Handbook of Organic Materials for Electronic and Photonic Devices (Second Edition)*, ed O Ostroverkhova: Woodhead Publishing) pp 453-87
[21] Un H-I, Wang J-Y and Pei J 2019 Recent Efforts in Understanding and Improving the Nonideal Behaviors of Organic Field-Effect Transistors **6** 1900375
[22] Braga D and Horowitz G 2009 High-Performance Organic Field-Effect Transistors **21** 1473-86
[23] Gundlach D J, Zhou L, Nichols J A, Jackson T N, Necliudov P V and Shur M S 2006 An experimental study of contact effects in organic thin film transistors **100** 024509
[24] Zaumseil J, Baldwin K W and Rogers J A 2003 Contact resistance in organic transistors that use source and drain electrodes formed by soft contact lamination **93** 6117-24
[25] Gupta D and Katiyar M 2006 Mobility estimation incorporating the effects of contact resistance and gate voltage dependent mobility in top contact organic thin film transistors *Proc. of ASID* 425-8
[26] Richards T J and Sirringhaus H 2007 Analysis of the contact resistance in staggered, top-gate organic field-effect transistors **102** 094510
[27] Waldrip M, Jurchescu O D, Gundlach D J and Bittle E G 2020 Contact Resistance in Organic Field-Effect Transistors: Conquering the Barrier **30** 1904576
[28] Chang M F, Lee P T, McAlister S P and Chin A 2009 Small-Subthreshold-Swing and Low-Voltage Flexible Organic Thin-Film Transistors Which Use HfLaO as the Gate Dielectric *IEEE Electron Device Letters* **30** 133-5
[29] Kalb W L, Haas S, Krellner C, Mathis T and Batlogg B 2010 Trap density of states in small-molecule organic semiconductors: A quantitative comparison of thin-film transistors with single crystals *Physical Review B* **81** 155315
[30] Haneef H F, Zeidell A M and Jurchescu O D 2020 Charge carrier traps in organic semiconductors: a review on the underlying physics and impact on electronic devices *Journal of Materials Chemistry C* **8** 759-87
[31] Rolland A, Richard J, Kleider J P and Mencaraglia D 1993 Electrical Properties of Amorphous Silicon Transistors and MIS-Devices: Comparative Study of Top Nitride and Bottom Nitride Configurations *Journal of The Electrochemical Society* **140** 3679
[32] McDowell M, Hill I G, McDermott J E, Bernasek S L and Schwartz J 2006 Improved organic thin-film transistor performance using novel self-assembled monolayers **88** 073505
[33] Yoon M-H, Kim C, Facchetti A and Marks T J 2006 Gate Dielectric Chemical Structure−Organic Field-Effect Transistor Performance Correlations for Electron, Hole, and Ambipolar Organic Semiconductors *Journal of the American Chemical Society* **128** 12851-69
[34] Kalb W L and Batlogg B 2010 Calculating the trap density of states in organic field-effect transistors from experiment: A comparison of different methods *Physical Review B* **81** 035327
[35] Xue F, Liu Z, Su Y and Varahramyan K 2006 Inkjet printed silver source/drain electrodes for low-cost polymer thin film transistors *Microelectronic Engineering* **83** 298-302
[36] Määttänen A, Ihalainen P, Pulkkinen P, Wang S, Tenhu H and Peltonen J 2012 Inkjet-Printed Gold Electrodes on Paper: Characterization and Functionalization *Acs Appl Mater Inter* **4** 955-64
[37] Kang J S, Kim H S, Ryu J, Thomas Hahn H, Jang S and Joung J W 2010 Inkjet printed electronics using copper nanoparticle ink *Journal of Materials Science: Materials in Electronics* **21** 1213-20
[38] Tortorich R P and Choi J W 2013 Inkjet Printing of Carbon Nanotubes *Nanomaterials (Basel, Switzerland)* **3** 453-68

[39] Song O, Rhee D, Kim J, Jeon Y, Mazánek V, Söll A, Kwon Y A, Cho J H, Kim Y-H, Sofer Z and Kang J 2022 All inkjet-printed electronics based on electrochemically exfoliated two-dimensional metal, semiconductor, and dielectric *npj 2D Materials and Applications* **6** 64
[40] Bihar E, Roberts T, Saadaoui M, Hervé T, De Graaf J B and Malliaras G G 2017 Inkjet-Printed PEDOT:PSS Electrodes on Paper for Electrocardiography **6** 1601167
[41] Lo L-W, Zhao J, Wan H, Wang Y, Chakrabartty S and Wang C 2021 An Inkjet-Printed PEDOT:PSS-Based Stretchable Conductor for Wearable Health Monitoring Device Applications *Acs Appl Mater Inter* **13** 21693-702
[42] Kim Y-J, Kim J, Kim Y S and Lee J-K 2013 TiO2-poly(4-vinylphenol) nanocomposite dielectrics for organic thin film transistors *Organic Electronics* **14** 3406-14
[43] Ning H, Liang Z, Fu X, Yao R, Xu Z, Qiu T, Yang Z, Hu C, Xu W and Peng J 2022 Environmentally friendly, flexible and high performance PVA dielectric layer fabricated by solution method and its application in IGZO-TFT *Organic Electronics* **100** 106383
[44] Martínez-Domingo C, Conti S, de la Escosura-Muñiz A, Terés L, Merkoçi A and Ramon E 2020 Organic-based field effect transistors for protein detection fabricated by inkjet-printing *Organic Electronics* **84** 105794
[45] Zheng W and Wong S-C 2003 Electrical conductivity and dielectric properties of PMMA/expanded graphite composites *Composites Science and Technology* **63** 225-35
[46] Dasgupta S, Kruk R, Mechau N and Hahn H 2011 Inkjet Printed, High Mobility Inorganic-Oxide Field Effect Transistors Processed at Room Temperature *ACS Nano* **5** 9628-38
[47] Kawase T, Shimoda T, Newsome C, Sirringhaus H and Friend R H 2003 Inkjet printing of polymer thin film transistors *Thin Solid Films* **438-439** 279-87
[48] Pipan G, Bogar M, Ciavatti A, Basiricò L, Cramer T, Fraboni B and Fraleoni-Morgera A 2018 Direct Inkjet Printing of TIPS-Pentacene Single Crystals onto Interdigitated Electrodes by Chemical Confinement **5** 1700925
[49] Han C Y, Tang W M and Lai P-T 2021 High-mobility pentacene organic thin-film transistors achieved by reducing remote phonon scattering and surface-roughness scattering *Applied Surface Science* **544** 148656
[50] Pankow R M and Thompson B C 2020 The development of conjugated polymers as the cornerstone of organic electronics *Polymer* **207** 122874
[51] Shi W, Yu J, Huang W, Yu X and Zheng Y 2013 Performance enhancement of poly(3-hexylthiophene) organic field-effect transistor by inserting poly(methylmethacrylate) buffer layer *Applied Physics Letters* **102** 111607
[52] Li J, Zhao Y, Tan H S, Guo Y, Di C-A, Yu G, Liu Y, Lin M, Lim S H, Zhou Y, Su H and Ong B S 2012 A stable solution-processed polymer semiconductor with record high-mobility for printed transistors *Scientific Reports* **2** 754
[53] Ong B S, Wu Y, Li Y, Liu P and Pan H 2008 Thiophene Polymer Semiconductors for Organic Thin-Film Transistors **14** 4766-78
[54] Printz A D and Lipomi D J 2016 Competition between deformability and charge transport in semiconducting polymers for flexible and stretchable electronics *Applied Physics Reviews* **3**
[55] Yang H, Zhang R, Wang L, Zhang J, Yu X, Liu J, Xing R, Geng Y and Han Y 2015 Face-On and Edge-On Orientation Transition and Self-Epitaxial Crystallization of All-Conjugated Diblock Copolymer *Macromolecules* **48** 7557-66
[56] Kroon R, Mengistie D A, Kiefer D, Hynynen J, Ryan J D, Yu L and Müller C 2016 Thermoelectric plastics: from design to synthesis, processing and structure–property relationships *Chemical Society Reviews* **45** 6147-64
[57] Brinkmann M 2011 Structure and morphology control in thin films of regioregular poly(3-hexylthiophene) *Journal of Polymer Science Part B: Polymer Physics* **49** 1218-33

[58] Jewel M U, Monne M A, Mishra B and Chen M Y 2020 Inkjet-Printed Molybdenum Disulfide and Nitrogen-Doped Graphene Active Layer High On/Off Ratio Transistors *Molecules* **25**
[59] Jiang Z, Xiao K, Chen J-J, Wang Y, Xu Z-Q, Sowade E, Baumann R R, Sheremet E, Rodriguez R D and Feng Z-S 2020 All-inkjet-printed high-performance flexible MoS2 and MoS2-reduced graphene oxide field-effect transistors *Journal of Materials Science* **55** 12969-79
[60] Jawaid A, Nepal D, Park K, Jespersen M, Qualley A, Mirau P, Drummy L F and Vaia R A 2016 Mechanism for Liquid Phase Exfoliation of MoS2 *Chemistry of Materials* **28** 337-48
[61] Forsberg V, Zhang R, Bäckström J, Dahlström C, Andres B, Norgren M, Andersson M, Hummelgård M and Olin H 2016 Exfoliated MoS2 in Water without Additives *PLOS ONE* **11** e0154522
[62] Mir S H, Yadav V K and Singh J K 2020 Recent Advances in the Carrier Mobility of Two-Dimensional Materials: A Theoretical Perspective *ACS Omega* **5** 14203-11
[63] Kim S, Konar A, Hwang W-S, Lee J H, Lee J, Yang J, Jung C, Kim H, Yoo J-B, Choi J-Y, Jin Y W, Lee S Y, Jena D, Choi W and Kim K 2012 High-mobility and low-power thin-film transistors based on multilayer MoS2 crystals *Nature Communications* **3** 1011
[64] Ponomarev E, Pásztor Á, Waelchli A, Scarfato A, Ubrig N, Renner C and Morpurgo A F 2018 Hole Transport in Exfoliated Monolayer MoS2 *ACS Nano* **12** 2669-76
[65] Bao W, Cai X, Kim D, Sridhara K and Fuhrer M S 2013 High mobility ambipolar MoS2 field-effect transistors: Substrate and dielectric effects *Applied Physics Letters* **102**
[66] Guo F, Liu Z, Zhu M and Zheng Y 2019 Electron–phonon scattering limited hole mobility at room temperature in a MoS2 monolayer: first-principles calculations *Physical Chemistry Chemical Physics* **21** 22879-87
[67] Velický M, Toth P S, Rakowski A M, Rooney A P, Kozikov A, Woods C R, Mishchenko A, Fumagalli L, Yin J, Zólyomi V, Georgiou T, Haigh S J, Novoselov K S and Dryfe R A W 2017 Exfoliation of natural van der Waals heterostructures to a single unit cell thickness *Nature Communications* **8** 14410
[68] Li H, Wu J, Yin Z and Zhang H 2014 Preparation and Applications of Mechanically Exfoliated Single-Layer and Multilayer MoS2 and WSe2 Nanosheets *Accounts of Chemical Research* **47** 1067-75
[69] Li J, Naiini M M, Vaziri S, Lemme M C and Östling M 2014 Inkjet Printing of MoS2 *Advanced Functional Materials* **24** 6524-31
[70] Zeng X, Hirwa H, Metel S, Nicolosi V and Wagner V 2018 Solution processed thin film transistor from liquid phase exfoliated MoS2 flakes *Solid-State Electronics* **141** 58-64
[71] Yu X, Prévot M S and Sivula K 2014 Multiflake Thin Film Electronic Devices of Solution Processed 2D MoS2 Enabled by Sonopolymer Assisted Exfoliation and Surface Modification *Chemistry of Materials* **26** 5892-9
[72] Shahar C, Zbaida D, Rapoport L, Cohen H, Bendikov T, Tannous J, Dassenoy F and Tenne R 2010 Surface Functionalization of WS2 Fullerene-like Nanoparticles *Langmuir* **26** 4409-14
[73] Chen I T, Schappell E, Zhang X and Chang C-H 2020 Continuous roll-to-roll patterning of three-dimensional periodic nanostructures *Microsystems & Nanoengineering* **6** 22
[74] Fernandes I J, Aroche A F, Schuck A, Lamberty P, Peter C R, Hasenkamp W and Rocha T L A C 2020 Silver nanoparticle conductive inks: synthesis, characterization, and fabrication of inkjet-printed flexible electrodes *Scientific Reports* **10** 8878
[75] Khodashenas B and Ghorbani H R 2019 Synthesis of silver nanoparticles with different shapes *Arabian Journal of Chemistry* **12** 1823-38

[76] Yu A K, Kudrinskiy A A, Olenin A Y and Lisichkin G V 2008 Synthesis and properties of silver nanoparticles: advances and prospects *Russian Chemical Reviews* **77** 233
[77] Hwang J Y and Moon S J 2013 The characteristic variations of inkjet-printed silver nanoparticle ink during furnace sintering *J Nanosci Nanotechnol* **13** 6145-9
[78] Shen X, Duzhko V V and Russell T P 2013 A Study on the Correlation Between Structure and Hole Transport in Semi-Crystalline Regioregular P3HT **3** 263-70
[79] Mulla M Y, Torsi L and Manoli K 2020 *Methods in Enzymology*, ed P Pelosi and W Knoll: Academic Press) pp 403-33
[80] Xue L, Gao X, Zhao K, Liu J, Yu X and Han Y 2010 The formation of different structures of poly(3-hexylthiophene) film on a patterned substrate by dip coating from aged solution *Nanotechnology* **21** 145303
[81] Grayfer E D, Kozlova M N and Fedorov V E 2017 Colloidal 2D nanosheets of MoS2 and other transition metal dichalcogenides through liquid-phase exfoliation *Advances in Colloid and Interface Science* **245** 40-61
[82] Thompson B C and Frechet J M 2008 Polymer-fullerene composite solar cells *Angew Chem Int Ed Engl* **47** 58-77
[83] Khlyabich P P, Burkhart B and Thompson B C 2011 Efficient ternary blend bulk heterojunction solar cells with tunable open-circuit voltage *J Am Chem Soc* **133** 14534-7
[84] Petoukhoff C E, Vijapurapu D K and O'Carroll D M 2014 Computational comparison of conventional and inverted organic photovoltaic performance parameters with varying metal electrode surface workfunction *Solar Energy Materials and Solar Cells* **120** 572-83
[85] Pascual-San-José E, Rodríguez-Martínez X, Adel-Abdelaleim R, Stella M, Martínez-Ferrero E and Campoy-Quiles M 2019 Blade coated P3HT:non-fullerene acceptor solar cells: a high-throughput parameter study with a focus on up-scalability *Journal of Materials Chemistry A* **7** 20369-82
[86] Li H M, Lee D Y, Choi M S, Qu D, Liu X, Ra C H and Yoo W J 2014 Metal-semiconductor barrier modulation for high photoresponse in transition metal dichalcogenide field effect transistors *Sci Rep* **4** 4041
[87] Sahoo D, Kumar B, Sinha J, Ghosh S, Roy S S and Kaviraj B 2020 Cost effective liquid phase exfoliation of MoS2 nanosheets and photocatalytic activity for wastewater treatment enforced by visible light *Scientific Reports* **10** 10759
[88] Long D X, Xu Y, Kang S-J, Park W-T, Choi E-Y, Nah Y-C, Liu C and Noh Y-Y 2015 Solution processed vanadium pentoxide as charge injection layer in polymer field-effect transistor with Mo electrodes *Organic Electronics* **17** 66-76
[89] Lim S C, Kim S H, Lee J H, Kim M K, Kim D J and Zyung T 2005 Surface-treatment effects on organic thin-film transistors *Synthetic Metals* **148** 75-9
[90] Merlo J A and Frisbie C D 2003 Field effect conductance of conducting polymer nanofibers **41** 2674-80
[91] Mampallil D and Eral H B 2018 A review on suppression and utilization of the coffee-ring effect *Adv Colloid Interface Sci* **252** 38-54
[92] Gu K, Wang Y, Li R, Tsai E, Onorato J W, Luscombe C K, Priestley R D and Loo Y-L 2021 Role of Postdeposition Thermal Annealing on Intracrystallite and Intercrystallite Structuring and Charge Transport in Poly(3-hexylthiophene) *Acs Appl Mater Inter* **13** 999-1007
[93] Kanai K, Miyazaki T, Suzuki H, Inaba M, Ouchi Y and Seki K 2010 Effect of annealing on the electronic structure of poly(3-hexylthiophene) thin film *Physical Chemistry Chemical Physics* **12** 273-82
[94] Al-Mohsin H, Ali S and Bermak A 2022 Design and Fabrication Process Optimization of Silver-Based Inkjet-Printed Microheater **10** 1677

[95] Oh Y, Kim J, Yoon Y J, Kim H, Yoon H G, Lee S-N and Kim J 2011 Inkjet printing of Al2O3 dots, lines, and films: From uniform dots to uniform films *Current Applied Physics* **11** S359-S63
[96] Soltman D and Subramanian V 2008 Inkjet-Printed Line Morphologies and Temperature Control of the Coffee Ring Effect *Langmuir* **24** 2224-31
[97] Mondal S K, Biswas A, Pradhan J R and Dasgupta S 2021 Inkjet-Printed MoS2 Transistors with Predominantly Intraflake Transport *Small Methods* **5** 2100634
[98] Ghayeb Zamharir S, Karimzadeh R and Aboutalebi S H 2018 Laser-assisted tunable optical nonlinearity in liquid-phase exfoliated MoS2 dispersion *Applied Physics A* **124**
[99] Mukherjee S, Maiti R, Midya A, Das S and Ray S K 2015 Tunable Direct Bandgap Optical Transitions in MoS2 Nanocrystals for Photonic Devices *ACS Photonics* **2** 760-8
[100] Shanmugam M, Bansal T, Durcan C A and Yu B 2012 Molybdenum disulphide/titanium dioxide nanocomposite-poly 3-hexylthiophene bulk heterojunction solar cell *Applied Physics Letters* **100**
[101] Petoukhoff C E, Kosar S, Goto M, Bozkurt I, Chhowalla M and Dani K M 2019 Charge transfer dynamics in conjugated polymer/MoS2 organic/2D heterojunctions *Molecular Systems Design & Engineering* **4** 929-38
[102] Wang X, Guo W, Zhu Y, Liang X, Wang F and Peng P 2018 Electrical and Mechanical Properties of Ink Printed Composite Electrodes on Plastic Substrates *Applied Sciences* **8**
[103] Yin X, Li Y, Huang X, Tian J, Meng H and Wu W 2020 Scalable and efficient extraction of two-dimensional MoS2 nanosheets from dispersions as a co-catalyst for enhancing Fenton reactions *Journal of Materials Science* **55** 14358-72
[104] Splendiani A, Sun L, Zhang Y, Li T, Kim J, Chim C-Y, Galli G and Wang F 2010 Emerging Photoluminescence in Monolayer MoS2 *Nano Letters* **10** 1271-5
[105] Chang M, Lim G T, Park B and Reichmanis E 2017 Control of Molecular Ordering, Alignment, and Charge Transport in Solution-Processed Conjugated Polymer Thin Films *Polymers (Basel)* **9**
[106] Zhao Y, Shao S, Xie Z, Geng Y and Wang L 2009 Effect of Poly (3-hexylthiophene) Nanofibrils on Charge Separation and Transport in Polymer Bulk Heterojunction Photovoltaic Cells *The Journal of Physical Chemistry C* **113** 17235-9
[107] Huang J, Hines D R, Jung B J, Bronsgeest M S, Tunnell A, Ballarotto V, Katz H E, Fuhrer M S, Williams E D and Cumings J 2011 Polymeric semiconductor/graphene hybrid field-effect transistors *Organic Electronics* **12** 1471-6
[108] Yadav P, Chanmal C, Basu A, Mandal L, Jog J and Ogale S 2013 Catalyst free novel synthesis of graphene and its application in high current OFET and phototransistor based on P3HT/G composite *RSC Advances* **3** 18049-54
[109] Tiwari S, Singh A K and Prakash R 2014 Poly(3-hexylthiophene) (P3HT)/Graphene Nanocomposite Material Based Organic Field Effect Transistor with Enhanced Mobility *Journal of Nanoscience and Nanotechnology* **14** 2823-8
[110] Lin C-T, Hsu C-H, Lee C-H and Wu W-J 2011 Inkjet-Printed Organic Field-Effect Transistor by Using Composite Semiconductor Material of Carbon Nanoparticles and Poly(3-Hexylthiophene) *Journal of Nanotechnology* **2011** 142890
[111] Sun Z, Li J, Liu C, Yang S and Yan F 2011 Enhancement of Hole Mobility of Poly(3-hexylthiophene) Induced by Titania Nanorods in Composite Films *Advanced Materials* **23** 3648-52
[112] Jang J, Kim J, Bae M, Lee J, Myong Kim D, Hwan Kim D, Lee J, Lee B-L, Koo B and Wan Jin Y 2012 Extraction of the sub-bandgap density-of-states in polymer thin-film transistors with the multi-frequency capacitance-voltage spectroscopy *Applied Physics Letters* **100**

[113] Dagan R, Vaknin Y, Henning A, Shang J Y, Lauhon L J and Rosenwaks Y 2019 Two-dimensional charge carrier distribution in MoS2 monolayer and multilayers *Applied Physics Letters* **114**
[114] Choi D, Chang M and Reichmanis E 2015 Controlled Assembly of Poly(3-hexylthiophene): Managing the Disorder to Order Transition on the Nano- through Meso-Scales *Advanced Functional Materials* **25** 920-7
[115] Keum J K, Xiao K, Ivanov I N, Hong K, Browning J F, Smith G S, Shao M, Littrell K C, Rondinone A J, Andrew Payzant E, Chen J and Hensley D K 2013 Solvent quality-induced nucleation and growth of parallelepiped nanorods in dilute poly(3-hexylthiophene) (P3HT) solution and the impact on the crystalline morphology of solution-cast thin film *CrystEngComm* **15** 1114-24
[116] Jo G, Jung J and Chang M 2019 Controlled Self-Assembly of Conjugated Polymers via a Solvent Vapor Pre-Treatment for Use in Organic Field-Effect Transistors *Polymers (Basel)* **11**
[117] Clark J, Chang J-F, Spano F C, Friend R H and Silva C 2009 Determining exciton bandwidth and film microstructure in polythiophene films using linear absorption spectroscopy *Applied Physics Letters* **94**
[118] Go G-T, Lee Y, Seo D-G, Pei M, Lee W, Yang H and Lee T-W 2020 Achieving Microstructure-Controlled Synaptic Plasticity and Long-Term Retention in Ion-Gel-Gated Organic Synaptic Transistors *Advanced Intelligent Systems* **2**
[119] Bakour A, Baitoul M, Bajjou O, Massuyeau F and Faulques E 2017 Improving optical properties of in situ reduced graphene oxide/poly(3-hexylthiophene) composites *Materials Research Express* **4** 025031
[120] Park S Y, Kwon E H and Park Y D 2020 Effect of localized UV irradiation on the crystallinity and electrical properties of dip-coated polythiophene thin films *RSC Advances* **10** 34130-6
[121] Alizadehaghdam M, Heck B, Siegenführ S, AlShetwi Y A, Keheze F M, Stäter S, Abbasi F and Reiter G 2020 Following isothermal and non-isothermal crystallization of poly(3-hexylthiophene) thin films by UV–vis spectroscopy *Polymer* **210** 122959
[122] Seidler N, Lazzerini G M, Li Destri G, Marletta G and Cacialli F 2013 Enhanced crystallinity and film retention of P3HT thin-films for efficient organic solar cells by use of preformed nanofibers in solution *Journal of Materials Chemistry C* **1** 7748-57
[123] Park M S and Kim F S 2019 Synergistic Effects of Processing Additives and Thermal Annealing on Nanomorphology and Hole Mobility of Poly(3-hexylthiophene) Thin Films *Polymers (Basel)* **11**
[124] Wang W, Chen C, Tollan C, Yang F, Qin Y and Knez M 2017 Efficient and controllable vapor to solid doping of the polythiophene P3HT by low temperature vapor phase infiltration *Journal of Materials Chemistry C* **5** 2686-94
[125] Lee Y, Mongare A, Plant A and Ryu D 2021 Strain-Microstructure-Optoelectronic Inter-Relationship toward Engineering Mechano-Optoelectronic Conjugated Polymer Thin Films *Polymers (Basel)* **13**
[126] Baeg K-J, Khim D, Kim D-Y, Koo J B, You I-K, Choi W S and Noh Y-Y 2010 High mobility top-gated poly(3-hexylthiophene) field-effect transistors with high work-function Pt electrodes *Thin Solid Films* **518** 4024-9
[127] Yang L, Cui X, Zhang J, Wang K, Shen M, Zeng S, Dayeh S A, Feng L and Xiang B 2014 Lattice strain effects on the optical properties of MoS2 nanosheets *Scientific Reports* **4** 5649
[128] Gao D, Si M, Li J, Zhang J, Zhang Z, Yang Z and Xue D 2013 Ferromagnetism in freestanding MoS2 nanosheets *Nanoscale Research Letters* **8** 129

[129] Higgins S G, Muir B V O, Dell'Erba G, Perinot A, Caironi M and Campbell A J 2016 Complementary Organic Logic Gates on Plastic Formed by Self-Aligned Transistors with Gravure and Inkjet Printed Dielectric and Semiconductors **2** 1500272
[130] Kang M S and Frisbie C D 2013 A Pedagogical Perspective on Ambipolar FETs **14** 1547-52
[131] Kleinhenz N, Persson N, Xue Z, Chu P H, Wang G, Yuan Z, McBride M A, Choi D, Grover M A and Reichmanis E 2016 Ordering of Poly(3-hexylthiophene) in Solutions and Films: Effects of Fiber Length and Grain Boundaries on Anisotropy and Mobility *Chemistry of Materials* **28** 3905-13
[132] Kim Y and Park B N 2020 Electrical Signature of Ultrasound-Induced Anisotropic Self-Assembly of Poly(3-Hexylthiophene) (P3HT) during Channel Formation **10** 6886
[133] Szendrei K, Jarzab D, Chen Z, Facchetti A and Loi M A 2010 Ambipolar all-polymer bulk heterojunction field-effect transistors *Journal of Materials Chemistry* **20** 1317-21
[134] Chaudhary V, Pandey R K, Sahu P K, Prakash R, Kumar N and Kumar Singh A 2020 MoS2 Assisted Self-Assembled Poly(3-hexylthiophene) Thin Films at an Air/Liquid Interface for High-Performance Field-Effect Transistors under Ambient Conditions *The Journal of Physical Chemistry C* **124** 8101-9
[135] Kim D H, Shin H-J, Lee H S, Lee J, Lee B-L, Lee W H, Lee J-H, Cho K, Kim W-J, Lee S Y, Choi J-Y and Kim J M 2012 Design of a Polymer–Carbon Nanohybrid Junction by Interface Modeling for Efficient Printed Transistors *ACS Nano* **6** 662-70
[136] Tiwari S P, Verma R, Alam M B, Kumari R, Sinha O P and Srivastava R 2017 Charge transport study of P3HT blended MoS2 *Vacuum* **146** 474-7
[137] Chang C H and Chien C H 2011 Functionalized Single-Walled Carbon-Nanotube-Blended P3HT-Based Thin-Film Transistors With Multiwalled Carbon-Nanotube Source and Drain Electrodes *IEEE Electron Device Letters* **32** 1457-9
[138] Zhang Y, Liu S, Liu W, Liang T, Yang X, Xu M and Chen H 2015 Two-dimensional MoS2-assisted immediate aggregation of poly-3-hexylthiophene with high mobility *Physical Chemistry Chemical Physics* **17** 27565-72
[139] Yang Y S, Kim S H, Lee J-I, Chu H Y, Do L-M, Lee H, Oh J, Zyung T, Ryu M K and Jang M S J A p l 2002 Deep-level defect characteristics in pentacene organic thin films **80** 1595-7
[140] Kuzum D, Park J H, Krishnamohan T, Wong H S P and Saraswat K C 2011 The Effect of Donor/Acceptor Nature of Interface Traps on Ge MOSFET Characteristics *IEEE Transactions on Electron Devices* **58** 1015-22
[141] Neo W T, Ye Q, Shi Z, Chua S-J and Xu J 2018 Influence of catalytic systems in Stille polymerization on the electrochromic performance of diketopyrrolopyrrole-based conjugated polymers *Materials Chemistry Frontiers* **2** 331-7
[142] Li M, An C, Marszalek T, Baumgarten M, Müllen K and Pisula W 2016 Impact of Interfacial Microstructure on Charge Carrier Transport in Solution-Processed Conjugated Polymer Field-Effect Transistors **28** 2245-52
[143] Chaudhary V, Pandey R K, Prakash R, Kumar N and Singh A K 2019 Highly aligned and crystalline poly(3-hexylthiophene) thin films by off-center spin coating for high performance organic field-effect transistors *Synthetic Metals* **258** 116221
[144] Jo G, Jung J and Chang M 2019 Controlled Self-Assembly of Conjugated Polymers via a Solvent Vapor Pre-Treatment for Use in Organic Field-Effect Transistors **11** 332
[145] Brinkmann M and Wittmann J-C 2006 Orientation of Regioregular Poly(3-hexylthiophene) by Directional Solidification: A Simple Method to Reveal the Semicrystalline Structure of a Conjugated Polymer **18** 860-3

[146] Borchert J W, Peng B, Letzkus F, Burghartz J N, Chan P K L, Zojer K, Ludwigs S and Klauk H 2019 Small contact resistance and high-frequency operation of flexible low-voltage inverted coplanar organic transistors *Nature Communications* **10** 1119
[147] Jung K-D, Kim Y C, Shin H, Park B-G, Lee J D, Cho E S and Kwon S J 2010 A study on the carrier injection mechanism of the bottom-contact pentacene thin film transistor **96** 103305
[148] Gupta D, Katiyar M and Gupta D 2009 An analysis of the difference in behavior of top and bottom contact organic thin film transistors using device simulation *Organic Electronics* **10** 775-84
[149] Liu C, Xu Y and Noh Y-Y 2015 Contact engineering in organic field-effect transistors *Materials Today* **18** 79-96
[150] Roh J, Lee T, Kang C-m, Kwak J, Lang P, Horowitz G, Kim H and Lee C 2017 Injection-modulated polarity conversion by charge carrier density control via a self-assembled monolayer for all-solution-processed organic field-effect transistors *Scientific Reports* **7** 46365
[151] Zikulnig J, Roshanghias A, Rauter L and Hirschl C 2020 Evaluation of the Sheet Resistance of Inkjet-Printed Ag-Layers on Flexible, Uncoated Paper Substrates Using Van-der-Pauw's Method *Sensors (Basel, Switzerland)* **20**
[152] Mypati S, Dhanushkodi S R, McLaren M, Docoslis A, Peppley B A and Barz D P J 2018 Optimized inkjet-printed silver nanoparticle films: theoretical and experimental investigations *RSC Advances* **8** 19679-89
[153] Apostolakis A, Barmpakos D, Pilatis A, Patsis G, Pagonis D-N, Belessi V and Kaltsas G 2022 Resistivity study of inkjet-printed structures and electrical interfacing on flexible substrates *Micro and Nano Engineering* **15** 100129
[154] Ghibaudo G 1988 New method for the extraction of MOSFET parameters. In: *Electronics Letters*: Institution of Engineering and Technology) pp 543-5
[155] Xu Y, Minari T, Tsukagoshi K, Chroboczek J A and Ghibaudo G 2010 Direct evaluation of low-field mobility and access resistance in pentacene field-effect transistors *Journal of Applied Physics* **107** 114507
[156] Natali D, Chen J, Maddalena F, García Ferré F, Di Fonzo F and Caironi M 2016 Injection Length in Staggered Organic Thin Film Transistors: Assessment and Implications for Device Downscaling **2** 1600097
[157] Liu D, Wang W, Zhang J, Ren Q, Fan L, Wang Y, Zhang Y and Zhang M 2023 A Universal Method for Extracting and Quantitatively Analyzing Bias-Dependent Contact Resistance in Carbon-Nanotube Thin-Film Transistors **9** 2201148
[158] Zhao Y, Xiao X, Huo Y, Wang Y, Zhang T, Jiang K, Wang J, Fan S and Li Q 2017 Influence of Asymmetric Contact Form on Contact Resistance and Schottky Barrier, and Corresponding Applications of Diode *Acs Appl Mater Inter* **9** 18945-55
[159] Tazuhara S, Nagase T, Kobayashi T, Sadamitsu Y and Naito H 2021 Understanding the influence of contact resistances on short-channel high-mobility organic transistors in linear and saturation regimes *Applied Physics Express* **14** 041010
[160] Maddali H, House K L, Emge T J and O'Carroll D M 2020 Identification of the local electrical properties of crystalline and amorphous domains in electrochemically doped conjugated polymer thin films *RSC Advances* **10** 21454-63
[161] Dinelli F, Murgia M, Levy P, Cavallini M, Biscarini F and de Leeuw D M 2004 Spatially correlated charge transport in organic thin film transistors *Physical review letters* **92** 116802
[162] Villarrubia J S 2005 Issues in Line Edge and Linewidth Roughness Metrology *AIP Conference Proceedings* **788** 386-93

[163] Jung K-D, Kim Y C, Shin H, Park B-G, Lee J D, Cho E S and Kwon S J 2010 A study on the carrier injection mechanism of the bottom-contact pentacene thin film transistor *Applied Physics Letters* **96**
[164] Zhu X, Su Z, Wu C, Cong H, Ai X, Yang H and Qian J 2022 Exfoliation of MoS2 Nanosheets Enabled by a Redox-Potential-Matched Chemical Lithiation Reaction *Nano Letters* **22** 2956-63
[165] Bang G S, Nam K W, Kim J Y, Shin J, Choi J W and Choi S-Y 2014 Effective Liquid-Phase Exfoliation and Sodium Ion Battery Application of MoS2 Nanosheets *Acs Appl Mater Inter* **6** 7084-9
[166] Cheng L, Zhang C and Liu Y 2020 Why Two-Dimensional Semiconductors Generally Have Low Electron Mobility *Physical review letters* **125** 177701
[167] Hanlon D, Backes C, Doherty E, Cucinotta C S, Berner N C, Boland C, Lee K, Harvey A, Lynch P, Gholamvand Z, Zhang S, Wang K, Moynihan G, Pokle A, Ramasse Q M, McEvoy N, Blau W J, Wang J, Abellan G, Hauke F, Hirsch A, Sanvito S, O'Regan D D, Duesberg G S, Nicolosi V and Coleman J N 2015 Liquid exfoliation of solvent-stabilized few-layer black phosphorus for applications beyond electronics *Nature Communications* **6** 8563
[168] Li Y, Yang Q, Li M and Song Y 2016 Rate-dependent interface capture beyond the coffee-ring effect *Scientific Reports* **6** 24628
[169] Fall S, Biniek L, Odarchenko Y, Anokhin D V, de Tournadre G, Lévêque P, Leclerc N, Ivanov D A, Simonetti O, Giraudet L and Heiser T 2016 Tailoring the microstructure and charge transport in conjugated polymers by alkyl side-chain engineering *Journal of Materials Chemistry C* **4** 286-94
[170] Calvimontes A 2014 A thermodynamic approach to predict apparent contact angles on microstructures using surface polygonal maps *Soft Matter* **10** 8308-23
[171] Hu G, Kang J, Ng L W T, Zhu X, Howe R C T, Jones C G, Hersam M C and Hasan T 2018 Functional inks and printing of two-dimensional materials *Chemical Society Reviews* **47** 3265-300
[172] Pradhan T K and Panigrahi P K 2018 *Selected Topics in Photonics*, ed A Pradhan and P K Krishnamurthy (Singapore: Springer Singapore) pp 69-77
[173] Hu H and Larson R G 2006 Marangoni Effect Reverses Coffee-Ring Depositions *The Journal of Physical Chemistry B* **110** 7090-4
[174] Sempels W, De Dier R, Mizuno H, Hofkens J and Vermant J 2013 Auto-production of biosurfactants reverses the coffee ring effect in a bacterial system *Nature Communications* **4** 1757
[175] Ku G M, Lee E, Kang B, Lee J H, Cho K and Lee W H 2017 Relationship between the dipole moment of self-assembled monolayers incorporated in graphene transistors and device electrical stabilities *RSC Advances* **7** 27100-4
[176] Chang J-F, Sun B, Breiby D W, Nielsen M M, Sölling T I, Giles M, McCulloch I and Sirringhaus H 2004 Enhanced Mobility of Poly(3-hexylthiophene) Transistors by Spin-Coating from High-Boiling-Point Solvents *Chemistry of Materials* **16** 4772-6
[177] Sung Kyu P, Yong Hoon K, Jeong In H, Dae Gyu M and Won Keun K 2002 High-performance polymer tfts printed on a plastic substrate *IEEE Transactions on Electron Devices* **49** 2008-15
[178] Deen M J, Kazemeini M H, Haddara Y M, Jianfei Y, Vamvounis G, Holdcroft S and Woods W 2004 Electrical characterization of polymer-based FETs fabricated by spin-coating poly(3-alkylthiophene)s *IEEE Transactions on Electron Devices* **51** 1892-901

Appendix A

Coffee-ring effect and evaporation dynamic of droplets

Ideally, a thin film should have a uniform thickness, but solution inks form non-uniform film thicknesses due to the evaporation of the liquid [91]. When a droplet of liquid dries on the solid surface, the ring-like stain remains after the evaporation. This phenomenon known as the coffee-ring or coffee-stain effect is generally considered to be one of the main challenges of inkjet printing technology [168]. Fig. A.1 shows the example of the coffee-ring effect and the deposition pattern of inkjet-printed droplets. In Fig. A.1a, the image of the deposition pattern shows clearly the non-uniform thickness along the diameter of the feature. Most of the particles in the solution are along the edge of the droplet forming a ring-like shape that is thicker on the edge of the ring. On the

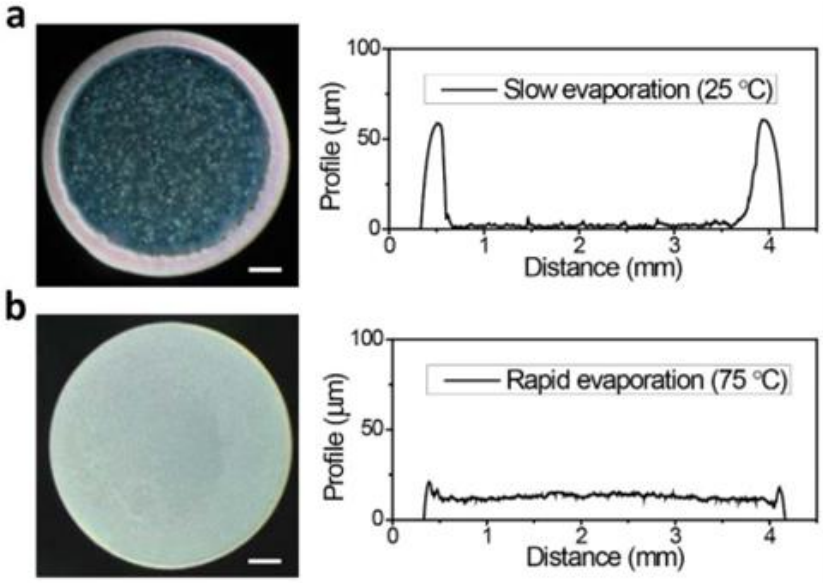

Figure A.1: The images and surface profiles of deposition results of hydrophilic polystyrene nanospheres in water. a) coffee-ring like and b) uniform deposition pattern [168].

contrary, process variations such as rapid annealing can minimize this effect and Fig. A.1b shows a more uniform thickness due to minimizing the coffee-ring effect.

To understand how to minimize this effect, one should consider how the drying of the ink is affected by the many variables such as temperature, humidity, the surface energy of the substrate, surface tension of the liquid, and the evaporation rate [169]. In order to control the droplet drying and suppress the coffee- ring effect, it is important to understand the evaporation dynamics of a droplet, shown in Fig. A.2. The contact angle of a droplet can be determined by Young's equation which is describing the relation between the contacts of each vapor (*V*), liquid (*L*), and solid (*S*) phases [170]:

$$\gamma_{SV} = \gamma_{SL} + \gamma_{LV} \cos\theta \tag{6.1}$$

where γ_{SV}, γ_{SL}, and γ_{LV} are the interfacial tension of solid-vapor, solid-liquid, and liquid-vapor, respectively, and θ is the contact angle shown in the left side of Fig. A.2. It is important to measure the contact angle of the droplet to determine the surface energy of the substrate. When the surface

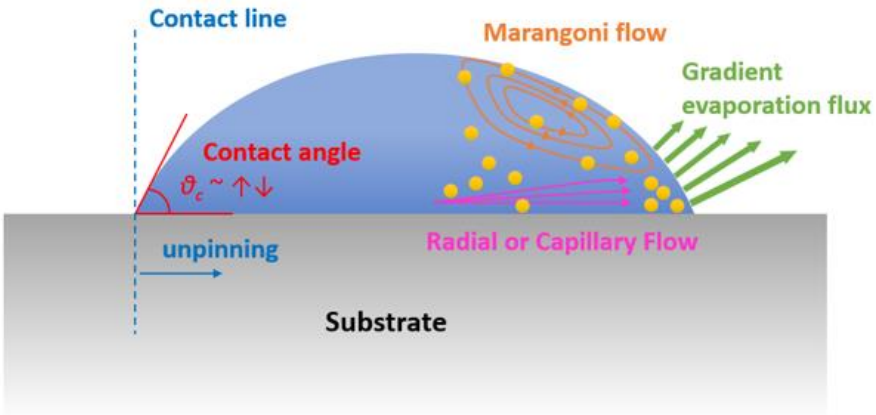

Figure A.2: Evaporation dynamic of a single droplet on the substrate.

is hydrophobic, defined as a higher droplet contact angle $\gg 90°$ and is due to a low surface energy [170, 171]. In this case, the contact line at the edge of the droplet is typically free to move or is not pinned. This contact line will recede to the center of the droplet during the evaporation since the volume of liquid continuously decreases while drying. As this is happening, the contact angle will stay constant. These concepts are described on the left side of the schematic droplet in Fig. A.2. On the contrary, when the contact angle is $\ll 90°$, the surface has high surface energy and is described as a hydrophilic surface [170, 171]. For a hydrophilic surface, the contact line is pinned, or will not recede during evaporation, and the contact angle changes during the film formation.

Moreover, the shape of the droplet also affects the evaporation rate along the droplet surface and this evaporation rate affects the distribution of particles in the droplet. For a hydrophilic surface, the contact angle changes as the droplet solvent evaporates, causing the curvature of the droplet to vary along the surface. This variation results in a faster evaporation rate along the edge of the droplet compared to its midsection; the green arrows in Fig. A.2 depict the higher evaporation flux. As a result, a concentration gradient develops and an outward radial or capillary flow [169] develops through the entire droplet. The non-uniform distribution of evaporation flux induces surface tension gradient on the surface of the droplet since concentration at the liquid-air interface also depends on the evaporation rate on the surface [172]. Then the surface tension gradient on the surface of droplet results in re-circulation flow in the liquid known as Marangoni convection or Marangoni flow which takes place between two different surface tensions [173]. Hence, Marangoni flow between the edge and the apex of the droplet can be used to suppress the coffee-ring effect as a force to move the particles to the center [173, 174]. However, when the

capillary flow is dominant rather than the Marangoni flow, the particles move to the edge of the droplet and form a ring-shaped pattern.

Another approach to minimizing the coffee-ring effect is to maintain a hydrophobic surface. In this case, the contact angle of the droplet is large, and the contact line recedes as the solvent evaporates. In this process, the shape of a droplet remains constant, and the evaporation flux (green arrows in Fig. A.2) is uniform over the surface of the droplet. The capillary flow can then be minimized, and the coffee ring effect can be suppressed by minimizing the concentration gradient due to the non-uniform evaporation rate along the droplet surface.

In summary, a hydrophobic surface, having a higher contact angle and a receding contact line will minimize the effect of forming a concentration gradient in the drying droplet. The use of additives to change the liquid surface tension may also be used to minimize the capillary flow of the solutes in the forming film and minimize the coffee-ring effect.

Appendix B

Hydrophobic surface using HMDS

To improve the charge transport characteristics of polymer films, it is essential to achieve a highly ordered and crystalline structure of the conjugated polymers. The quality of the substrate surface plays a crucial role in achieving this goal since the polymer film is deposited onto the substrate surface. To enhance the surface quality, a self-assembled monolayer (SAMs) is used and treated on the surface of silicon dioxide (SiO_2). The silane molecule of hexamethyldisilazane (HMDS), the SAM material, chemically reacts with the hydroxyl group of SiO_2 surface [175], and it forms trimethylsilanol ($(CH_3)_3SiOH$) as a uniform molecular monolayer on the SiO_2 surface shown in Fig. B.1b. The non-polar property of the methyl group from HMDS forms a hydrophobic surface and thus modifies the surface of SiO_2 by adding the alkyl chain.

The result of the HMDS treatment can be confirmed by contact angle measurements. Single droplet of deionized water (DI-water) was deposited using a micropipette droplet of 10 µL volume on two different surfaces, bare SiO_2 and HMDS treated SiO_2 surfaces. The contact angle of the droplet on the bare SiO_2 surface is 45° (Fig. 2.7) which is much lower than 90° on an HMDS treated surface (Fig. 2.7). This result shows that the HMDS treated SiO_2 surface has lower surface energy

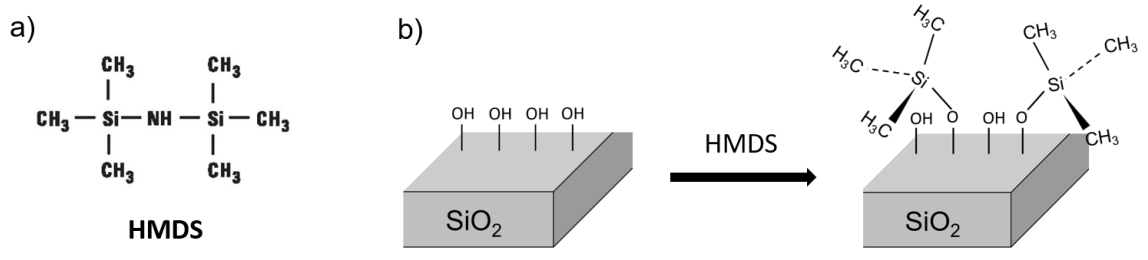

Figure B.1: a) HMDS and b) HMDS treated on the SiO_2 surface.

and becomes more hydrophobic than bare SiO_2 surface. HMDS treated SiO_2 surface was used as a reference of the hydrophobic surface. If the surface is hydrophobic, the contact line at the edge of the droplet should more easily unpin during the evaporation process to prevent the coffee-ring formation. Hence, the contact angle measurement is performed over the evaporation time (Fig. B.2). At a drying time, ~ 5 min, the contact angle and the diameter of a single droplet were ~ 95° and ~3.6 mm, respectively. Since the contact line at the edge of the droplet is unpinned and moving to the center during evaporation, the diameter of the droplet continuously decreases, and the contact angle remained nearly constant, in a range of 95°-97° over time, up to a measurement time of 55 minutes. The hydrophobic and low surface energy obtained on the SiO_2 substrate experimentally demonstrates the effectiveness of treating the surface with HMDS to control the droplet drying.

On the prepared two surfaces (i.e. bare SiO_2 and HMDS treated SiO_2), the fluid dynamics of P3HT rather than DI-water should be investigated to fabricate the TFT. Single droplets of same the volume of P3HT ink were inkjet printed on the two surfaces which are shown in Fig. B.3. In

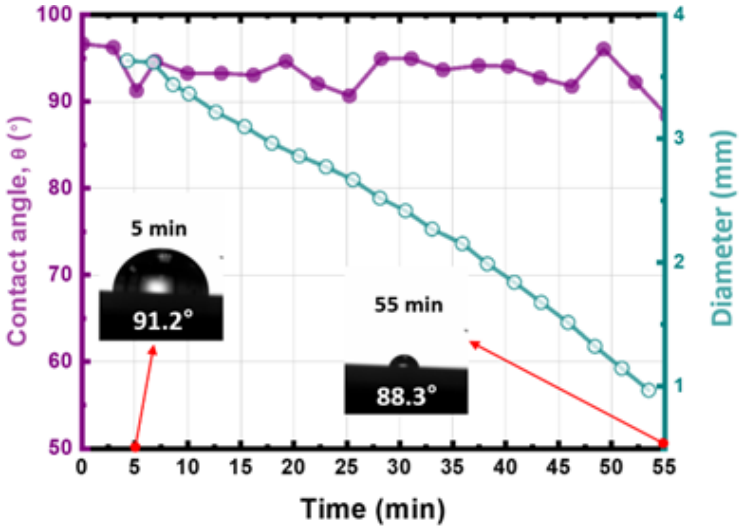

Figure B.2: Contact angle (left axis) and diameter (right axis) of DI-water single droplet on the hydrophobic surface over evaporation time.

the case of bare surface (Fig. B.3a), its diameter is larger than that of the printed pattern on HMDS treated surface since the ink on the hydrophobic surface is dried over time, the contact line at the edge of the droplet was not pinned and was free to move toward the center. In Fig. B.3a, the contrast difference is observed between the near center and edge of the droplet. P3HT looks bright yellow, but when it is thin, the color darkens, similar to the color of the substrate. It is observed that coffee-ring formation happens on the bare and hydrophilic surface. On the contrary, the thicker P3HT film forms at the center on the hydrophobic surface. Based on this result, the coffee-ring effect can be minimized by controlling the substrate surface energy. The results follow the theoretical expectation of the evaporation dynamic which is discussed in Appendix. A.

Fig. B.4 shows the summary of electrical parameters (saturation field-effect mobility, threshold voltage, and subthreshold swing) of inkjet-printed P3HT channel TFTs with different substrate surface conditions. It is noteworthy that the field-effect mobility increases more than one order of magnitude in the case of HMDS treated (hydrophobic) surface compared to the bare surface, possibly due to the organic polymer (P3HT) having a better-ordered crystallinity on the treated

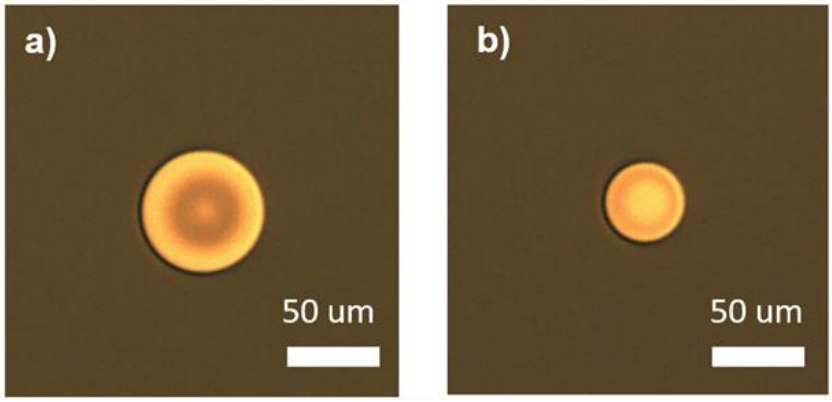

Figure B.3: Optical microscopy of a printed single droplet of P3HT on the different surface a) bare surface and b) HMDS treated surface.

surface [176]. The devices fabricated on the hydrophobic surface have a smaller variation of threshold voltage, suggesting the dangling bonds from the unpassivated SiO_2 bare surface may work as trap states [108]. The data also suggests the TFTs on the hydrophobic surface have

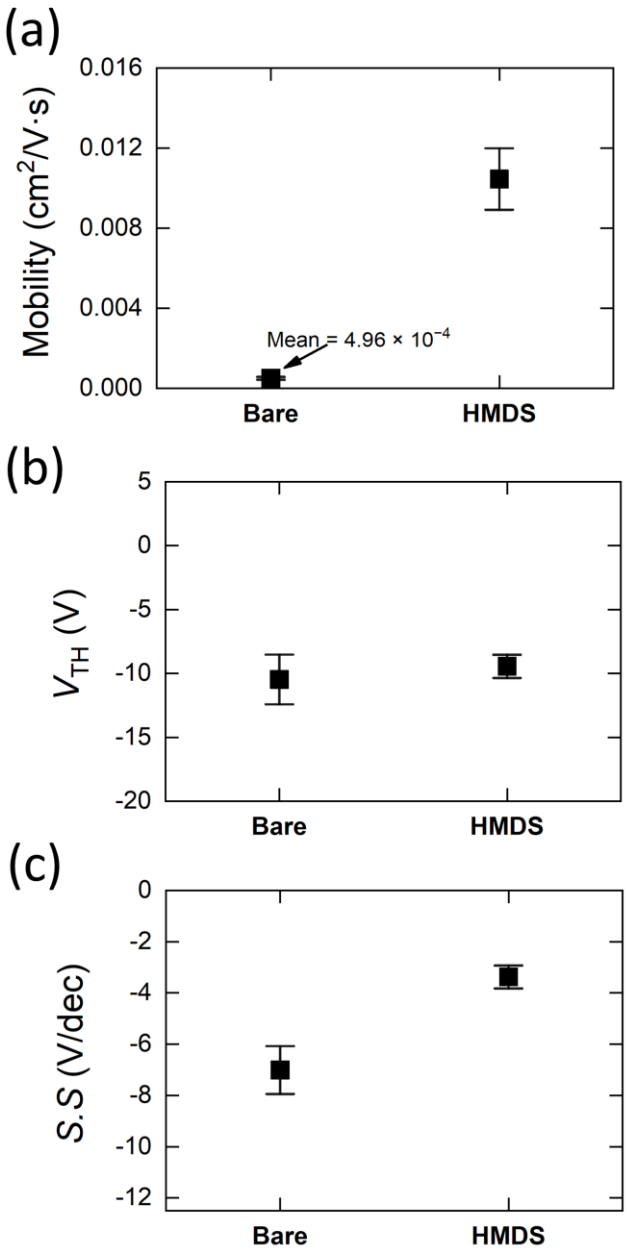

Figure B.4: Summary of electrical characteristics such as (a) carrier mobility, (b) threshold voltage, and (c) subthreshold swing of the inkjet-printed P3HT channel TFTs with bare SiO_2 (left) and HMDS-treated SiO_2 substrate.

enhanced charge transport due to the SAM, the devices have a better subthreshold swing which also indicates improved thin-film quality that results in better switching behavior. The inkjet-printed P3HT TFT, as a reference device, is comparable to the previous studies of spin-cast P3HT film TFT [176-178].

Appendix C

Supplementary information

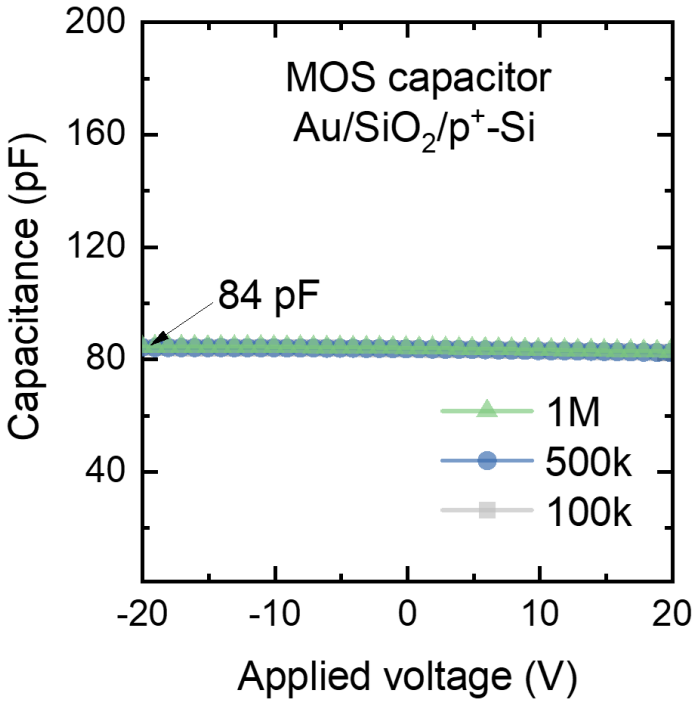

Figure C.1: *C-V* curves for Au/SiO_2 /Si stacks (SiO_2 thickness: 100 nm). The measurement frequencies are 100 kHz, 500kHz, and 1MHz. The gold is top-contact of the metal-oxide-semiconductor (MOS) capacitor which area is 500 × 500 μm^2. Theoretically calculated capacitance is 86.3 pF ($C = \varepsilon_r \varepsilon_0 A/d$, where ε_r is the relative permittivity, ε_0 is the vacuum permittivity, A is the contact pad area, and d is thickness of SiO_2). The arrows indicate the measure capacitance.

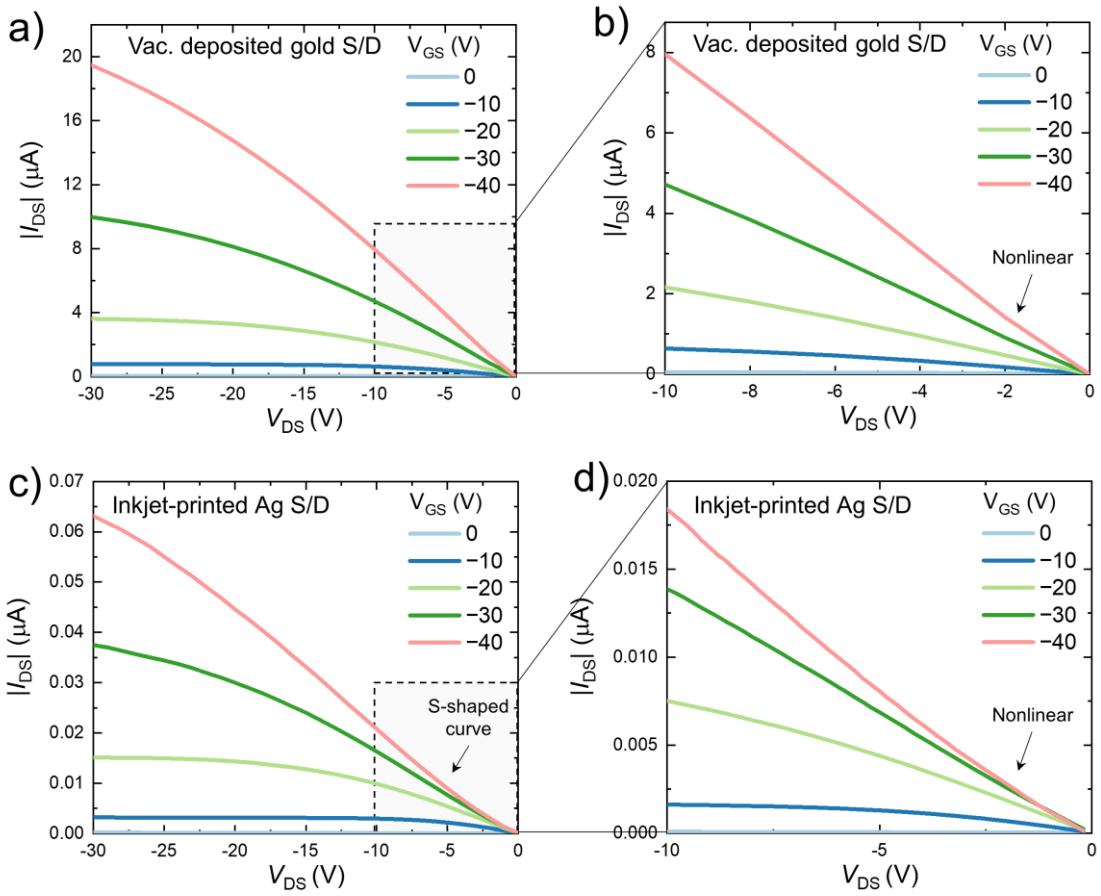

Figure C.2: Output characteristics of inkjet-printed P3HT channel TFTs with a) vacuum deposited Au S/D and b) inkjet-printed Ag S/D. Linear regime of output curves is shown on the right. Since inkjet-printed Ag S/D caused higher contact resistance than the Au S/D, the S-shaped output curve is more clearly observed from the TFTs with printed Ag S/D.

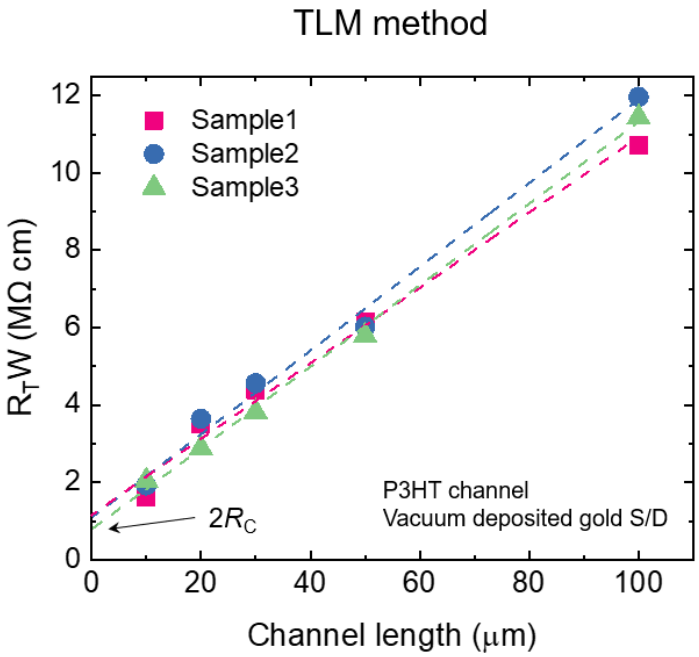

Figure C.3: The width-normalized device resistance as a function of the channel lengths of TFTs. Transfer length method (TLM) was employed to obtain contact resistance of inkjet-printed P3HT TFT with vacuum-deposited gold S/D. The average R_C extracted by YFM is 0.37 MΩ·cm. Therefore, both methods showed very similar results.

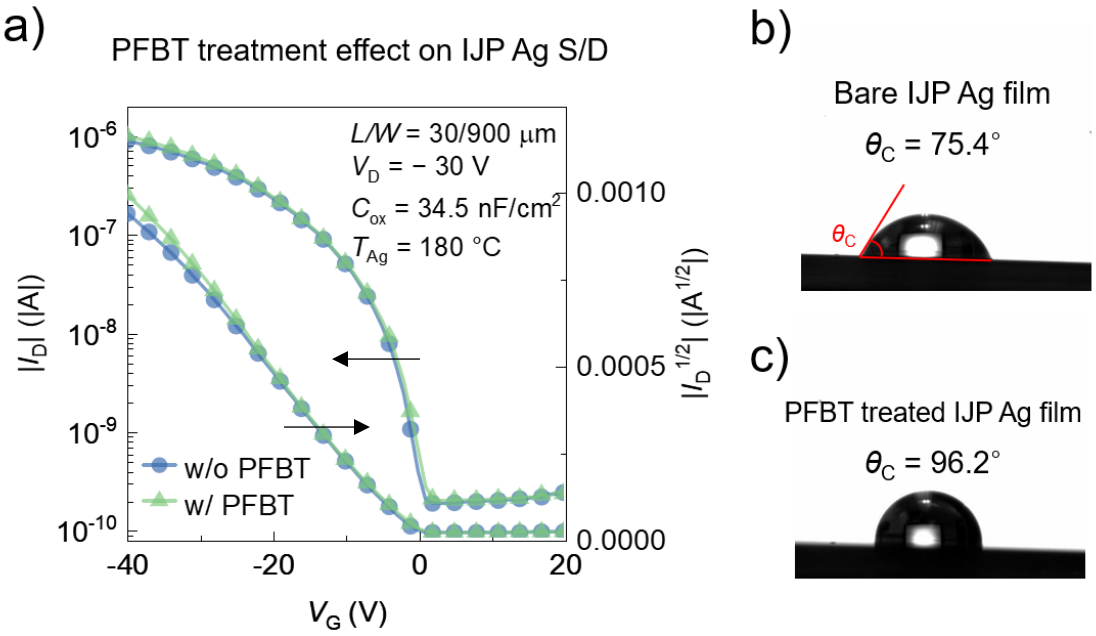

Figure C.4: a) Transfer characteristics of inkjet printed P3HT TFTs with printed Ag S/D (Ag film is sintered at 180 °C) with and without PFBT treatment. Both devices show similar electrical properties indicating PFBT has a negligible impact on the device performance in the experimental configuration of this study. Contact angle measurement results of b) a bare printed Ag film and c) a PFBT treated Ag film.